Universidad Autónoma de San Luis Potosí
Facultad de Ingeniería
Centro de Investigación y Estudios de Posgrado

Modeling of fluid flow and drug delivery through a cancerous nodule.

T E S I S

Que para obtener el grado de:

Maestría en Ingeniería Mecánica

Presenta:
Jorge Andrés Monasterio González

Asesor:
Dr. Francisco Gerardo Pérez Gutiérrez

Co-asesor:
Dr. Ricardo Romero Méndez

San Luis Potosí, S. L. P. Agosto de 2026

UASLP
Universidad Autónoma de San Luis Potosí

FACULTAD DE INGENIERÍA

20 de noviembre de 2025

ING. JORGE ANDRÉS MONASTERIO GONZÁLEZ
P R E S E N T E.

En atención a su solicitud de Temario, presentada por el **Dres. Francisco Gerardo Pérez Gutiérrez y Ricardo Romero Méndez,** Asesor y Coasesor de la Tesis que desarrollará Usted, con el objeto de obtener el Grado de **Maestro en Ingeniería Mecánica**. Me es grato comunicarle que en la sesión del H. Consejo Técnico Consultivo celebrada el día 20 de noviembre del presente, fue aprobado el Temario propuesto:

TEMARIO:

"Modelado de flujo de fluidos y suministro de fármacos a través de un nódulo canceroso"

Introducción
1. Estudio de los mecanismos de diseminación transcelular en lesiones tipo carcinoma.
2. Avances en los sistemas de suministro de fármacos para el tratamiento del cáncer de ovario.
3. Modelado computacional del transporte de fármacos libres en un nódulo canceroso dentro de un microcanal.
4. Modelado computacional de un sistema de suministro de fármacos basado en nanopartículas en un nódulo canceroso dentro de un microcanal.
5. Identificación de parámetros críticos y predicción de la dinámica de transferencia de masa de fármacos.

Conclusiones.
Referencias.

"MODOS ET CUNCTARUM RERUM MENSURAS AUDEBO"

A T E N T A M E N T E

DR. EMILIO JORGE GONZÁLEZ GALVÁN
DIRECTOR

UNIVERSIDAD AUTÓNOMA DE SAN LUIS POTOSI
FACULTAD DE INGENIERIA
DIRECCION

Ccp. Archivo
-bvlg

www.uaslp.mx

Av. Manuel Nava 8
Zona Universitaria • CP 78290
San Luis Potosí, S.L.P.
tel. (444) 826 2330 al39
fax (444) 826 2336

UASLP
Universidad Autónoma de San Luis Potosí

FACULTAD DE INGENIERÍA

20 de noviembre de 2025

ING. JORGE ANDRÉS MONASTERIO GONZÁLEZ
P R E S E N T E.

En atención a su solicitud de Temario, presentada por el **Dres. Francisco Gerardo Pérez Gutiérrez. y Ricardo Romero Méndez,** Asesor y Coasesor de la Tesis que desarrollará Usted, con el objeto de obtener el Grado de **Maestro en Ingeniería Mecánica**. Me es grato comunicarle que en la sesión del H. Consejo Técnico Consultivo celebrada el día 20 de noviembre del presente, fue aprobado el Temario propuesto:

TEMARIO:

"Modeling of fluid flow and drug delivery through a cancerous nodule"

Introduction.
1. Study of transcelular dissemination mechanisms in carcinoma type lesions.
2. Advances in drug delivery systems for ovarian cancer therapy.
3. Computational modeling of free-drug transport in a cancerous nodule within a microchannel.
4. Computational modeling of a nanoparticle-based drug delivery system in a canerous nodule within a microchannel.
5. Identification of a critical parameters and prediction of drug mass transfer dynamics.

Conclusions.
References.

"MODOS ET CUNCTARUM RERUM MENSURAS AUDEBO"

A T E N T A M E N T E

DR. EMILIO JORGE GONZÁLEZ GALVÁN
DIRECTOR

UNIVERSIDAD AUTONOMA
DE SAN LUIS POTOSI
FACULTAD DE INGENIERIA
DIRECCION

www.uaslp.mx

Av. Manuel Nava 8
Zona Universitaria • CP 78290
San Luis Potosí, S.L.P.
tel. (444) 826 2330 al39
fax (444) 826 2336

Ccp. Archivo
-bvlg

"1945-2025: 80 años formando profesionales de la Ingeniería en beneficio de la sociedad"

Acknowledgements.

I am extremely grateful to my advisor, Dr. Francisco Gerardo Pérez Gutiérrez for his invaluable guidance, willingness to help and his continuous support, to my co-advisor, Dr. Ricardo Romero Méndez, for extending his experience and expertise to aid my search of knowledge. Both have been incredibly patient with me and have help me grow and develop both personally and academically. Their advices and suggestions have helped me not only in this research or academically, but also as experiences that will remain with me throughout my life.

I am deeply grateful to my mother Cecy and to my brother Mauricio for their incommensurable support, company and love, they have been a beacon of light to guide me through difficult times. Their patience, encouragement and belief in me during each stage of this journey has allowed me to continue forward without losing sight of the path.

I would like to thank my friends who have encouraged me through this journey, their support and companionship have been the catalysts that have allowed me to overcome the challenges I have faced.

I'd like to thank all my professors and the members of the thesis committee for the knowledge they have shared with me and their valuable comments and suggestions which has greatly improved the thesis project but also my own habits.

I would like to acknowledge sincerely the support of Walfre Franco regarding the numerical modeling and simulation work carried out in this thesis.

I would like to thank the CIEP FI, and to the UASLP as a whole for providing the facilities to conduct this research and for making the process enjoyable throughout the way.

Dedication

"*This work is dedicated to my mother Cecy, my brother Mauricio, my pets Ushi and Dembé, my friends, and those who have accompanied me on this journey*".

Resumen

En el estudio del cáncer a lo largo de los años se han realizado diferentes esfuerzos para mejorar la efectividad de los tratamientos, mediante nuevos medicamentos, métodos de entrega, variación en dosis y frecuencia de aplicación. Sin embargo, aún no se comprenden todos los mecanismos que ocurren en este proceso de entrega de fármaco. En el presente trabajo se desarrolla un modelo matemático por medio de simulación numérica en el software de COMSOL Multiphysics, el cual consiste en analizar el proceso de absorción de fármaco en tejido canceroso. Los resultados muestran información importante para entender las mecánicas detrás del proceso de entrega y absorción de fármaco.

Abstract

Over the years, various efforts have been made in cancer research to improve the effectiveness of treatments through new drugs, delivery methods and variations in dosage and frequency of administration. However, not all the mechanisms involved in this drug delivery process are yet fully understood. In this study, a mathematical model is developed using numerical simulation in the COMSOL Multiphysics software to analyze the process of drug absorption in cancerous tissue. The results provide important insights into the mechanisms underlying the drug delivery and absorption process.

Contents

Acknowledgements i
Dedication iii
Resumen v
Abstract vii
Contents ix
List of Figures xi
List of Tables xv
Introduction. 1
Chapter 1. Study of transcellular dissemination mechanisms in carcinoma type lesions. 5
1.1 Physical aspects of drug delivery to a cancerous nodule in the abdominopelvic cavity. 6
1.2 Disease spread. 8
1.3 Background 10
1.4 Cancer progression 11
Chapter 2. Advances in drug delivery systems for ovarian cancer therapy. 13
2.1 Intraperitoneal therapy 13
2.2 Nanoparticle-Based Drug Delivery Systems 15
2.3 Mechanisms of targeting 17
Chapter 3. Computational modeling of free-drug transport in a cancerous nodule within a microchannel. 19
3.1. Geometric parameters. 20
3.2 Numerical simulation 23
3.3 Numerical parameters of the model 24
3.3.1 Materials 24
3.3.2 Boundary conditions 25
3.4 Probe positioning 27
3.5. Mesh generation 29
3.6 Computational model parameters 34
4. Computational modeling of a nanoparticle-based drug delivery system in a cancerous nodule within a microchannel. 39
4.1 Numerical simulation 39
4.2 Numerical parameters of the model 40

4.2.1 Materials 40
4.2.2 Boundary conditions 40
4.3 Computational model parameters 43
4.4 Measurement approach 43
5. Identification of critical parameters and prediction of drug mass transfer dynamics. 51
5.1 Convection-diffusion model 51
5.2 Nanoparticle-based model 55
Conclusions. 61
Future work 62
References 63

List of Figures

Figure 1.1. Representation of ovarian cancer nodule metastases in the abdominopelvic cavity. From Rizvi, *et al.*, [9]. 6

Figure 1.2. Peritoneal cavity diagram [10] 7

Figure 1.3. Schematic diagram showing the peritoneal cavity (PC) on the left and the subperitoneal space (SPS) on the right. The dotted lines show some of these interconnections that allow the spread of the disease. Abbreviations for the peritoneal cavity: IC inframesocolic compartment, LP left paracolic recess, LS lesser sac, M Morison's pouch, RP right paracolic recess, RS right subphrenic space, and RV rectovesical space. Abbreviations for the subperitoneal space: B bladder, C colon, K kidney, L liver, P pancreas, S spleen, SB small bowel, and ST stomach. Taken from [8]..... 7

Figure 1.4. Routes of disease spread for viscera. Disease can cross the visceral peritoneum (solid arrow) to spread in the peritoneal cavity or follow the vessels and lymphatics (open arrow) to spread in the SPS. Taken from [8]. 9

Figure 1.5. Peritoneal cavity flow and recesses. Coronal CT image shows peritoneal carcinomatosis demonstrating peritoneal recesses. Tumor in the right subdiaphragmatic recess (black arrow) and Morison's pouch (double black arrows). Tumor (arrowheads) is also seen along the peritoneal reflection over the bladder (B). The white arrows show the continuity between the paravesical and paracolic recesses. The yellow arrows show the right and left paracolic gutters. Taken and modified from [8]. 9

Figure 1.6. Schematic representation of cancer cell detachment. From O.L. Torres-Saucedo [14]. 10

Figure 1.7. Representation of different interstitial flow rates on spheroid. From C. K. M. Ip, *et al.* [15]. 11

Figure 1.8. Alter fluid homeostasis in the tumor microenvironment. (I) Consistent features of tumor tissue are regions of high cancer cell density and abnormal microvascular networks. From M. Souri, *et al.*, [21]..... 12

Figure 2.1. Passive and active targeting of NPs to cancer cells. Taken from [28]. 18

Figure 3.1. Main cluster of cancerous cells with a) fractal dimension 2.3 and b) fractal dimension 2.7. Taken from [2]. 20

Figure 3.2. Representation of a cell from a cancerous nodule cluster using a solid sphere geometry. 21

Figure 3.3. Side view of selected 2.3 (left) and 2.7 (right) fractal dimension subclusters. Taken from [2]. 21

Figure 3.4. Assignment of materials to the domains of the microchannel geometry with the presence of a cluster with fractal dimension 2.3. 25

Figure 3.5. Fluid flow boundary conditions. Fluid flow velocity input ui=30 μm/s (blue) and pressure outlet po=0 Pa (red). Initial conditions are applied on all system domains. 26

Figure 3.6. Species transport boundary conditions.(a) Volumetric species source S_{PTX}=1.08435×10^{-5} ·step1(t) mol/m^3.(b) Species outflow.(c) Zero species concentration condition ci=0molm3..... 28

Figure 3.7. Domain point probe location in a microchannel with presence of cluster with a fractal dimension of 2.3. Views in the *y-z* plane (left), and the *x-y* plane (right) are shown. 29

Figure 3.8. Domain point probe location in a microchannel with presence of cluster with a fractal dimension of 2.7. Views in the *y-z* plane (left), and the *x-y* plane (right) are shown. 29

Figure 3.9. Comparison of concentration for fluid and tissue domain meshing iterations in probe location (-150, 0, 600) at t = 24 h. 34

Figure 3.10. Side view of the velocity distribution in a microchannel containing a cluster with a fractal dimension 2.3. A cross-section of the model with a *y-z* plane at x=-150 μm at t=24 h was used. 35

Figure 3.11. Concentration distribution in the plane at x=-150 μm at 24 h in microchannel with the presence of a cluster of fractal dimension 2.3. 36

Figure 3.12. Temporal variation of species concentration measured at four selected locations within a microchannel containing a cluster of fractal dimension 2.3. 36

Figure 3.13. Side view of the velocity distribution in a microchannel containing a cluster with a fractal dimension 2.7. A cross-section of the model with a *y-z* plane at x=-30 μm at t=24 h was used. 37

Figure 3.14. Concentration distribution in the plane at x=-30 μm at 24 h in microchannel with the presence of a cluster of fractal dimension 2.7. 37

Figure 3.15. Temporal variation of species concentration measured at four selected locations within a microchannel containing a cluster of fractal dimension 2.7. 38

Figure 4.1. Fluid flow boundary conditions. Fluid flow velocity input uin=30 μm/s (blue) and pressure outlet P_o = 0 Pa (red). Initial conditions are applied on all system domains. 41

Figure 4.3. Particle tracing on tissue surfaces and outlet in microchannel with presence of a cluster of fractal dimension 2.3. 44

Figure 4.4. Particle distribution and accumulation in microchannel model with fractal dimension 2.3 for the nanoparticle-based delivery model at t = 3 h and PW=4.5554×10^7.. 46

Figure 4.5. Particle distribution and accumulation in microchannel model with fractal dimension 2.7 for the nanoparticle-based delivery model at t = 3 h and PW = 1.02972×10^8. 46

Figure 4.6. Particle distribution and accumulation in microchannel model with fractal dimension 2.3 for the nanoparticle-based delivery model at t = 24 h and PW=4.5554×10^{7}. Views in the *y-z* plane (a), and the *x-y* plane (b) are shown. 47

Figure 4.7. Particle distribution and accumulation in microchannel model with fractal dimension 2.7 for the nanoparticle-based delivery model at t = 24 h and PW=1.02972×10^{8}. Views in the *y-z* plane (a), and the *x-y* plane (b) are shown. 48

Figure 5.1. Molar drug accumulation by volume over time in tissue domains with inlet velocity of 30 μm/s for microchannel model with fractal dimension 2.3 and 2.7 for the convection-diffusion drug delivery model. 52

Figure 5.2. Molar drug accumulation by volume over time in cancerous tissue domains with inlet velocity variation between 10-100 μm/s for microchannel model with fractal dimension 2.3 and 2.7 for the convection-diffusion delivery model. 52

Figure 5.3. Drug mass accumulation in tissue domains with inlet velocity variation for microchannel model with fractal dimension 2.3 and 2.7 for the convection-diffusion-based delivery model at t = 24 h. 53

Figure 5.4. Concentration value by tissue depth with inlet velocity of 30 μm/s for microchannel model with fractal dimension 2.3 (solid line) and fractal dimension 2.7, (scatter) for the convection-diffusion delivery model. 54

Figure 5.5. Concentration value comparison at 4 different tissue depths with variating inlet velocity between 10 - 100 μm/s for microchannel model with fractal dimension 2.3 (left) and fractal dimension 2.7 (right) for the convection-diffusion delivery model. 54

Figure 5.6. Numerical particle and nanoparticle accumulation over time in cancerous surfaces with inlet velocity of 30 μm/s for microchannel model with fractal dimension 2.3 for PW=4.5554×10^{7} and 2.7 for PW=1.02972×10^{8} with 450 nm nanoparticle size for the nanoparticle-based delivery model. 55

Figure 5.7. Numerical particle and nanoparticle accumulation over time in cancerous surfaces with variating inlet velocity between 10 – 100 μm/s for microchannel model with fractal dimension 2.3 for PW=4.5554×10^{7} and 2.7 for PW=1.02972×10^{8} with 450 nm nanoparticle size for the nanoparticle-based delivery model. 56

Figure 5.8. Numerical particle and nanoparticle accumulation in cancerous surfaces with inlet velocity variation for microchannel model with fractal dimension 2.3 for PW=4.5554×10^{7} and 2.7 for PW=1.02972×10^{8} with 450 nm nanoparticle size for the nanoparticle-based delivery model at t = 24 h. 57

Figure 5.9. Numerical particle and nanoparticle accumulation over time in cancerous surfaces with inlet velocity of 30 μm/s for microchannel model with fractal dimension 2.3 for PW= 7.6873×10^{10} and 2.7 for PW=8.58917×10^{10} with 60 nm nanoparticle size for the nanoparticle-based delivery model. 58

Figure 5.10. Numerical particle and nanoparticle accumulation in cancerous surfaces with inlet velocity variation for microchannel model with fractal dimension 2.3 for PW= 7.6873×10^{10} and 2.7 for PW=8.58917×10^{10} with 60 nm nanoparticle size for the nanoparticle-based delivery model at t = 24 h. 58

Figure 5.11. Drug mass accumulation in cancerous surfaces with inlet velocity variation for microchannel model with fractal dimension 2.3 and 2.7 with 450 nm nanoparticle size for the nanoparticle-based delivery model at t = 24 h. 59

List of Tables

Table 2.1. Clinical dose levels and corresponding total paclitaxel doses for ovarian cancer therapy. 15

Table 2.2. Effects or responses of the immune system according to different sizes of NPs. 16

Table 2.3. Representative nanoparticles systems reported for paclitaxel encapsulation. Extracted from M. Souli, *et. al.* [21]. 17

Table 3.1. Numerical parameters of the materials. 24

Table 3.2. Concentration point probes location for 2.3 and 2.7 fractal dimension cluster models. 27

Table 3.3. Mesh size characteristics for tissue domains. 30

Table 3.4. Mesh size iteration for fluid domain analysis. 30

Table 3.5. Number of elements and simulation time of mesh size iteration for fluid domain analysis. 30

Table 3.6. Maximum velocity for every iteration of fluid mesh size. 31

Table 3.7. Concentration at probe for every iteration of fluid mesh size. 31

Table 3.8. Mesh size iteration for tissue domain analysis. 32

Table 3.9. Number of elements and simulation time of mesh size iteration for tissue domain analysis. 32

Table 3.10. Maximum velocity for every iteration of tissue mesh size. 32

Table 3.11. Concentration at probe for every iteration of tissue mesh size. 33

Table 3.12. Element size parameters for the mesh. 35

Table 3.13. Concentration point probes values on clusters with varying fractal dimension. 38

Table 4.1. Mass data for drug and nanoparticles. 42

Table 4.2. Element size parameters for the mesh. 43

Table 4.3. Particle weighting factors and release parameters for nanoparticle delivery. 44

Table 4.4. Nanoparticle delivery and drug distribution at 24 h for varying particle weighting factors and release parameters for the model with fractal dimension 2.3. 45

Table 4.5. Nanoparticle delivery and drug distribution at 24 h for varying particle weighting factors and release parameters for the model with fractal dimension 2.7. 45

Introduction.

Cancer is a progressive disease that consists of an uncontrolled division of cells, it begins when a cell manages to avoid cell division restrictions and forms a tumor through abnormal proliferation.

The determination of malignancy of a tumor is the ability to invade and metastasize. Metastasis refers to the ability of cells to leave a primary tumor, travel through a dissemination route to distant tissue and form an additional tumor. This phenomenon presents a major clinical relevance, because 90% of cancer deaths can be attributed to metastases and not to primary tumors [1,18]. Particularly, ovarian cancer propagates through transcellular dissemination which metastasis are associated with a higher of mortality and morbidity due to the capacity to affect nearby organs [17].

Angiogenesis is the first phase of metastasis and plays a key role in tumor cell proliferation and growth of the neoplasm, usually beginning once the mass reaches a certain volume (1-2 mm^3) [5].

There are three main routes of dissemination by which metastasis can occur, these being transcellular, lymphatic and hematogenous dissemination.

Transcellular dissemination is the most common route of propagation in patients with ovarian carcinomas, being responsible for peritoneal metastases observed in about 70% of patients [5]. Peritoneal ovarian carcinomas metastases are commonly associated with a higher mortality and morbidity rate due to their capacity to affect nearby organs, such as those in the abdominal cavity and gastrointestinal tract [6].

According to the World Health Organization in 2020, cancer is one of the leading causes of death worldwide, amounting to almost 10 million deaths [17]. Due to the nature of the conventional treatments, mainly chemotherapy, cancer patients undergo a process of physical strain accompanied by a deterioration of their general health, due to the side effects generated by drug administration. Over the years, a need to develop more effective treatment methods has arisen, leading to the development of drug delivery systems.

Several drug delivery systems can be used for intraperitoneal therapy, with varying levels of effectiveness. Nanoparticle based systems provide a reliable alternative that allows drugs to be administered to specific areas.

Due to the importance of this topic, it is proposed to generate a numerical model aimed at maximizing the drug concentration in the tumor tissue of a cancerous nodule in the abdominal region, while maintaining low flow shear stress to avoid causing cell detachment in the nodule. The model aims to help understand the mechanical implications of the drug delivery process, allowing for further study of this phenomena.

The effectiveness of a nanoparticle based drug delivery system for mass transfer process from interstitial fluid to cancerous tissue can be accurately modeled using a numerical approach based on principles of convection and diffusion. By simulating key parameters such as permeability, growth pattern, stage of development and external conditions, the numerical model provides valuable insights into the spatial and temporal distribution of drug-loaded nanoparticles and their payload within the tissue.

This thesis addresses the analysis of a drug mass transfer process to cancerous tissue using a numerical model of a cancerous nodule with two stages of development represented with fractal dimension. The

corresponding simulation was performed using COMSOL Multiphysics software. The model consists of a channel with a square cross section and on one of its inner surfaces, the cells are arranged in such a way that they form an assembly adhered to the wall, which is called a cluster. A constant flow of biological fluid is induced through the channel and the drug transfer process from biological flow to tissue is studied. The results reveal important information that helps us understand the physical mechanics underlying the process of drug delivery and absorption. Here, stage of development and velocity of the fluid play a crucial role, which can aid the drug accumulation dynamics by cancerous tissue. This thesis is organized as follows:

Chapter 1	**Study of transcellular dissemination mechanisms in carcinoma type lesions.** This chapter introduces the physical and biological mechanisms underlying cancer metastasis, with emphasis on the transcellular dissemination process for carcinoma-type lesions. A review of the physical aspects of the abdominal cavity and drug delivery via interstitial fluid. Furthermore, the current understanding of cancer progression and the influence of hydromechanical factors on metastatic dissemination is summarized.
Chapter 2	**Advances in drug delivery systems for ovarian cancer therapy.** This chapter reviews the current state of the art in ovarian cancer drug delivery systems, with particular emphasis on intraperitoneal chemotherapy and nanoparticle-based drug delivery, and the transport mechanisms governing drug distribution and accumulation in the peritoneal cavity. .
Chapter 3	**Computational modeling of free-drug transport in a cancerous nodule within a microchannel.** This chapter describes the development of the convection-diffusion model for free-drug transport in a cancerous nodule of the model, the use of governing equations, numerical parameters of the simulation and the boundary conditions governing the model are presented, along with a mesh independence study required to outline the base behavior of the numerical model.
Chapter 4	**Computational modeling of a nanoparticle-based drug delivery system in a cancerous nodule within a microchannel.** This chapter describes the development of the nanoparticle-based transport model within the same computational framework. The particle tracing methodology, properties of the nanoparticles, the release and particle weighting strategy for the numerical configuration, and boundary conditions, are presented. Additionally, initial parameter are evaluated to establish the baseline behavior of the nanoparticle model.

Chapter 5	**Identification of critical parameters and prediction of drug mass transfer dynamics.** Presents a parametric analysis of both computational models to identify governing variables for the drug accumulation and species transport mechanics.

General Objective

To propose a model through numerical analysis of the drug mass transfer to biological tissue, originated by interstitial fluid currents in a cancerous nodule model, to reach a required drug concentration to disable cancer tissue development.

Specific Objectives

- To model a microchannel with the presence of a representative obstacle possessing a growth pattern that simulates that of a cancerous nodule with porosity characteristics.
- To model drug mass transfer between biological fluid and tissue by diffusive mechanisms.
- To propose a mathematical model of drug delivery using nanoparticles.
- To identify the critical parameters that significantly influence the process of drug mass transfer in biological tissue.
- To predict behavior of critical parameters for drug absorption into the biological tissue.

Chapter 1. Study of transcellular dissemination mechanisms in carcinoma type lesions.

Cancer is a degenerative disease, meaning that the condition of the disease worsens with time. It consists of an uncontrollable division of affected body cells, which begins when a cell manages to free itself from restrictions on cellular division, generating progeny that will also present abnormal proliferation [1]. The malignancy of the tumor is determined by the capacity for invasion and metastasis.

The start-up phase of metastasis process generally begins once a tumor mass reaches a volume of around 1-2 mm^3 and undergoes a process known as angiogenesis [2]. Angiogenesis is a process where new blood vessels develop from existing ones, it is a process not only related to organ function and development but also to tumor growth. Cancerous cells exhibit enhanced metabolism and demand a much larger supply of oxygen. These requirements stimulate tumor angiogenesis and fulfill an essential prerequisite needed to trigger the metastatic process. [3].

Cancer manifests itself in people due to changes during cell reproduction processes. Affected cells tend to reproduce at a faster rate than normal cells, generating an abnormal buildup of cells, known as tumors [4]. Tumors inhibit normal bodily functions of organs they reside in and can spread through the different dissemination routes that can lead to metastasis:

- Hematogenous dissemination, involving transport through the blood circulation,
- Lymphatic dissemination, involving transport through the lymphatic system; and
- Transcellular dissemination, involving transport across the abdominal and thoracic cavities.

In general, the circulatory system is considered the main avenue for propagation to distant organs, since lymphatic vessels provide a pathway to local lymph nodes, which then spread through the blood.

This study focused on ovarian carcinomas, in which transcellular dissemination is the most common route of spread in patients [5]. Transcellular metastases are associated with higher mortality and morbidity rates due to their ability to affect nearby organs, those present in the abdominal cavity [6]. In addition, these metastases are often associated with the production of malignant ascites, which consist of the accumulation of fluid in the abdominal cavity [6]. During the stage of metastasis, cancerous cells interact with various biochemical and biophysical factors in the tumor microenvironment (TME), making it a priority to investigate the responses of cancerous cells to the different stimuli present in the TME. The biophysical forces, produced by the induced flow of ascitic fluid, can provide mechanical effects on tumors and the surrounding microenvironment, having a significant role in the process of cancer cell metastasis [7].

In biological systems, a laminar flow regime prevails in fluids, which generally occurs in blood, lymphatic, and interstitial fluid. Tumor cells experience shear stress mainly from interstitial and blood flow during the metastatic stage [7].

The continuous flow of biological fluid circulating in the abdominal cavity and through tumor tissue is known as interstitial flow. Malignant ascites develop frequently in patients with advanced stages of metastatic ovarian cancer and contribute to tumor proliferation, invasion, and metastasis through various cellular, acellular and biophysical mechanisms, which hinders the efficacy of conventional therapies [2,5].

Figure 1.1 shows a representation of the ovarian metastatic process, which involves four common sites in the abdominopelvic cavity: (1) cul-de-sac, (2) right inframesocolic space, (3) left inframesocolic space, and (4) right paracolic gutter. This spread pattern is influenced by interstitial flow pathways represented by the blue arrows and allows nodules to reach nearby areas (2-3), as well as distant organs such as the liver.

1.1 Physical aspects of drug delivery to a cancerous nodule in the abdominopelvic cavity.

The peritoneal cavity is a potential space between the visceral and parietal layers of the peritoneum; this cavity as shown in Figure 1.2 is located in the abdomen and completely or partially surrounds the splanchnic organs. The peritoneal cavity contains a small amount of interstitial fluid (about 100 mL), which helps lubricate the abdominal organs, for movement and expansion of the intestine [8]. The peritoneum is a serous membrane that lines the abdominal cavity and secretes the fluid that lubricates the organs.

As shown in Figure 1.3, there are two spaces in the abdomen and pelvis, the peritoneal cavity (PC) and the subperitoneal space (SPS), and these are separated by the peritoneum and remain separated, each as a single continuous space. The peritoneal cavity is one continuous space with interconnecting recesses, some of which are shown in the figure. The subperitoneal space is also one continuous space containing all the abdominal pelvic organs which are interconnected via ligaments and mesenteries. Dotted lines show some of these interconnections which allow for disease spread [8].

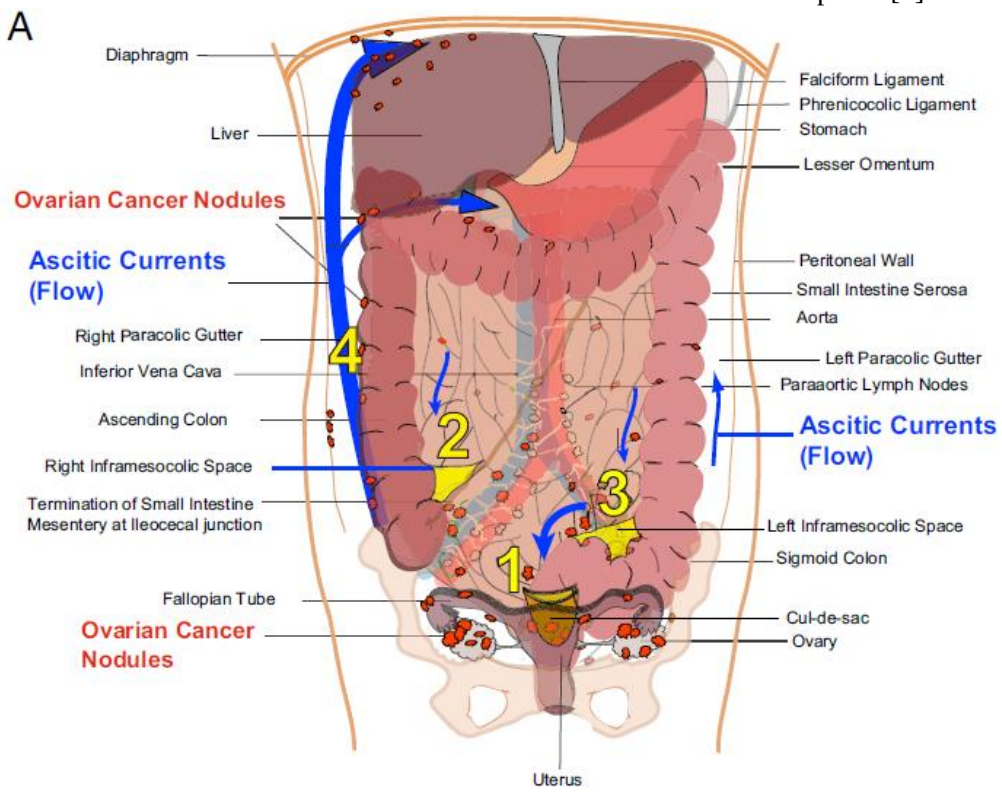

Figure 1.1. Representation of ovarian cancer nodule metastases in the abdominopelvic cavity. From Rizvi, *et al.*, [9].

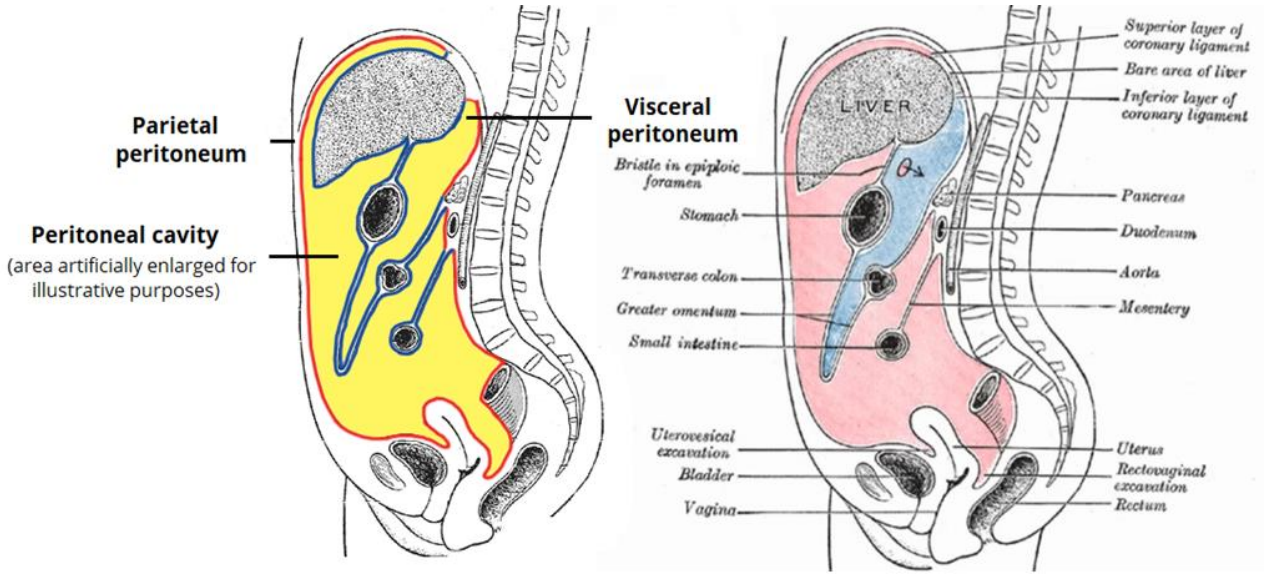

Figure 1.2. Peritoneal cavity diagram [10]

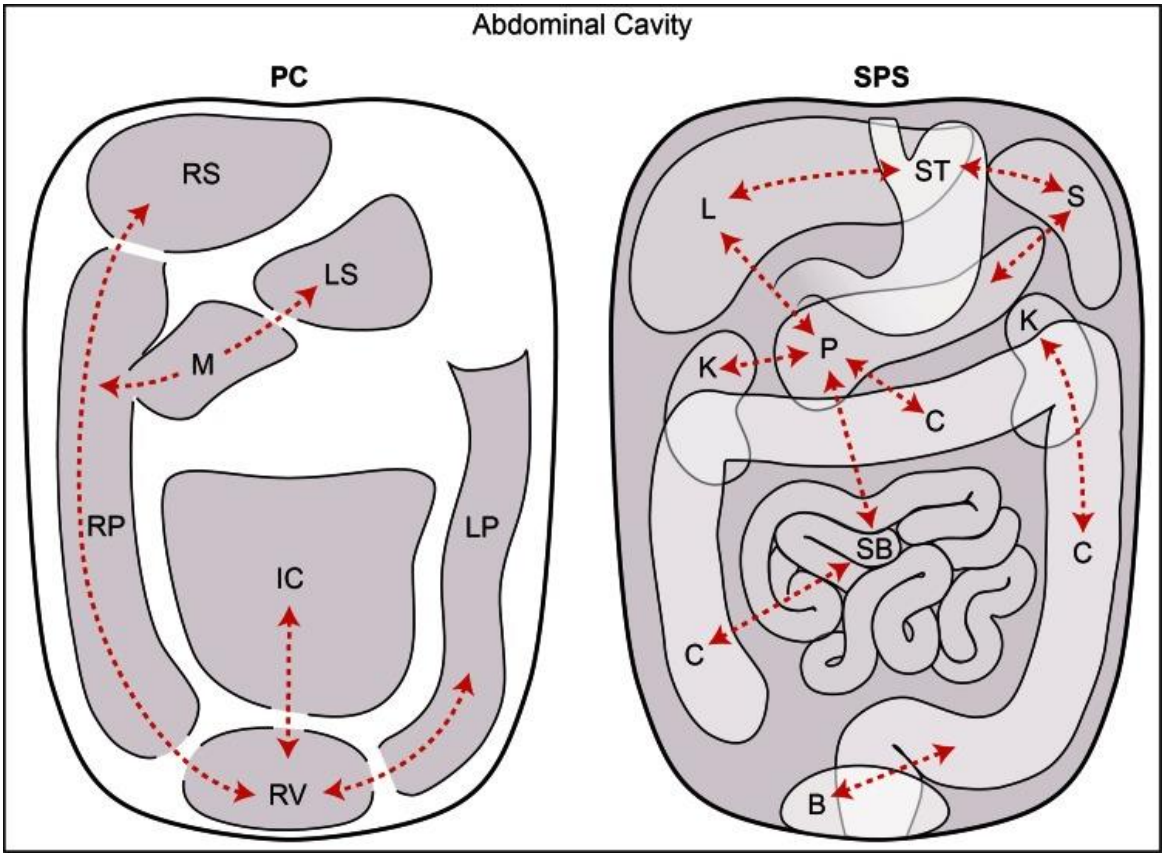

Figure 1.3. Schematic diagram showing the peritoneal cavity (PC) on the left and the subperitoneal space (SPS) on the right. The dotted lines show some of these interconnections that allow the spread of the disease. Abbreviations for the peritoneal cavity: IC inframesocolic compartment, LP left paracolic recess, LS lesser sac, M Morison's pouch, RP right paracolic recess, RS right subphrenic space, and RV rectovesical space. Abbreviations for the subperitoneal space: B bladder, C colon, K kidney, L liver, P pancreas, S spleen, SB small bowel, and ST stomach. Taken from [8].

The organs located in the abdominal cavity are referred to as splanchnic organs and include the stomach, small bowel, colon, pancreas, liver, and spleen.

Splanchnic blood flow includes perfusion to these organs, primarily focused on the liver, spleen, and intestines, and is often also associated with renal blood flow. Because hepatic and renal blood flow is considerably greater than metabolic requirements, a substantial fraction of normal splanchnic blood flow can be diverted to active muscle and the skin during exercise and heat exposure, thus reducing the required cardiac output [11].

For determination of hepatic blood flow, blood enters the liver through the portal vein and hepatic artery and exits through the hepatic veins. Several techniques have been developed to measure flow in these vessels.

Hepatic blood flow can be quantified using several methods based on Fick's principle. These methods involve the injection of a dye, indocyanine green (ICG), and the quantification of the rate at which it is extracted. As ICG is extracted exclusively from the bloodstream by the liver [11], the system can be analyzed under steady-state conditions using a continuous infusion approach in a peripheral vein, which becomes uniformly mixed with circulating blood. The ICG concentration entering the liver is measured from a peripheral vein as input and from a hepatic vein as output [11].

As the project proposes an analysis of a drug delivery system in the abdominopelvic cavity, blood flow does not enter into relevance; instead, interstitial fluid flow serves as the transport medium for drug concentration inside of the peritoneal cavity. Ovarian carcinomas can metastasize to the peritoneal cavity in advanced stages of ovarian cancer (Stage III or IV).

Ovarian cancer cells can spread to the peritoneum by detaching from the primary tumor and floating within the peritoneal fluid. In addition, direct local invasion can occur from the primary ovarian tumor to neighboring pelvic organs, such as the bladder or colon.

1.2 Disease spread.

Since the organs in the abdominal cavity are subperitoneal, the subperitoneal space (SPS) is a natural pathway for the spread of the disease from one organ to the other due to the continuity of the space, as illustrated in Figure 1.4. Disease can spread bidirectionally within the subperitoneal space using pathways created by normal structures. In addition, transperitoneal spread occurs when the disease spreads from the subperitoneal space to the peritoneal cavity by crossing the peritoneal lining [8].

The transverse mesocolon divides the peritoneal cavity into supramesocolic and inframesocolic compartments. Peritoneal fluid is drawn into the upper abdomen by low subdiaphragmatic pressures and is drawn into the pelvis under the influence of gravity [8].

Fluid travels from the pelvis to the abdomen via paracolic gutters and from the abdominal infracolic compartment to the pelvis, as presented in Figure 1.5.

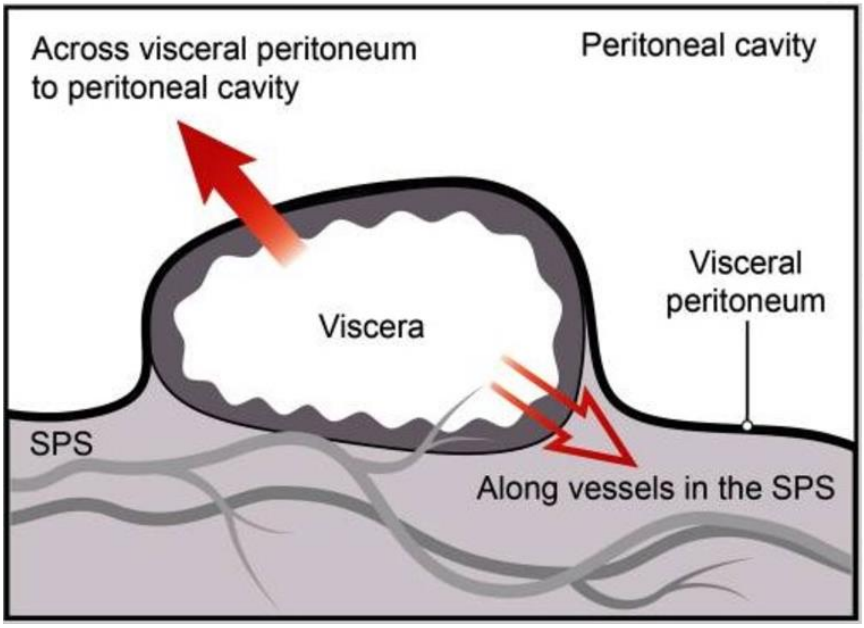

Figure 1.4. Routes of disease spread for viscera. Disease can cross the visceral peritoneum (solid arrow) to spread in the peritoneal cavity or follow the vessels and lymphatics (open arrow) to spread in the SPS. Taken from [8].

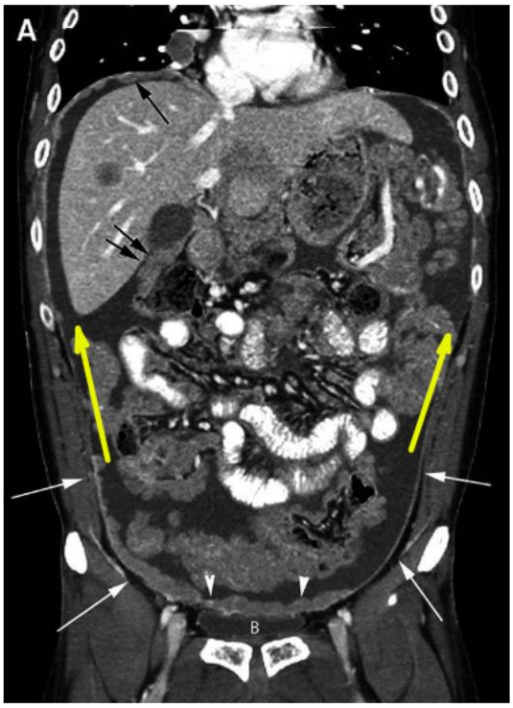

Figure 1.5. Peritoneal cavity flow and recesses. Coronal CT image shows peritoneal carcinomatosis demonstrating peritoneal recesses. Tumor in the right subdiaphragmatic recess (black arrow) and Morison's pouch (double black arrows). Tumor (arrowheads) is also seen along the peritoneal reflection over the bladder (B). The white arrows show the continuity between the paravesical and paracolic recesses. The yellow arrows show the right and left paracolic gutters. Taken and modified from [8].

1.3 Background

Over the years, several advances have allowed us to better understand the influence of hydromechanical factors on the metastasis process of ovarian cancer tumor cell. Some of them are presented below.

In 2013, Rizvi, *et al.*, [9] used a microfluidic platform using 3D ovarian cancer nodules to investigate the role of fluidic forces as modulators of the metastasis process of ovarian cancer nodules. They evaluated the changes presented in morphological, genetic, and protein profiles under continuous laminar flow, demonstrating that fluidic streams induce aggressive and motile nodule behavior.

Shields *et al.* [12], applying a constant interstitial flow, found that this flow increases the migratory potential of metastatic cancer tumor cells. Subsequently, Polacheck, *et al*. [13] with a model based on the work of Shields *et al*. [12] showed that the direction of tumor cell migration depends on the strength of the flow and the cell density.

The migratory potential of metastatic cancer tumor cells can lead to cancer cell detachment due to the influence of interstitial flow, as shown in Figure 1.6.

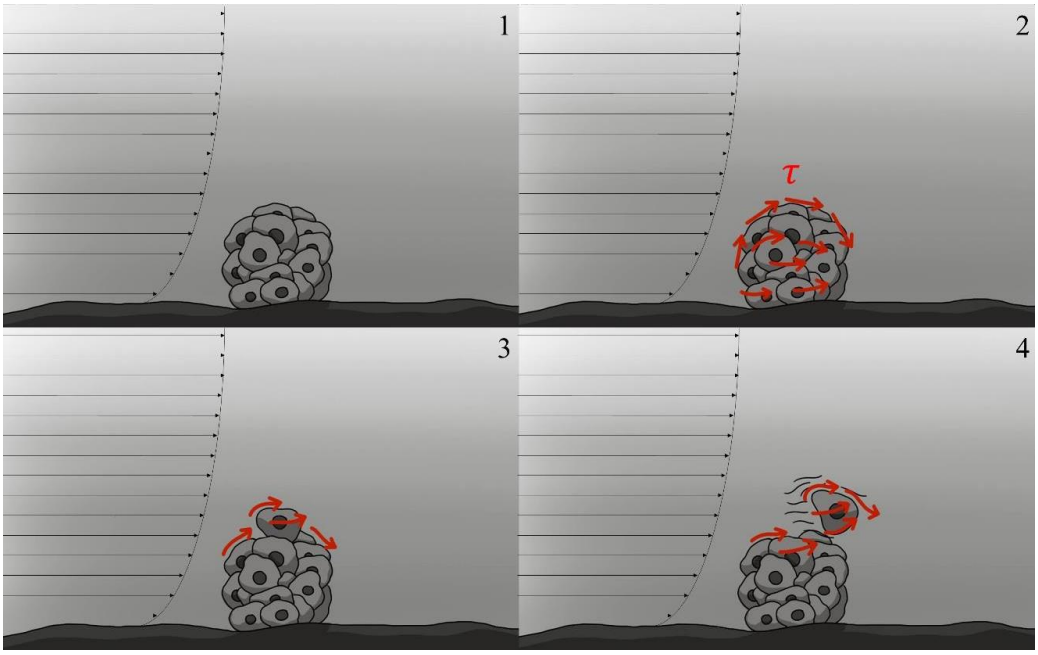

Figure 1.6. Schematic representation of cancer cell detachment. From O.L. Torres-Saucedo [14].

Fig 1.6.1 provides a view of a cancerous nodule in a channel and an interstitial flow stream with a rightward direction, causing flow shear stress around the nodule in Fig. 1.6.2. Fig. 1.6.3 begins to show the first effects of cell detachment, while in Fig 1.6.4 the detachment of the entire cell can be observed.

In 2016, C. K. M. Ip, *et al*. [15] performed a numerical flux procedure in a model based on work by Rickard and Rizvi *et al*. [5]. Spheroids within the channels experimented a mean shear stress of 3.902×10^{-4} Pa y de 3.902×10^{-4} Pa when permeated by a continuous laminar flow of 30.1 µl/h or 301.2 µl/h for 24 h at a temperature of 37 °C, respectively. Figure 1.7 shows the result of the numerical simulation in ANSYS software.

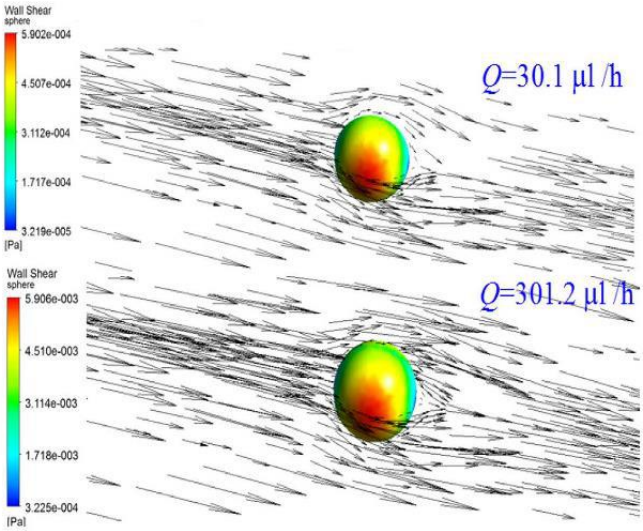

Figure 1.7. Representation of different interstitial flow rates on spheroid. From C. K. M. Ip, *et al.* [15].

In 2020, O. L. Torres-Saucedo [14] deepened in the study of shear forces, obtaining a great similarity between the forces calculated experimentally and those obtained by numerical simulation. As part of this study, in 2021 D. A. Robledo [16] further studied the velocity fields and mechanical stresses caused by microfluids subjected to oscillatory changes in a cancerous nodule model, considering porous material.

Afterwards, in 2023 J. A. Monasterio [2] developed a more complex model with fractal dimension properties, simulating the growth pattern of a cancerous nodule in two different stages and approximating a value for the shear stress profile, using the velocity profiles generated in the channel.

Several efforts have been made to better understand the role of hydromechanical factors in the process of ovarian cancer cell metastasis, revealing that both migratory behavior and direction of tumor cell migration are strongly influenced by the strength and direction of interstitial flow, among other external parameters.

1.4 Cancer progression

After attachment to the tissue and initial growth, cancerous neoplasms develop new blood vessels, as an integral part of angiogenesis, allowing the tumor to grow beyond 2 mm in size [20] after vascularization occurs, a stage shown in Figure 1.8. Angiogenesis also allows for a genetic level switch to occur, which is critical in tumor progression in the later stages [19].

Depending on the level of analysis, tumor evolution involves phenomena occurring on different scales. The microscopic, mesoscopic and macroscopic scales can be related to sub-cellular, cellular, and tissue levels, respectively. Macroscopic scale focuses on tissue-level behavior and relates associated processes to continuum systems, such as cell migration, convection and diffusion of nutrients, mechanical effects, interaction with tissues and diffusion of metastases [20].

In the macroscopic stage, tumor progression can be described using mass balance and reaction–diffusion equations, derived from the principles of continuum mechanics.

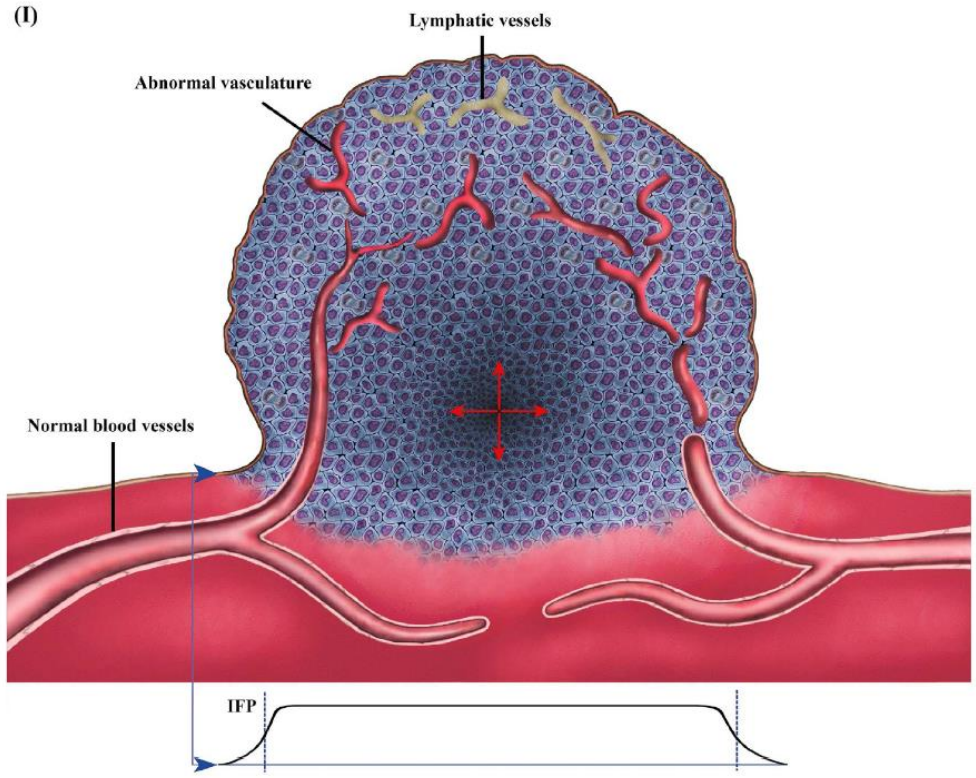

Figure 1.8. Alter fluid homeostasis in the tumor microenvironment. (I) Consistent features of tumor tissue are regions of high cancer cell density and abnormal microvascular networks. From M. Souri, *et al.*, [21].

As reviewed, the movement of fluids, molecules, and particles within the tumor microenvironment has numerous biophysical and clinical implications, as cancer cell proliferation depends on the distribution and clearance of several molecules, transport of these plays a critical role in tumor growth, angiogenesis, metastasis, and therapy [20]. The transport of molecules in solid tumors occurs through both diffusion and convection and is highly dependent on the physicochemical properties of the diffusing species as well as those of the surrounding medium.

Understanding the physical factors involved in interstitial transport is of vital importance on in the development of strategies to improve drug delivery in malignant carcinomas. This will be explored in the next chapter.

Chapter 2. Advances in drug delivery systems for ovarian cancer therapy.

Current optimal management for advanced stages of ovarian cancer includes surgery and a chemotherapy program with carboplatin and paclitaxel, generally administered for six cycles [19]. While the chemotherapy program has been validated by Phase III trials, there are multiple variations utilized for each patient in clinical practice, contributed by gaps in knowledge and disagreement between practitioners.

Platinum compounds are typically administered intravenously (IV) and remain the most dominant agents currently utilized in the treatment of ovarian cancer, some of the downsides of the use of platinum-based drugs are the development of cancer cell resistance, as well as the general impairment of the patient, which includes a series of effects such as nausea, vomiting, nephrotoxicity, myelosuppression, tinnitus, hearing loss, peripheral neuropathy, hyperuricemia, and hypersensitivity [22].

The therapeutic index of platinum-based chemotherapy has improved by determining the optimal dose, schedule, sequence, and duration of treatment over the years. With paclitaxel, shorter infusions (<3 h) are generally better tolerated in patients, as longer infusions (≥24 h) increase mucosal and bone marrow toxicity without improved efficacy [19]. Weekly scheduling of shorter infusions allows a higher cumulative dose delivery while avoiding hematologic toxicity and alopecia.

High-grade serous ovarian cancer is characterized by increased production of vascular endothelial growth factor (VEGF), which triggers abnormal tumor angiogenesis, contributing to high interstitial pressure and ascites production [19], enabling fluid-induced mechanical effects on the tumor in the abdominal cavity.

In recent years, there have been no major changes in the therapeutic strategy for advanced-stage ovarian cancer. In addition to the development of new cytotoxic agents and variations in treatment protocols, the vast majority of patients are initially subjected to maximal cytoreductive surgery and a carboplatin and paclitaxel chemotherapy program [19]. This approach remains the standard treatment regimen.

2.1 Intraperitoneal therapy

One of the alternatives developed to increase the effectiveness of the chemotherapy program is the use of intraperitoneal (IP) drug delivery compared to the standard intravenous (IV) route of administration.

Direct delivery of drugs in the abdominal cavity has long been explored for the treatment of malignant neoplasms involving this space; however, the idea did not gain relevance in the early days due to the antineoplastic agents available at the time, many of which had low efficacy against carcinomas within the peritoneal cavity, and showed a high level of toxicity to the system [19].

The primary theoretical advantage of IP antineoplastic drug delivery is the prolonged exposure of cancer cells within the abdominal cavity to anticancer agents at higher concentrations than is achievable with IV administration. In general, the longer an agent remains biologically active within the peritoneal cavity, the greater the expected therapeutic benefit.

Additional benefits may be observed for antineoplastic agents that undergo extensive metabolism in the first passage through the liver, such as paclitaxel. However, some limitations arise in the use of IP drug delivery, as the toxicity associated with this route may prevent the use of certain agents. Both doxorubicin and mitoxantrone have been shown to produce excessive local toxicity when administered intraperitoneally, including pain, adhesion formation, and bowel obstruction [19].

Therefore, the applicability of IP delivery is limited, and its use must be evaluated on an individual basis. In patients with metastatic tumors at sites outside the peritoneal cavity, the drug-containing fluid cannot consistently reach these regions, thus reducing the overall effectiveness of this route. Extra-peritoneal metastatic sites must still be treated via IV delivery.

In contrast to IV drug administration, there is no guarantee that the dug instilled into the peritoneal cavity will distribute uniformly due to the ever-changing geometry of the compartment due to movement and the presence of adhesions or presence of swollen tissues. Clinical trials have shown that a volume of on to two liters of solution ensures that no disease progression or recurrence occurs [19], however this amount is limited by the condition of the patient and the extent of toxicity effects exhibited.

Ovarian cancer is closely associated with the abdominal cavity, as tumors are present in this body compartment in most cases. Consequently, IP therapy has emerged as an attractive alternative to conventional IV treatment. One limitation of IP administration is tumor size, as studies have shown that chemotherapeutic agents can only penetrate 1-2 mm into tumor nodules from the surface; therefore, the IP route is deemed ineffective for larger tumors [19].

Despite conjunct efforts, the IP therapy has not gained enough widespread acceptance by the oncology community due to toxicity levels and the difficulty in implementing the IP regimen.

Cisplatin, carboplatin and paclitaxel, are currently among the most widely used agents for IP therapy [19]. Paclitaxel is frequently administered as a standalone antineoplastic agent or in combination with other drugs; therefore, the present study focuses on the evaluation of standalone paclitaxel as an anticancer therapy agent.

Paclitaxel is a natural compound with antitumor activity. It presents as a white to off-white crystalline powder with the empirical formula $C_{47}H_{51}NO_{14}$ and a molecular weight of 853.9 g/mol [23]. The compound is highly lipophilic, insoluble in water, and melts at around 216 to 217 °C [24]. Generally used in the treatment of Kaposi's sarcoma and small cell lung cancer, advanced ovarian carcinoma, and breast cancer [23,24].

Paclitaxel is commercially available under the name TAXOL, in multidose vials containing 30 mg, 100 mg, and 300 mg [24], which are selected according to the prescribed treatment regimen. Dose levels generally administered for standalone paclitaxel therapy range between 60 and175 mg/m^2. This body surface area (BSA) dosing is used in conjunction with Equation 2.1 to determine the total dose to be administered to a patient.

$$\text{Total dose (mg)} = \text{Dose (mg/m}^2\text{)} \times \text{BSA (m}^2\text{)} \tag{2.1}$$

BSA is commonly used to establish the appropriate dosage of anticancer drugs. Accurate dosing helps guarantee therapeutic efficacy while reducing the risk of toxicity [24]. According to V. Danesi, *et al.* [25], an overall mean value for BSA is 1.75 m^2 in a study population of 13,036 male and female patients with various types of cancers, corresponding to 1.66 m^2 in females and 1.87 m^2 in males.

Considering a BSA value of 1.66 m^2, the clinical level doses for ovarian cancer therapy are displayed in Table 2.1.

Table 2.1. Clinical dose levels and corresponding total paclitaxel doses for ovarian cancer therapy.

Dose level (mg/m^2)	Total dose (mg)	Clinical context
60	99.6	Lower clinical dose; tipically used for clinical trials or as a second-line treatment.
80	132.8	Early option for stage III ovarian cancer or in follow-up regimen.
135	224.1	Intermediate dose. Late stage III or early stage IV ovarian cancer.
175	290.5	Upper clinical dose level. Commonly used on advanced stage IV ovarian cancer.

These values define a clinically relevant paclitaxel dose range of approximately 100 to 300 mg, commonly used in oncological practice.

Anticancer agents may be administered through different infusion times, with 3-h and 24-h being the most commonly employed. Specifically for paclitaxel, an infusion time of 3 hours is favored over 24 hours, as it provides comparable clinical outcomes in terms of response rate, time to disease progression, and mean survival, while being associated with reduced toxicity [24].

Pharmacokinetic studies in animal models suggest that IP-administered paclitaxel is eliminated from the peritoneal cavity in less than 24 h [26].

Drug delivery systems (DDS) are defined as routes by which drugs are delivered to a variety of biological structures, such as organs, tissues, cells and subcellular organs. Purposes include drug release and absorption through a variety of drug carriers. These are used to transport therapeutic drugs in the body; usually designed to i) improve aqueous solubility and chemical stability of active agents, ii) increase pharmacological activity, and iii) reduce side effects [27]. The main objective of DDS is to provide and maintain certain therapeutic concentrations of drugs at the target biological site.

2.2 Nanoparticle-Based Drug Delivery Systems

Cancer treatment has advanced significantly in recent years, leading to the development of new drug delivery systems. Among these, nanoparticle-based systems have shown promising results in cancer treatment, particularly for the targeted delivery of therapeutic agents.

Nanoparticle-based (NP-based) drug delivery systems have shown various advantages in cancer therapy, including improved pharmacokinetics, enhanced tumor targeting, and reduced side effects and drug resistance. Due to their size and surface characteristics, NP-carriers can increase the mean useful life of drugs and promote accumulation in tumor tissues [28].

NPs in cancer treatment are limited by certain geometric characteristics such as sizes, shapes, and surface properties as these aspects have a major influence on the efficiency of NP-drug delivery and

control therapeutic efficacy [29]. In particular, the size parameter can have different effects in the immune system, as shown in Table 2.2.

Drug encapsulation within nanoparticles or other carrier systems can provide effective platforms for anticancer agents, extending local residence time in the peritoneal cavity while reducing systemic toxicity [26].

Table 2.2. Effects or responses of the immune system according to different sizes of NPs.

Particle diameter	Possible effect	Reference
$\leq 1-2$ nm	Can leak from normal vasculature to damage normal cells,	[28]
≤ 10 nm	Can be filtered by kidneys	[28]
$10-100$ nm	Generally suitable for cancer therapy, can effectively deliver drugs and achieve enhanced permeability and retention (EPR) effect.	[28]
≥ 100 nm	Likely to be cleared from circulation by phagocytes	[28, 30]

NP-based drug delivery systems provide a good platform for in vivo delivery of many antitumor drugs, such as doxorubicin and paclitaxel, among other chemotherapeutic agents, as well as nucleic acids [28]. In particular, organic NPs have been explored and are made of several types of materials, such as liposomes, which consist of an outer lipid layer and a core entrapping either a hydrophobic or a hydrophilic drug.

Polymer based NPs are a particularly popular type of nanoparticle, because of their biocompatibility and biodegradation capabilities, and a solid deployment of the EPR effect. Polylactic-co-glycolic acid (PLGA), is commonly used as polymeric chemotherapy NP, due to their ability to load and deliver therapeutic agents, as well as their increasing accessibility in the market [28].

The prolonged intraperitoneal residence time observed with nanoparticle-based drug delivery does not arise from sustained administration, but rather from the decoupling between drug release kinetics and peritoneal clearance.

NPs are rapidly gathering interest as a reliable tool for IP delivery; however, several physical challenges need to be overcome for IP chemotherapy, such as poor drug penetration into tumor tissues or with the handling of pressure gradients caused by interstitial fluid.

Microparticles have recently emerged as an alternative for IP administration, whose sizes range from 4 to 6 μm, and 47 μm, as these particles are cleared relatively slowly and present a better drug retention capabilities, with the noticeable downside of possibly causing peritoneal adhesions [26].

Several NP-based strategies for drug loading have been reported, using both conventional and microfluidic approaches, which affects the effective load that a certain particle can carry. For the purposes of the present study, only NP systems encapsulating paclitaxel were selected, as this agent constitutes the focus of the proposed IP delivery model. The corresponding nanoparticle formulations were extracted from M. Souli, *et al.* [21] and summarized in Table 2.3.

Table 2.3. Representative nanoparticles systems reported for paclitaxel encapsulation. Extracted from M. Souli, *et. al.* [21].

Loading strategy	Nanocarrier material	Size range (nm)	Drug loading (%)
Pre-loading	Polymer	60-450	42.6
		40-175	38-58.5
	Sylica	58.6	59.2
Co-loading	Polymer	98-110	8.67-28.32
Post-loading	Silica	130-190	5.7-51.9

2.3 Mechanisms of targeting

Targeting cancer cells is an important characteristic of nanocarriers used for drug delivery, as it improves therapeutic efficacy while protecting normal cells from cytotoxicity [28]. Targeting mechanisms can be divided into two categories, passive targeting and active targeting.

Passive targeting is designed to take advantage of the different mechanical and superficial characteristics of tumor and normal tissue, allowing drugs to be delivered to the target site to play a therapeutic role. In Figure 2.1, the passive targeting mechanics are represented in the lower part of the figure, nanoparticles infiltrate in normal and cancer cells due to the fluid velocity field and pressure gradients. A higher concentration of particles is able to enter in tumor tissue, due to the defective angiogenesis state, which is part of the metastasis process. This enables all macromolecules to leak from newly formed blood vessels supplying the tumor and accumulate within tumor tissue, including pharmacological NPs. In addition, poor lymphatic drainage in cancer-associated tumor tissue allows for increased retention of pharmacological NPs, which enables the nanocarriers to release their contents into tumor cells.

These processes cause enhanced permeability and retention (EPR) effect, which together with the tumor microenvironment, form the major driving forces of passive targeting. Limitations in passive targeting include non-specific drug distribution, non-universal existence of the EPR effect, and different permeability of blood vessels in various tumors [28].

Active targeting, on the other hand, specifically targets cancer cells through direct interactions between ligands and receptors. The ligands on the surface of NPs are selected to target characteristic molecules on the surface of cancer cells, allowing them to distinguish targeted cells from healthy cells. As illustrated in Figure 2.1, active targeting exploits molecular recognition patterns through the ligands, allowing to enhance nanoparticle accumulation in tumor tissues, beyond that achieved by passive targeting alone. Minimizing presence of nanoparticles in normal tissue and thus, reducing side effects due to chemotherapy filtration. Active targeting is particularly suitable for the delivery of macromolecular drugs, as the interaction between ligands and receptors induces receptor-mediated endocytosis, allowing NPs to internalize in the cell and to successfully release therapeutic drugs [28]. Both passive and active processes are shown in Figure 2.1

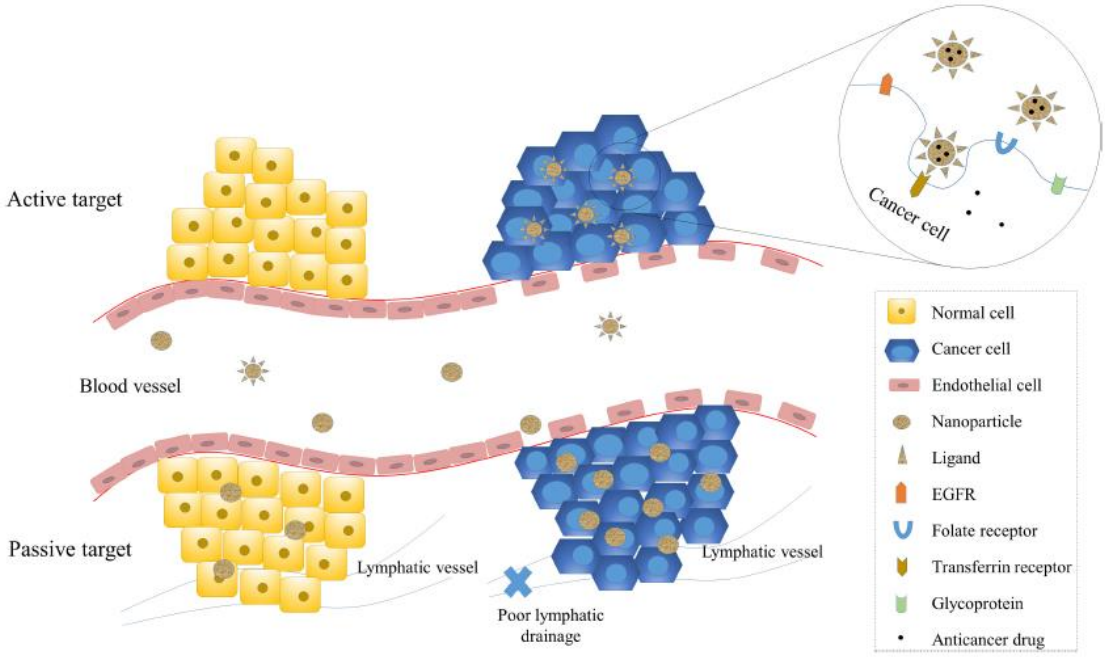

Figure 2.1. Passive and active targeting of NPs to cancer cells. Taken from [28].

During the development of the project, the analysis of a drug mass transfer process to cancerous tissue, by means of a constant flow with an initial constant concentration of drug solution in a channel containing an obstacle representative of a cancerous nodule, through models built with two values of fractal dimension, to represent different stages of development in the cancerous nodule, will be approached. The model consists of a channel with a square cross section and on one of its inner sphere faces are arranged in such a way that they form an assembly adhered to the wall, which is called a cluster. A constant flow of biological fluid is induced through the channel and the drug transfer process from biological flow to tissue is studied.

Chapter 3. Computational modeling of free-drug transport in a cancerous nodule within a microchannel.

The process in which a normal cell transforms into a cancerous cell is known as carcinogenesis; here the cell proliferates and reproduces at a much higher rate than normal, which induces the formation of abnormal growth of cells known as neoplasia or tumor. [3]

Objects that display a self-similar structure at different length scales are commonly referred to as fractals. A variety of systems in nature are fractals, including biological tissue samples for different body systems, like circulatory, respiratory, and nervous systems, among others. Biological tissues present spatial heterogeneity in the mass density distribution values and exhibit as a self-similar structure, which can be analyzed and described by fractal dimension [4]. This behavior has also been observed in tumors, and efforts have even been made to differentiate benign from malignant tumors according to the fractal dimension [31]. The fractal dimension of a tissue is known to change over the course of cancer progression, due to an increased production and rearrangement of intracellular structures, resulting in an increased mass density and rearrangement of the tissue; therefore a quantitative diagnostic test can be developed based on these modifications [4].

The fractal dimension is known as a real number that defines how completely a fractal can fill a defined space, generally composed of replicating elements on an increasingly smaller scale. Random fractals occur often in nature and can be found in the structures of trees, coastlines, corals, and in tissue structures [4, 32].

There are different methodologies for calculating the fractal dimension of an N-dimensional structure, resulting in values between 1 and 3 for a three-dimensional structure, where values close to 3 correspond to dense structures. The fractal dimension of an ideal smooth surface corresponds to 2, while the fractal dimension of a completely space-filling volume corresponds to 3. For example, a common fractal dimension value used to describe Earth's relief is 2.3 [33]. Two fractal dimension values of 2.3 and 2.7 were selected to represent distinct levels of structural complexity within the theoretical limits of 2 and 3.

The primary cluster models constructed with the particle position data [2] shown in Figure 3.1 are based in a Brownian dynamics simulation. Here, colloidal particles undergoing Brownian motion with a competing interaction pair potential, short range attraction and long-range repulsion. These are simulated at different concentrations and parameters of the potential, producing the formation of clusters with a given fractal dimension that depends on such parameters [34]. From the division of primary clusters, a total of 6 secondary clusters were obtained, one for each face of the cube that contained the initial cluster, which shares the same dimensional properties of the primary cluster, respecting the value of the corresponding fractal dimension.

The selected fractal dimensions are intended to represent two distinct morphologies of tissue through fractal dimension, which serves as a quantitative indication of structural complexity. The two selected values for fractal dimension 2.3 and 2.7, serve to evaluate whether changes in structural complexity influence drug transport. Even though evaluation of more fractal dimension values would prove useful in identifying behavior patterns of drug transport absorption, the two selected values provide a clear contrast in structural architecture. Additional fractal dimension values would likely exhibit an intermediate response rather than reveling additional transport mechanisms. Nevertheless, extending the analysis to cover a broader range of fractal dimensions represents an important direction of future work.

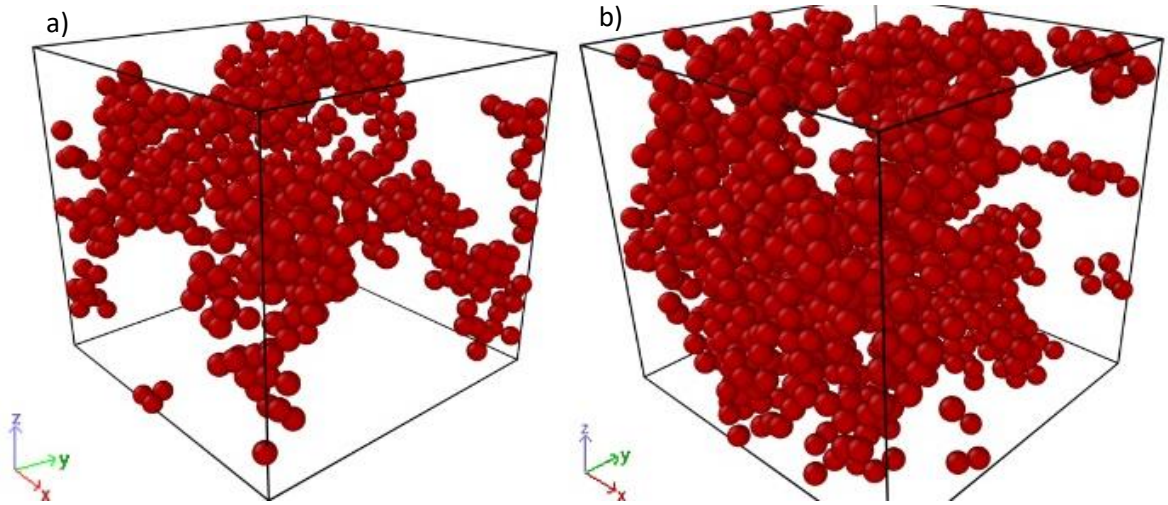

Figure 3.1. Main cluster of cancerous cells with a) fractal dimension 2.3 and b) fractal dimension 2.7. Taken from [2].

A study of the radius of gyration, $R_g(s)$, of finite clusters as a function of size (s), yielded that in all cases $R_g(s)$ follows the power law, therefore it is possible to calculate the slope of the power law in a log-log representation, $R_g(s) \sim s^{1/F_D}$ [34].

Although, the process may result in completely different cluster morphologies, the present analysis compares a single geometric configuration for each fractal dimension, rather than an ensemble of multiple configurations with varying geometries. Therefore, the observed tendencies of the study may be influenced by geometric differences associated with the specific configuration considered, rather than by the fractal dimension alone. Regardless, the results remain valuable, as they aim to provide initial insight into the influence of fractal structure on drug transport behavior and serve as a foundation for future studies that include a wider range of geometric configurations to better distinguish fractal effects from purely geometric variability.

3.1. Geometric parameters.

Cancerous nodules were modeled as clusters of cells arranged according to the level of the fractal structural obstacle. Based on [2], only cell cluster models emerging from the X-Y plane were considered for both fractal dimensions. A schematic representation of the geometric model of the cell is shown in Figure 3.2.

The geometric parameters of the model were defined as a function of the cell diameter, $d_{cell} = 50$ μm, and are summarized below:

- Channel width (X-direction): $w_{channel} = 20 * d_{cell} = 1000$ μm
- Channel length (Y-direction): $l_{channel} = 80 * d_{cell} = 4000$ μm
- Channel height (Z-direction): $h_{channel} = 20 * d_{cell} = 1000$ μm
- Wall thickness: $t_w = 10 * d_{cell} = 500$ μm

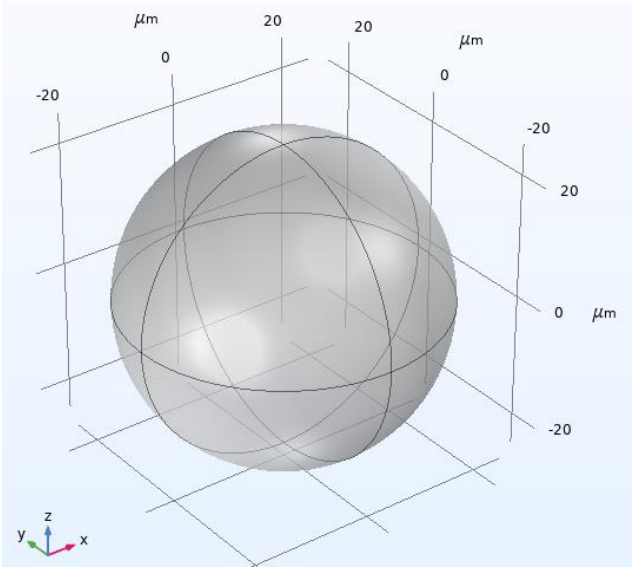

Figure 3.2. Representation of a cell from a cancerous nodule cluster using a solid sphere geometry.

From the subclusters models, four of the six positions were deemed suitable for this study. The X-Z plane nodules were not eligible for evaluation, as the area of origin is not in contact with any tissue domain, making it impossible to study the drug absorption phenomenon. Upon evaluation of the rest of the models, the X-Y plane nodules starting from Z=1000 µm were selected due to the significant number of cells and distribution in the microchannel. Figure 3.3 is a side view of the selected X-Y plane subcluster models, with 129 and 232 particles for 2.3 and 2.7 fractal dimensions, respectively.

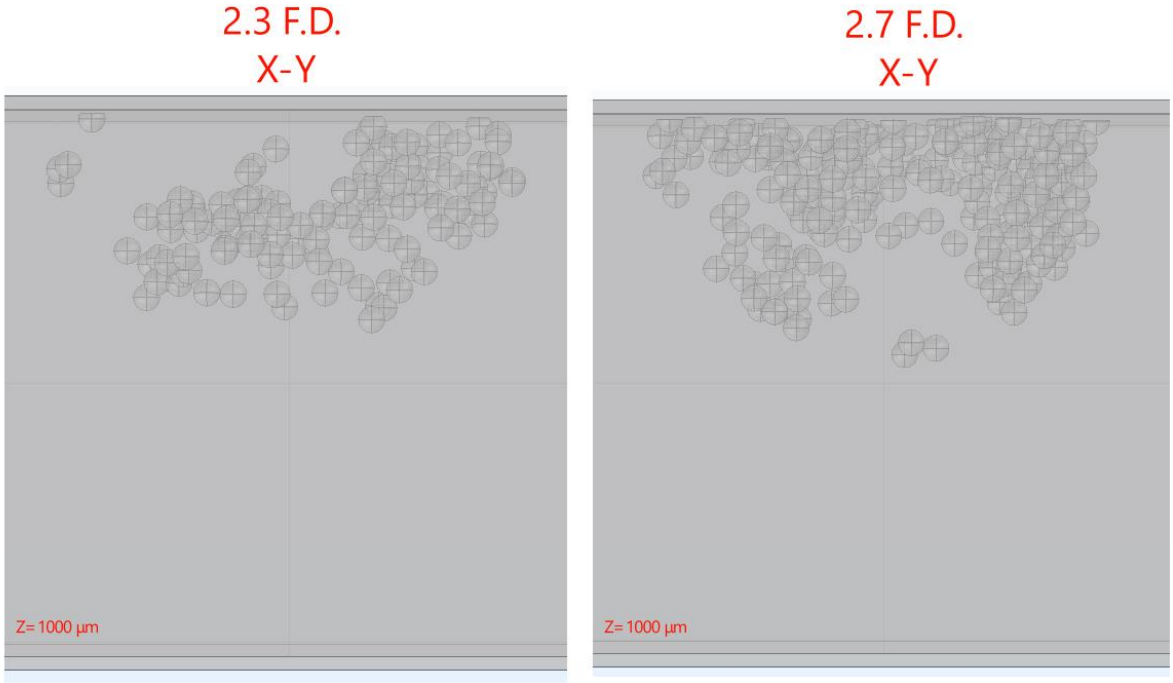

Figure 3.3. Side view of selected 2.3 (left) and 2.7 (right) fractal dimension subclusters. Taken from [2].

As in the original model used by J. A. Monasterio, 2023 [2] the domain is a 1 mm^2 squared-cross-section channel with a 4-mm length for fluid domain; this volume is to be considered as the analysis region for drug accumulation. A flow development zone was incorporated to allow the inlet flow to evolve into a fully developed profile before reaching the region of interest. Upon entering a channel, the velocity field requires a finite entry length to develop due to boundary layer formation at walls. When this effect is ignored, it may cause artificial velocity gradients to form and influence convective transport and distort the concentration distributions achieved at the analysis zone.

By considering a dedicated flow development region, the sudden imposed inlet conditions do not directly affect the distribution result within the region of interest, thus ensuring that the observed drug transport behavior is regulated by inherent model parameters rather than boundary-induced effects. This approach increases numerical stability and increases the physical accuracy of the simulated flow and mass transport phenomena.

The minimum required development length was estimated using a theoretical entrance-length expression for laminar flow, as shown in Equation 3.1:

$$\mathrm{L} = \frac{0.32a^2}{\eta} \cdot \mathrm{V_{prom}} + 1.4a \tag{3.1}$$

where a is the characteristic length of the domain, η is the dynamic viscosity of the fluid, and V_{prom} is the mean inlet velocity. This expression accounts for the balance between convective momentum transport and viscous diffusion during flow development [2,14].

The inlet velocity was varied between from 10 to 100 μm/s and the characteristic length was taken as the channel height, a = 1000 μm, corresponding to a squared-cross sectional domain [2]. The minimum required development length was calculated to range between 1403.19 to 1431.87 μm. A development region length of 2000 μm was selected to offer a conservative margin.

In the case of mass transfer, it is first necessary to identify whether the species transport is dominated by convection or diffusion, with the Péclet number defined in Equation 3.2

$$\mathrm{Pe} = \frac{\mathrm{U \cdot L}}{\mathrm{D}} \tag{3.2}$$

where U is the characteristic velocity of the fluid, L is the characteristic length of the channel and D is the molecular diffusion coefficient of the species in the fluid.

Considering the same range of channel velocities of the fluid for U, from 10 to 100 μm/s and a characteristic length L of 500 μm to characterize drug penetration into the tissue, the diffusion coefficient for paclitaxel in aqueous liquids of $D = 10^{-9}$ [38], the resulting values for the Péclet number ranged from 5 to 50 which indicate a mainly convection-driven mass transport regime; while diffusion remains non-negligible for low velocity regions, the overall spatial distribution of the transport species is mainly guided by the fluid velocity field.

Unlike the fluid velocity field, which required a finite entrance length to achieve a fully developed state, the species concentration is governed by a volumetric source term acting within the fluid domain over a certain drug infusion time and therefore does not reach a standard fully developed profile. Since the species transport is driven by a fully developed velocity field, only the combined effects of convection, diffusion and time-dependent species source will affect the drug concentration distribution, avoiding effects caused by the boundary conditions.

3.2 Numerical simulation

Drug concentration accumulation

The initial model, designated as convection-diffusion, assumes that the pharmaceutical agent is administered as a free drug in solution through the intraperitoneal route (IP), without accounting for any carrier-based or assisted drug delivery mechanisms.

Convection-diffusion

A subsequent mesh independence analysis was conducted under these assumptions. Simulations were performed using COMSOL Multiphysics® [35] employing two physics interfaces: Free and Porous Media Flow and Transport of Diluted Species in Porous Media, available through a project collaborator.

The fluid flow was modeled using the Free and Porous Media Flow module in COMSOL Multiphysics® [35], which was implemented to solve the incompressible flow Navier-Stokes equations within a three-dimensional domain under stationary conditions. The momentum conservation is given by Equation 3.3, while mass conservation for incompressible flow is given by the continuity equation, Equation 3.4.

$$\rho(u_f \cdot \nabla)u_f = \nabla \cdot [-pI + \tau] + F \tag{3.3}$$

$$\nabla \cdot u_f = 0 \tag{3.4}$$

where ρ is the fluid density, u_f is the fluid velocity vector, p is the pressure, I is the identity tensor, τ is the viscous stress tensor, and F represents the body forces.

Subsequently, the Transport of Diluted Species in Porous Media interface, considers convection and molecular diffusion in a saturated porous medium under time-dependent conditions in a three-dimensional domain; the transient mass balance involving convection and diffusion is described by Equation 3.5, while molecular diffusion is represented by Fick's Second Law in Equation 3.6.

$$\frac{\partial(\epsilon_p c_i)}{\partial t} + \frac{\partial(\rho c_{p,j})}{\partial t} + \nabla \cdot J_i + u_m \cdot \nabla c_i = R_i + S_i \tag{3.5}$$

$$J_i = -D\,\nabla c_i \tag{3.6}$$

where c_i and $c_{p,j}$ represent the liquid and solid phase concentrations, J_i is the mass diffusive flux vector, u_m is the mass average velocity, R_i is the expression of the reaction rate for the species and S_i is an arbitrary source term, D is the liquid diffusion coefficient.

Equation 3.5 includes a solid-phase accumulation term in the general formulation. However, for free-drug IP delivery without a carrier, solid phase accumulation and adsorption effects were neglected. Therefore, species transport was assumed to occur exclusively in the fluid phase of the porous medium, $c_{p,j} = 0$. Since paclitaxel was treated as a non-reactive species, the reaction rate term, R_i, was also neglected.

3.3 Numerical parameters of the model

3.3.1 Materials

Three different materials are assigned to the geometries of the model. The properties of two different types of tissue and those of interstitial fluid were defined, as noted in Table 3.1.

Table 3.1. Numerical parameters of the materials.

Variable	Parameter	Numerical Value for			Reference
		Cancerous Tissue	Healthy Tissue	Interstitial Fluid	
ρ	Density [kg/m^3]	1100	1100	998.2054	[2]
ν	Dynamic viscosity [Pa·s]	0.5	0.5	0.001009	[2]
E	Young's modulus [Pa]	500	500	-	[36]
ν	Poisson ratio	0.35	0.35	-	[37]
κ	Permeability [m^2]	2.4×10^{-11}	10^{-11}	0.4	[37]
ε	Porosity	0.85	0.7	-	[13]
D	Diffusion coefficient [m^2/s]	1.3×10^{-12} [36]	0.048×10^{-12} [36]	10^{-9} [38]	[36,38]
s	Saturation	0.55	0.3	-	[37]

Permeability is a parameter of particular physical importance when modeling the flow within tumor tissue. For permeability values below $\kappa < 10^{-12}$ m^2, the tumor behaves effectively as a solid in contact with an external flow, and the governing porous-media equations may no longer provide an appropriate physical description. Consequently, a larger κ-value must be employed to ensure the numerical solution is well posed. In this study, the mean value reported by L. T. Baxter [37], $\kappa = 2.4\times10^{-11}$ m^2, is adopted; additionally, a comparable value, $\kappa = 10^{-11}$ m^2, is proposed for non-tumor tissue.

The materials described in Table 3.1 are assigned to the microchannel model, as shown in Figure 3.4. The blue domain represents the cancerous nodule, involving both the cancer cells and the proximate affected tissue, which was defined as the "Cancerous Tissue" material. The gray region corresponds to the tissue portion that has not yet been affected by the disease, which was defined as "Healthy Tissue". The red region denotes the interstitial fluid domain, for which the parameters can be considered similar to those of water. Each material was characterized by its respective thermophysical properties, including density and dynamic viscosity. This configuration reflects the physical configuration of a space in the abdominal cavity, filled with interstitial fluid acting as a lubricant between the organs and muscle tissue.

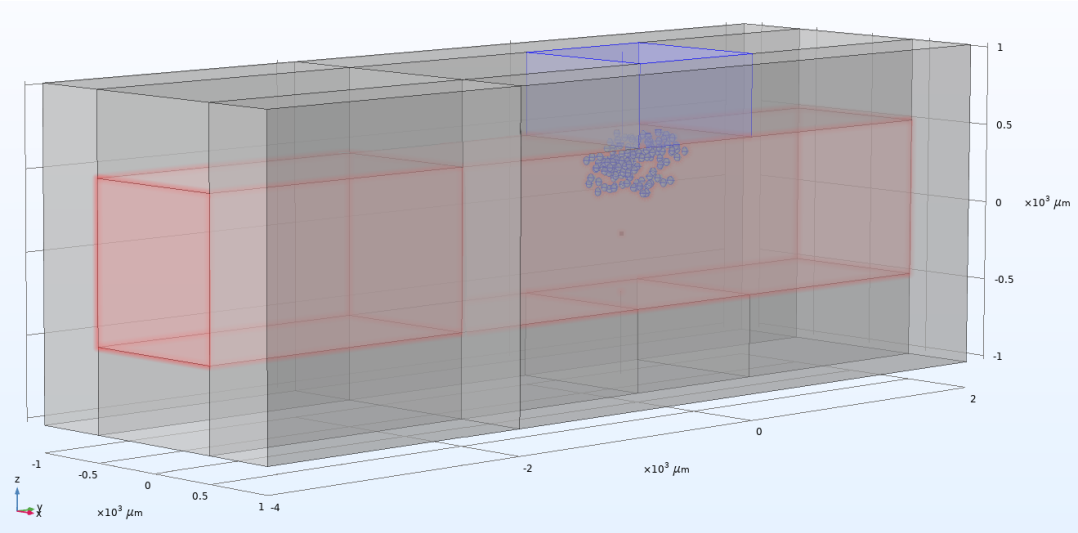

Figure 3.4. Assignment of materials to the domains of the microchannel geometry with the presence of a cluster with fractal dimension 2.3.

3.3.2 Boundary conditions

Free and Porous Media Flow

For the convection-diffusion model, several assumptions were made to correctly simulate flow behavior in the peritoneal cavity. As mentioned before, a laminar flow regime tends to prevail in biological systems [7]. A constant inlet velocity of 30 µm/s was assigned at the channel entrance, aligned with the low interstitial flow velocities characteristic of biological microenvironments [2,5,7,9,15]. These assumptions minimize inertial forces due to the low Reynolds number regime of interstitial flow while ensuring a steady convective transport field in which viscous forces dominate fluid motion.

At the channel outlet, a reference pressure of P_o = 0 Pa was assigned, allowing the fluid velocity field to develop naturally according to the imposed velocity inlet and internal geometric resistance of the domain. This condition allows to represent a downstream region with negligible pressure constraints, commonly employed to simulate open biological systems [2,5,9].

The external boundaries of the microchannel were assigned with a no-slip condition, imposing a zero bulk velocity (u=0) for fluid in the distal end of tissue domains, preventing tangential fluid motion at the tissue boundaries. The healthy and cancerous tissue domains were considered as porous domains, where fluid transport was described by the volume-averaged Navier Stokes equations incorporating the effects of porous matrix through porosity and permeability of the tissue.

Initial model conditions were specified as zero velocity and zero pressure throughout the fluid domain (u = 0 µm/s, p_o= 0 Pa), representing a stationary fluid state prior to the inception of flow. These initial conditions have no effect on the steady state solution but are considered to ensure numerical stability during the startup period of the model. The fluid flow boundary conditions are shown in Figure 3.5.

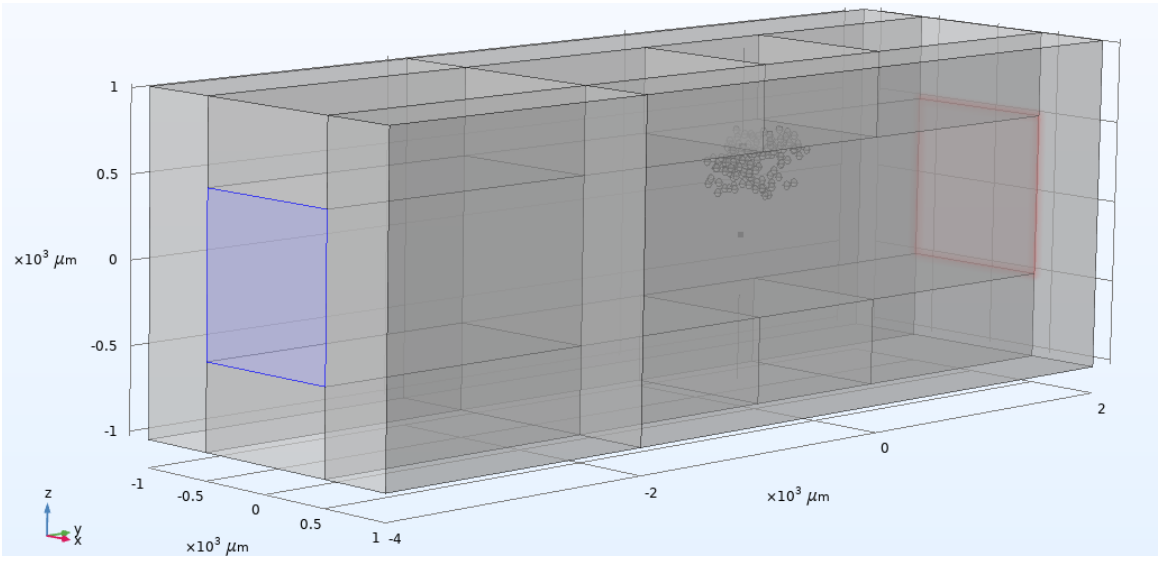

Figure 3.5. Fluid flow boundary conditions. Fluid flow velocity input u_i=30 µm/s (blue) and pressure outlet p_o=0 Pa (red). Initial conditions are applied on all system domains.

Transport of Diluted Species in Porous Media.

Boundary conditions were defined to represent localized drug release and physiological clearance mechanisms. The cancerous and healthy tissue domains were defined as partially saturated porous media. Its properties where assigned according to Table 3.1. Species transport within these domains is described by the convection-diffusion equation for porous media, accounting for convective transport represented by fluid velocity field (u). Additionally, diffusive flux is governed by Fick's second law using the species diffusion coefficient in the solute (D) with the Millington and Quirk model selected as effective diffusivity model.

Drug intraperitoneal administration was modeled as a spatially homogeneous volumetric source acting within the interstitial fluid domain, implemented via a time-dependent step function as shown in Figure 3.6a. A 100 mg dose level of paclitaxel (PTX) was selected to match the lower clinical limit in the treatment of advanced ovarian carcinoma, diluted in 1 L of solution (L_{sol}) prior to IP administration [23,24]. Calculating the dose of paclitaxel in grams (g_{PTX}) by the volume of solution results in 0.1 g_{PTX}/L_{sol} or 100 g_{PTX}/m^3_{sol}.

Considering a molecular weight (MW) of 853.9 g/mol for paclitaxel and an infusion time of 10800 s [24], the species production rate is to be calculated as shown in Equation 3.7.

$$S_{PTX} = \frac{\text{Dose}_{PTX/L,sol}}{MW \cdot t_{inf}} \tag{3.7}$$

The volumetric species production term results in a value of $1.08435\times10^{-5}\cdot$step1(t) $mol_{PTX}/m^3_{sol} \cdot s$. The time-dependent step function controls the species production rate and limits the species release. For t <10800 s, the value for the step function is defined as step1(t) ≈ 1. Once the infusion time is reached (t >10800 s), the step function is set to step1(t) ≈ 0. A transition zone of 100 s was introduced to allow a smooth shift of the system from 1 to 0.

An outflow condition was assigned at the channel outlet and along the channel sidewalls, allowing the species to exit the space governed by the local velocity field without imposing concentration

gradients, as illustrated in Figure 3.6b. This condition ensures that the species removal mechanism is driven by convection and diffusion rather than boundary constraints.

At the distal end of the healthy tissue domains, Dirichlet condition for fixed concentration value $c_i = 0\,mol/m^3$ was prescribed, as shown in Figure 3.6c. This boundary condition helps represent an effective sink due to systemic clearance present in the healthy tissue domains due to lymphatic drainage capacity. Numerically a realistic gradient is maintained and prevents species backflow into the domain throughout the simulation. Additionally, Neumann condition for concentration flux $J_i=0$ was considered on the boundaries coloured in gray in Figure 3.6.

Initial model conditions were specified as zero concentration throughout fluid and tissue domains ($c = 0\ mol/m^3$), representing a stationary fluid state prior to the inception of flow.

3.4 Probe positioning

A configuration of four domain point probes are positioned along the line containing the highest cell density in order to maximize convective and diffusive interactions and to most accurately represent drug accumulation. These probes are set to evaluate the temporal development of species concentration and provide essential information on drug absorption pathway. The spatial coordinates of the four-point probes are specified in Table 3.2. An image of their location is provided in Figures 3.7 and 3.8.

Additionally, two domain probes are placed in both the cancerous and healthy tissue domains. The probes measure the volume-average drug concentration by integrating the spatial concentration distribution over each respective domain. These probes aim to evaluate the temporal development of the integrated drug concentration within each tissue domain.

Table 3.2. Concentration point probes location for 2.3 and 2.7 fractal dimension cluster models.

Fractal Dimension	Probe	X-coordinate (μm)	Y-coordinate (μm)	Z-coordinate (μm)
2.3	1	-150	0	600
2.3	2	-150	0	625
2.3	3	-150	0	650
2.3	4	-150	0	700
2.7	1	-30	245	600
2.7	2	-30	245	625
2.7	3	-30	245	650
2.7	4	-30	245	700

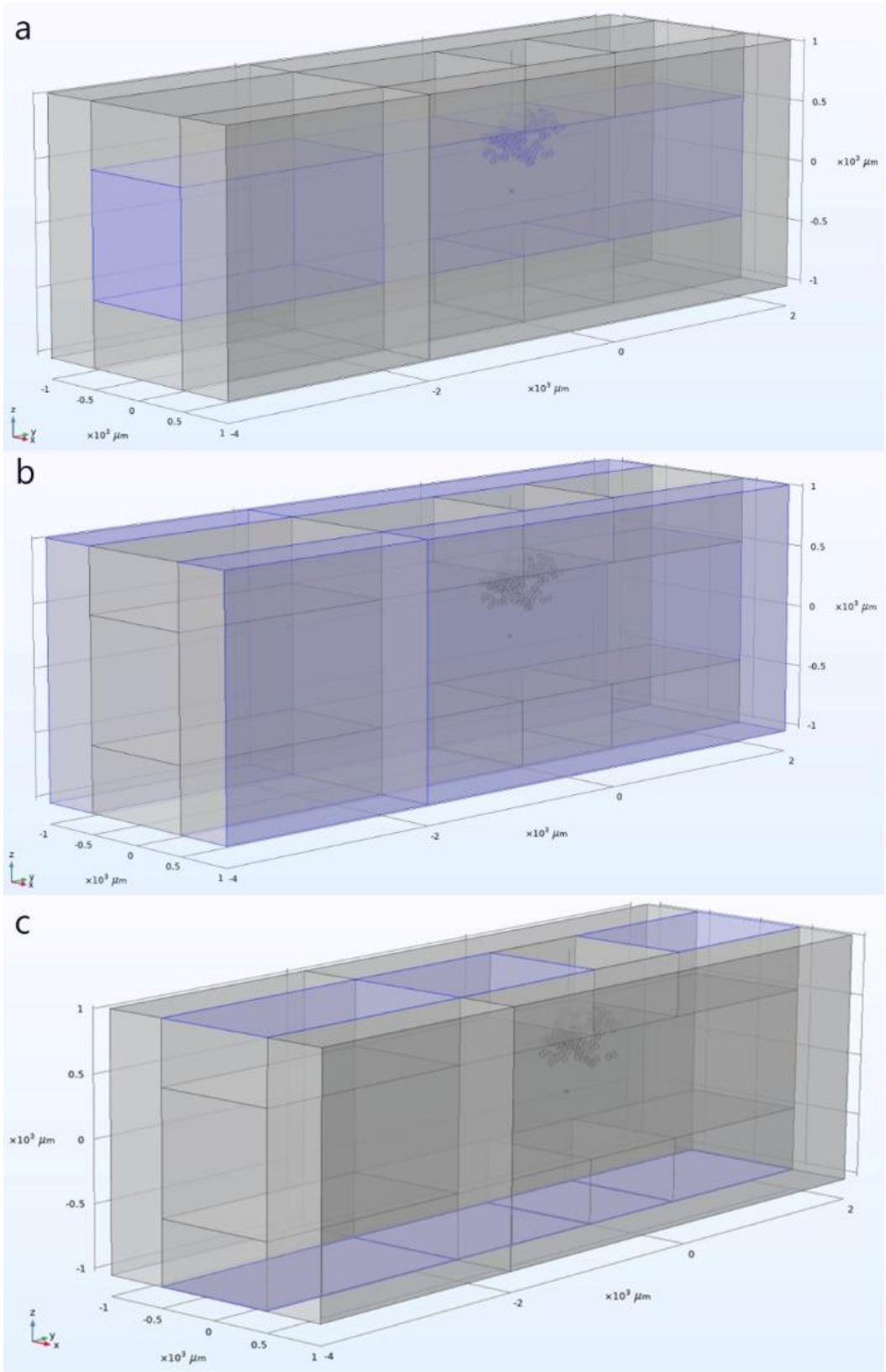

Figure 3.6. Species transport boundary conditions.(a) Volumetric species source $S_{PTX}=1.08435\times10^{-5}$ ·step1(t) mol/m^3.(b) Species outflow.(c) Zero species concentration condition $c_i=0\,\mathrm{mol/m^3}$.

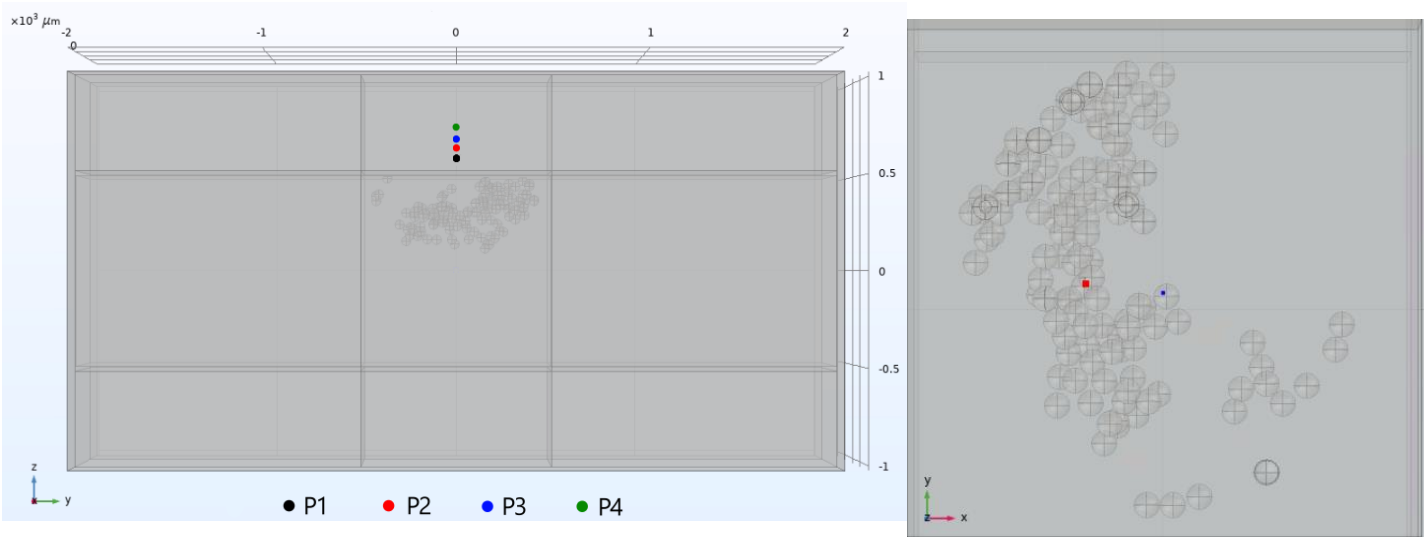

Figure 3.7. Domain point probe location in a microchannel with presence of cluster with a fractal dimension of 2.3. Views in the *y*-*z* plane (left), and the *x*-*y* plane (right) are shown.

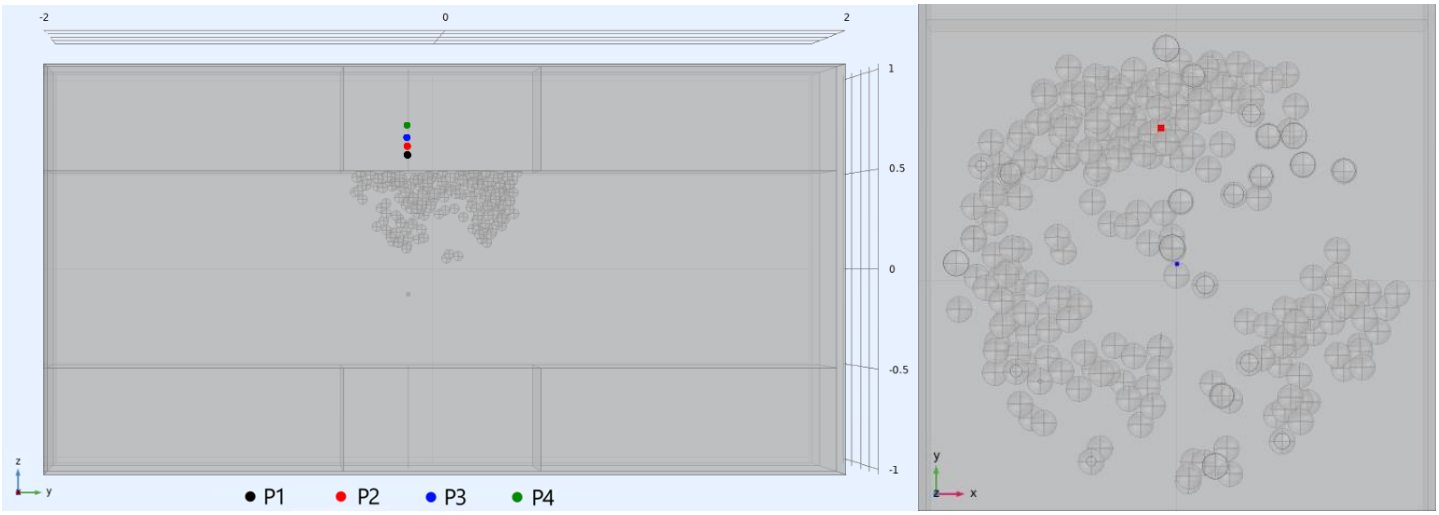

Figure 3.8. Domain point probe location in a microchannel with presence of cluster with a fractal dimension of 2.7. Views in the *y*-*z* plane (left), and the *x*-*y* plane (right) are shown.

3.5. Mesh generation

Before the execution of the numerical simulations, a mesh independence study was conducted to ensure solution convergence and numerical validity. In this study, mesh size directly affects numerical accuracy. Therefore, it is necessary to perform multiple refinements until a selected relevant parameter does not present significant variations.

As the mesh independence study performed by Monasterio [2] takes into account the maximum deflection as a significant evaluation parameter, the study will not be applicable to this iteration, as the cells are set as a rigid domain.

In the first study, the Free and Porous Media Flow and the Transport of Diluted Species in Porous Media interfaces were evaluated for the first stage of the mesh independence analysis. A “Finer”

element size was selected for the tissue domains to remain stable during the first stage, with the mesh parameters shown in Table 3.3. Meanwhile, the element size of the fluid domain was refined iteratively according to the values listed in Table 3.4, while monitoring the maximum velocity within a 20-µm-wide region defined between x = -160 µm and x = -140 µm. This region corresponds to a section of the model with high cell density, where stronger velocity gradients are expected. The mesh was created with free tetrahedral elements and the discretization setting in both interfaces was selected as Linear P1. The mesh element breakdown for the fluid domain iteration analysis is shown in Table 3.5. Total simulation time data for the studies is also provided.

Table 3.3. Mesh size characteristics for tissue domains.

Mesh	Size	Max. Element Size (µm)	Min. Element Size (µm)	Max. Elem. Growth Rate	Curvature Factor	Narrow Region Resolution
T	Finer	100	12.5	1.35	0.3	0.85

Table 3.4. Mesh size iteration for fluid domain analysis.

Mesh cases	Size	Max. Element Size (µm)	Min. Element Size (µm)	Max. Elem. Growth Rate	Curvature Factor	Narrow Region Resolution
1	Fine	150	12.5	1.13	0.5	0.8
2	Fine	120	12.5	1.13	0.5	0.8
3	Fine	90	12.5	1.13	0.5	0.8
4	Fine	70	12.5	1.13	0.5	0.8
5	Fine	60	12.5	1.13	0.5	0.8
6	Fine	50	12.5	1.13	0.5	0.8

Table 3.5. Number of elements and simulation time of mesh size iteration for fluid domain analysis.

Mesh cases	Fluid domain			Fluid and Tissue domains			Total simulation time for	
	Domain Elements	Boundary Elements	Edge Elements	Domain Elements	Boundary Elements	Edge Elements	Hydro dynamics	Species Transport
1	654,115	28,606	5,034	1,053,098	47,690	5,993	3 m 30 s	3 h 41 m 36 s
2	672,688	29,820	5,083	1,077,291	48,469	6,042	4 m 26 s	3 h 31 m 51 s
3	729,858	32,482	5,165	1,142,844	51,799	6,124	4 m 38 s	3 h 4 m 8 s
4	861,860	37,398	5,291	1,299,783	57,655	6,250	4 m 49 s	3 h 8 m 8 s
5	1,012,236	41,618	5,370	1,480,001	62,472	6,329	5 m 18 s	3 h 24 m 3 s
6	1,321,683	48,222	5,486	1,839,795	69,744	6,445	6 m 55 s	3 h 33 m 49 s

The refinement process continued until no significant change was detected between sequential cases, as shown in Table 3.6 and Table 3.7.

Table 3.6. Maximum velocity for every iteration of fluid mesh size.

Mesh cases	Number of fluid domain elements	Total number of domain elements	Maximum velocity in monitored region [μm/s]	Relative difference (%)
1	654,115	1,053,098	67.9194	-
2	672,688	1,077,291	70.5716	3.7582
3	729,858	1,142,844	71.0306	0.6462
4	861,860	1,299,783	70.7724	0.3649
5	1,012,236	1,480,001	70.9549	0.2572
6	1,321,683	1,839,795	70.9149	0.0564

Table 3.7. Concentration at probe for every iteration of fluid mesh size.

Mesh cases	Number of fluid domain elements	Total number of domain elements	Concentration at probe (-150, 0, 600), t=24 h [mol/m^3]	Relative difference (%)
1	654,115	1,053,098	0.02481	-
2	672,688	1,077,291	0.02790	11.0685
3	729,858	1,142,844	0.03474	19.6922
4	861,860	1,299,783	0.04415	21.3103
5	1,012,236	1,480,001	0.04500	1.8848
6	1,321,683	1,839,795	0.05132	12.3216

The mesh independence study for the hydrodynamics study is summarized in Table 3.6. A progressive refinement of the mesh shows that the maximum velocity converges between meshes 4, 5 and 6, with percentage differences of 0.3649%, 0.2572%, and 0.0564%, respectively. This trend indicates that the solution approaches an asymptotic regime, with a decreasing variation as the mesh is further refined.

For the species transport study, Table 3.7 presents the corresponding analysis of the concentration value at the probe located in (-150, 0, 600) at t = 24 h. Unlike the velocity results, the concentration values present larger fluctuations across refinement iteration, particularly between meshes 2 and 4. However, a significant reduction in variation is observed between meshes 4 and 5 (1.8848%), which may suggest the beginning of convergence. The increased discrepancy observed for mesh 6 is attributed to the convective transport predominant nature of the species transport problem. Given the high local Péclet numbers that appear in the analysis, pronounced concentration gradients and thin boundary layers develop, making the numerical solution particularly sensitive to mesh resolution. Therefore, a uniform mesh refinement may probe insufficient to fully resolve these localized features, and additional local domain refinement is needed to approach full mesh independence.

Taking into consideration both flow and species transport results, mesh 5 was selected as a reasonable balance between accuracy and computational cost, since it provides adequately convergent velocity results while achieving the lowest variation in concentration among the refined meshes.

For the second stage of the mesh independence study, the element size selected for the fluid domains in the first stage was kept fixed. The mesh refinement was applied for the tissue domain, with the corresponding element size configurations shown in Table 3.8. The mesh element breakdown for the fluid domain iteration analysis is shown in Table 3.9. Compute time data associated with each case of the studies is reported.

Table 3.8. Mesh size iteration for tissue domain analysis.

Mesh cases	Size	Max. Element Size (µm)	Min. Element Size (µm)	Max. Elem. Growth Rate	Curvature Factor	Narrow Region Resolution
1	Finer	200	12.5	1.35	0.3	0.85
2	Finer	160	12.5	1.35	0.3	0.85
3	Finer	120	12.5	1.35	0.3	0.85
4	Finer	80	12.5	1.35	0.3	0.85
5	Finer	60	12.5	1.35	0.3	0.85
6	Finer	60	12.5	1.35	0.3	0.85

Table 3.9. Number of elements and simulation time of mesh size iteration for tissue domain analysis.

Mesh cases	Fluid domain			Fluid and Tissue domains			Total simulation time for	
	Domain Elements	Boundary Elements	Edge Elements	Domain Elements	Boundary Elements	Edge Elements	Hydro dynamics	Species Transport
1	1,012,236	41,618	5,370	1,287,011	50,138	5,923	4 m 37 s	2 h 34 m 40 s
2	1,012,236	41,618	5,370	1,304,303	52,582	6,039	5 m 27 s	3 h 3 m 10 s
3	1,012,236	41,618	5,370	1,375,578	57,236	6,197	5 m 17 s	3 h 13 m 11 s
4	1,012,236	41,618	5,370	1,480,001	62,472	6,329	5 m 13 s	3 h 22 m 47 s
5	1,012,236	41,618	5,370	1,743,460	72,446	6,557	6 m 38 s	4 h 53 m 32 s
6	1,012,236	41,618	5,370	2,548,424	91,488	6,913	9 m 45 s	10 h 14 m 16 s

The refinement process continued until no significant change was detected between sequential cases, as shown in Table 3.10 and Table 3.11.

Table 3.10. Maximum velocity for every iteration of tissue mesh size.

Mesh	Number of fluid domain elements	Total number of domain elements	Maximum velocity in monitored region [µm/s]	Relative difference (%)
1	1,012,236	1,287,011	70.8914	-
2	1,012,236	1,304,303	70.7684	0.1739
3	1,012,236	1,375,578	71.0588	0.4088
4	1,012,236	1,480,001	70.9549	0.1465

5	1,012,236	1,743,460	70.8971	0.0816
6	1,012,236	2,548,424	70.6466	0.3546

Table 3.11. Concentration at probe for every iteration of tissue mesh size.

Mesh	Total number of fluid elements	Total number of domain elements	Concentration at probe (-150, 0, 600), t=24 h [mol/m^3]	Relative difference (%)
1	654,115	1,053,098	0.03712	-
2	672,688	1,077,291	0.03868	4.0269
3	729,858	1,142,844	0.04256	9.1155
4	861,860	1,299,783	0.04500	5.4153
5	1,012,236	1,480,001	0.04806	6.3678
6	1,321,683	1,839,795	0.04978	3.4552

The second iteration of mesh independence study, focused on tissue domain refinement, is summarized in Table 3.10 and Table 3.11. For the hydrodynamic study, the maximum velocity evaluated within the monitored region shows limited variation across mesh refinement iterations, as percentage differences remain below 0.41% in all cases. The smallest percentage difference is observed between meshes 4 and 5 (0.0816%). This behavior indicates that the velocity field solution is insensitive to further refinement, therefore it can be concluded that the solution has reached a stable regime.

For the species transport study, Table 3.11 presents the concentration values evaluated at the probe location (-150, 0, 600) at t = 24 h. In contrast with the first stage analysis, the results display variation across mesh refinements with percentage differences falling below 10%. While a convergence behavior is not quite observed, the results indicated a gradual decrease towards higher elements meshes. A significant reduction in the relative difference is observed between meshes 5 and 6 (3.4552%), which suggests improved stability, and indicating that the solution is approaching convergence with further mesh refinement. On the down side, computational time spikes in this last iteration. Despite the reduced relative difference, the absence of monotonic convergence indicates that the asymptotic mesh-independent regime has not yet been reached. Consequently, the results must be interpreted with this limitation in mind. Further localized adaptive mesh refinement in regions with high Péclet numbers is recommended in future work to improve solution convergence.

Considering both flow and species transport results and limitations from the current computational equipment, mesh 5 was selected as the appropriate configuration for the model. This mesh provides stable hydrodynamic results while maintaining an acceptable variation for the concentration field, offering a balance between numerical accuracy and computational efficiency for subsequent simulations.

Figure 3.9 plots the concentration values for the fluid and tissue domain mesh refinements shown in Tables 3.7 and 3.11. An increase in the number of elements is directly associated with higher concentration values in the fluid-domain iteration stage and a reduced gradient between consecutive meshes. In contrast, once Mesh 5 for fluid domains is selected, the concentration gradient across the iterations for tissue-domain is reduced substantially, especially between meshes 5 and 6.

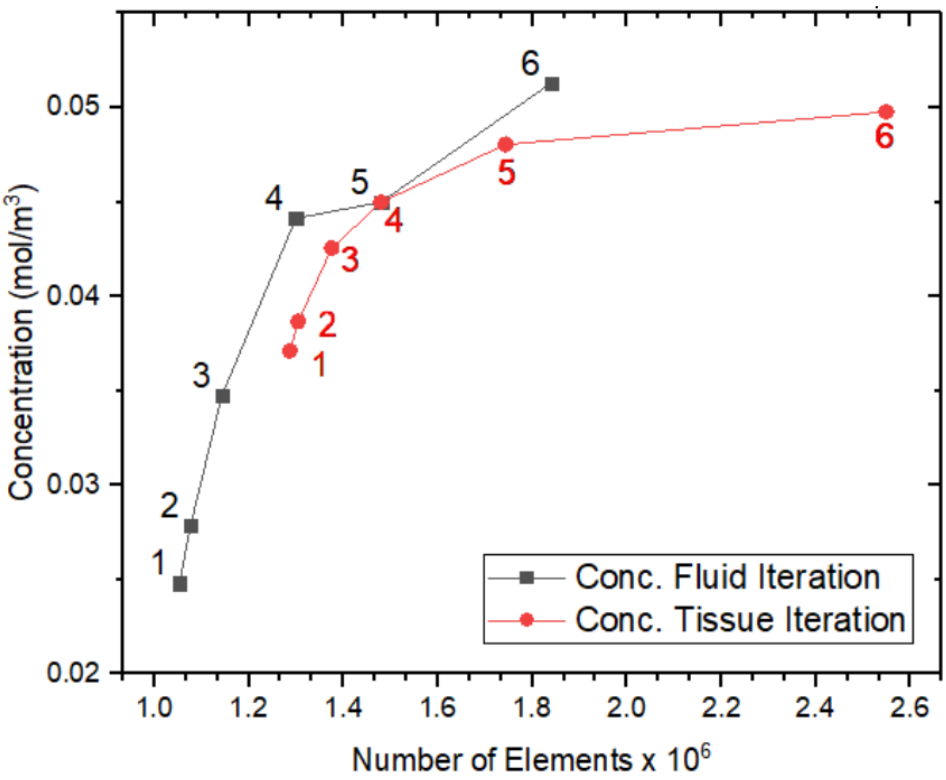

Figure 3.9. Comparison of concentration for fluid and tissue domain meshing iterations in probe location (-150, 0, 600) at t = 24 h.

3.6 Computational model parameters

Two initial mesh independence studies were conducted. The first study was designed to assess the hydrodynamic aspect of the model, incorporating a stationary step. The second study was designed to calculate species transport, incorporating a time-dependent step. After these analysis, geometric points and lines were added to the model to help with further refinement of the mesh, helping the model match the location of the probes with mesh nodes, to avoid result variation.

The final parameters defined for the mesh, as compiled in Table 3.12, were established in accordance with the findings of the mesh independence study, with the value of relative tolerance in the studies set as 0.0001. Both study solvers utilize a 'Segregated' attribute node, to allow the model to handle the solution process in substeps, to aid with computational requirements. In the case of the Stationary study, a lineal iterative solver is employed, using the 'AMG, fluid flow variables' with the Generalized Minimum Residual (GMRES) iterative method and the Multifrontal Massively Parallel Sparse Direct Solver (MUMPS) solver. On the other hand, the Time-Dependent study relies on a direct solver, making use only of the MUMPS solver.

Figure 3.10 plots the results for the stationary hydrodynamic study for the microchannel with a 2.3 fractal dimension cluster. After a development length region, the fluid velocity profile remains stable until the involvement of the cluster of cancerous nodules near the mark y=-500 µm.

Figures 3.11 and 3.12, show results for the Species Transport study for the microchannel with a 2.3 fractal dimension cluster with the initial parameters assigned. After the development of the flow region, it can be seen that the drug absorption occurs predominantly in the cancerous tissue domain.

The occurrence of this behavior can be attributed to a combination of different factors, such as the difference in tissue porosity and velocity at nearby boundaries, among others.

Table 3.12. Element size parameters for the mesh.

Element Domain	Fluid	Tissue
Mesh size	Fine	Finer
Calibration	Fluid dynamics	General physics
Maximum element size	60 µm	80 µm
Minimum element size	12.5 µm	12.5 µm
Maximum growth rate	1.13	1.35
Curvature factor	0.5	0.3
Narrow region resolution	0.8	0.85

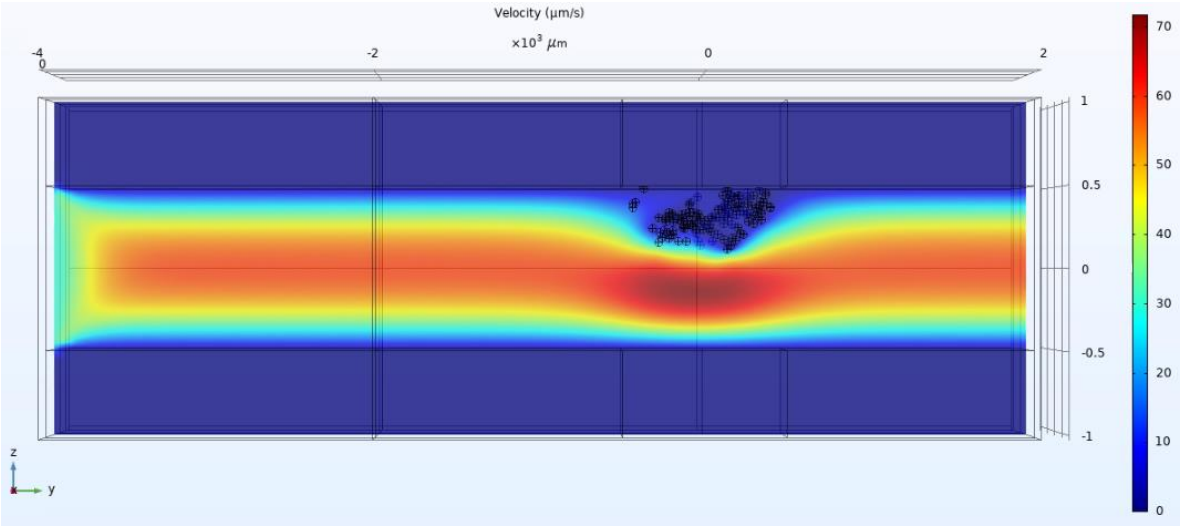

Figure 3.10. Side view of the velocity distribution in a microchannel containing a cluster with a fractal dimension 2.3. A cross-section of the model with a *y-z* plane at x=-150 µm at t=24 h was used.

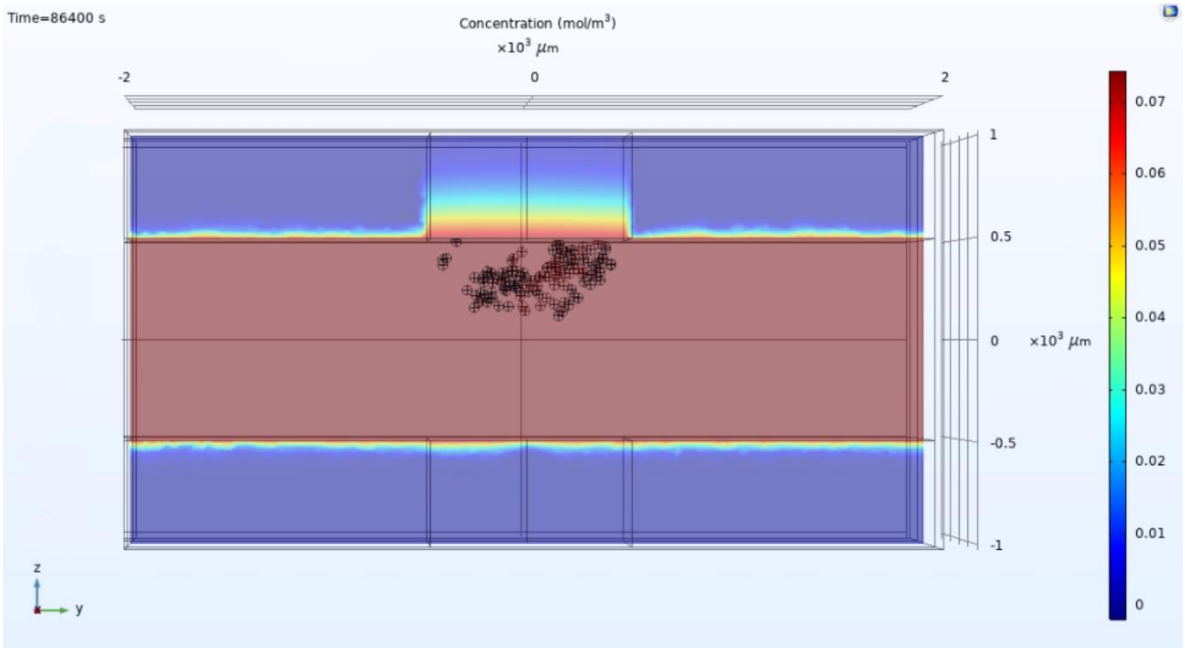

Figure 3.11. Concentration distribution in the plane at x=-150 µm at 24 h in microchannel with the presence of a cluster of fractal dimension 2.3.

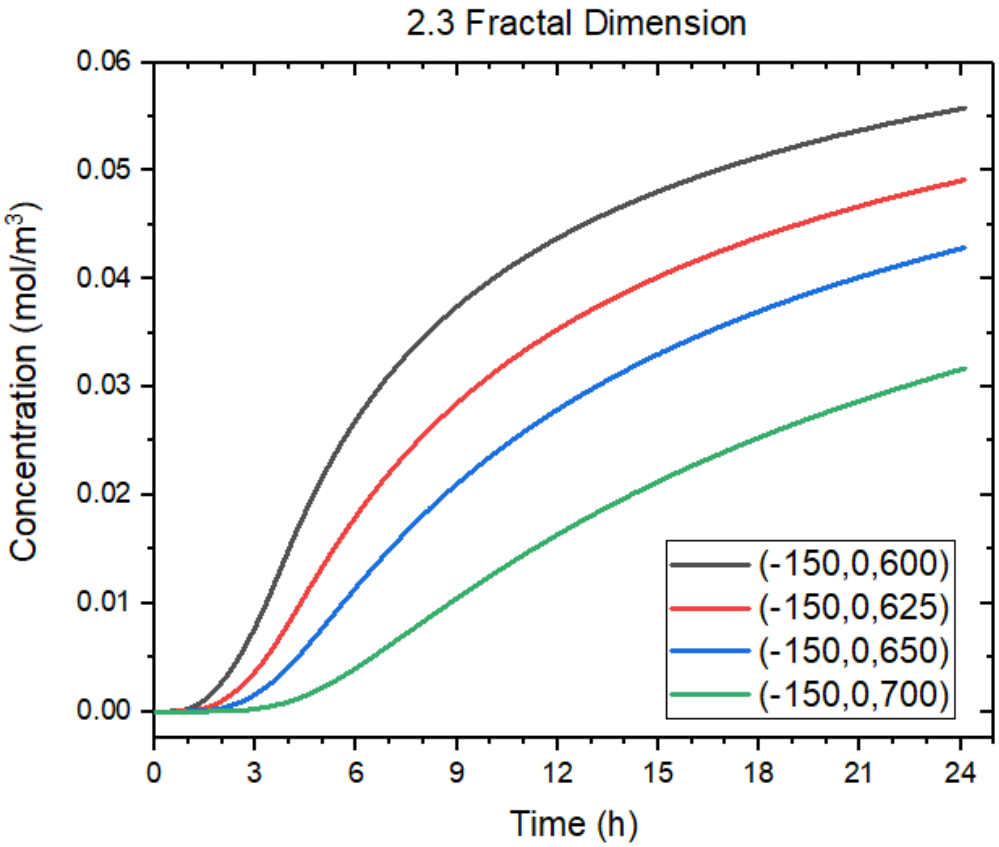

Figure 3.12. Temporal variation of species concentration measured at four selected locations within a microchannel containing a cluster of fractal dimension 2.3.

Figure 3.13 plots the results for the stationary hydrodynamic study now for the microchannel with a 2.7 fractal dimension cluster. The same behavior from the 2.3 F.D model replicates; however, the change due to involvement of the cancerous nodule cluster near the y=-500 µm mark is much more pronounced.

Figures 3.14 and 3.15, show results for the Species Transport study for the microchannel with a 2.7 fractal dimension cluster with the initial parameters assigned. Drug absorption behavior also occurs predominantly in the cancerous tissue domain, with a barely noticeable difference at this stage of the study.

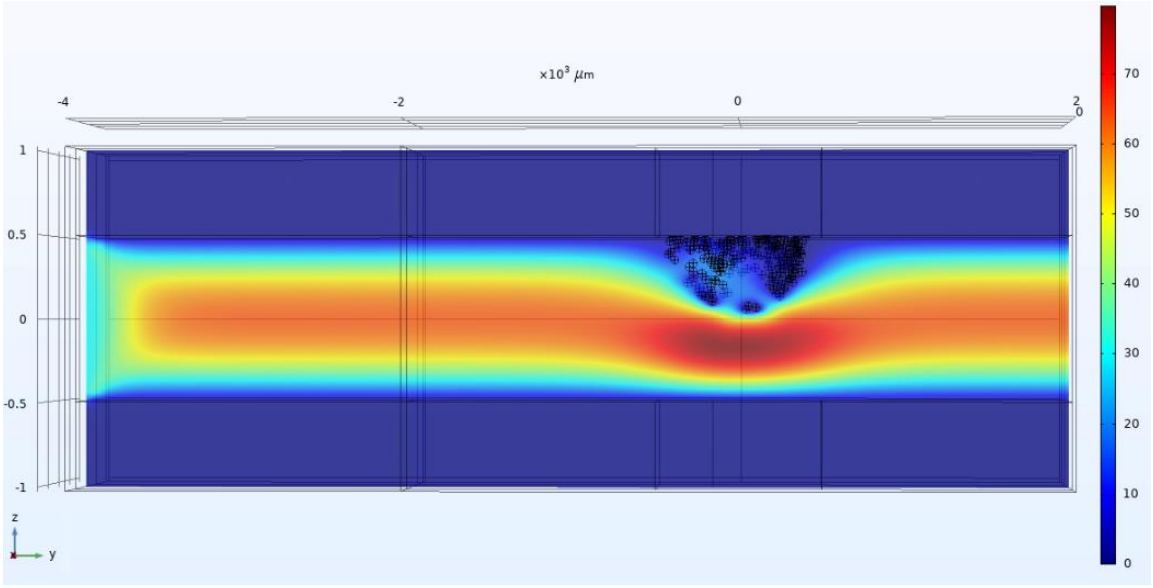

Figure 3.13. Side view of the velocity distribution in a microchannel containing a cluster with a fractal dimension 2.7. A cross-section of the model with a *y-z* plane at x=-30 µm at t=24 h was used.

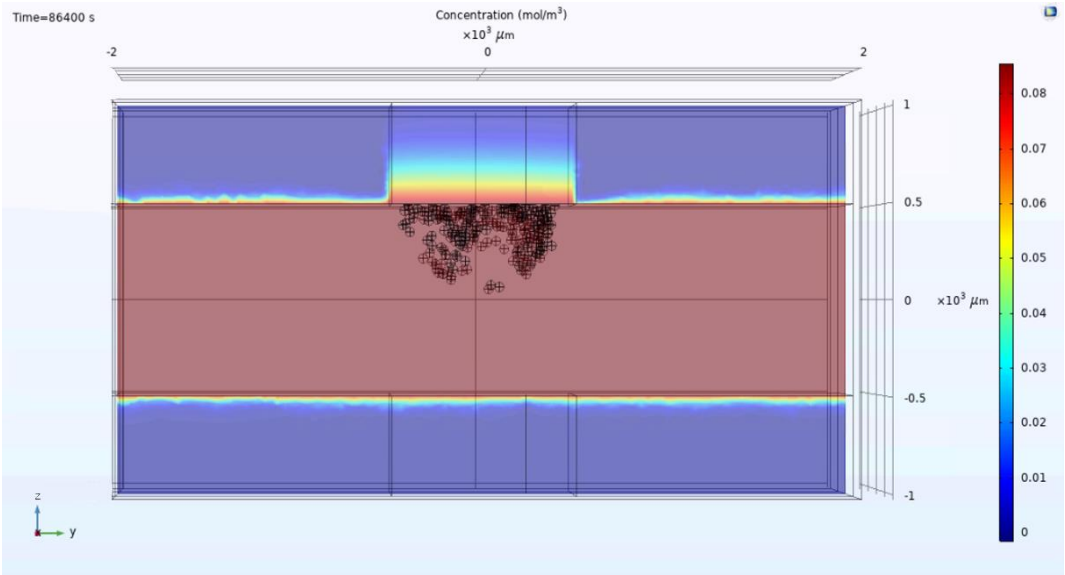

Figure 3.14. Concentration distribution in the plane at x=-30 µm at 24 h in microchannel with the presence of a cluster of fractal dimension 2.7.

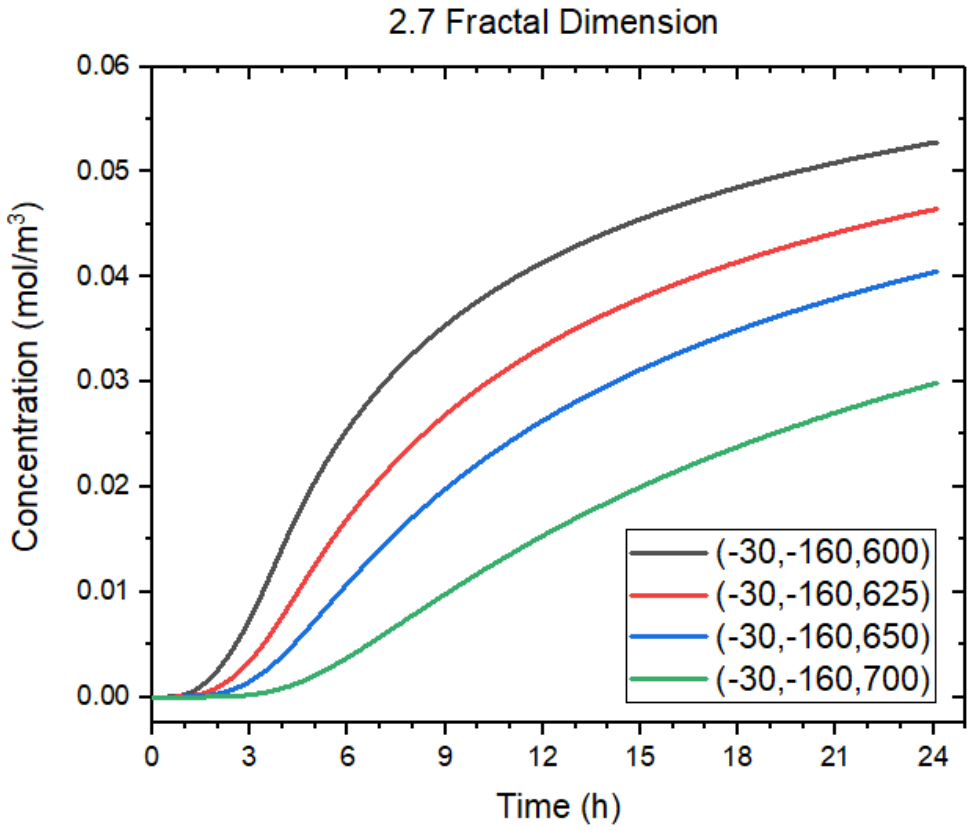

Figure 3.15. Temporal variation of species concentration measured at four selected locations within a microchannel containing a cluster of fractal dimension 2.7.

Both models with fractal dimension 2.3 and 2.7 show a similar tendency of elevated accumulation in the cancerous tissue zone. The analysis demonstrates that the most elevated concentration value is likely due to the disparities in geometry and mechanical properties between healthy and cancerous tissue.

The concentration values obtained in the probes at the 24-hour mark are listed in Table 3.13 for both fractal dimensions, where a moderate increase is detected on the model with fractal dimension of 2.3.

Table 3.13. Concentration point probes values on clusters with varying fractal dimension.

Probe	Z-coordinate [µm]	Concentration at t = 24 h for FD 2.3 [mol/m^3]	Concentration at t = 24 h for FD 2.7 [mol/m^3]
1	600	0.05578	0.05281
2	625	0.04913	0.04646
3	650	0.04286	0.04050
4	700	0.03170	0.02990

While this chapter establishes the baseline drug-free transport behavior when lacking any nanocarriers, the following chapter extends the model to incorporate nanoparticle-based delivery. This progression allows for an evaluation of how nanoparticle transport mechanisms behave and a comparison relative to the drug-free case.

4. Computational modeling of a nanoparticle-based drug delivery system in a cancerous nodule within a microchannel.

Nanoparticle-based drug delivery systems have attracted attention in recent years as a promising alternative for intraperitoneal delivery. This is mostly due to the benefits offered in cancer therapy, such as improved pharmacokinetics, enhanced tumor targeting, and reduced side effects and drug resistance [28].

Research has focused on analyzing the encapsulation of drugs in nanoparticles or other delivery systems to serve as an effective platform for anticancer agents [26]. The effects of different varieties of nanoparticles have been studied, including variations in material, size, shape, and surface properties [26,27,28,29,30].

4.1 Numerical simulation

A second model, designated as nanoparticle-based, assumes that the pharmaceutical agent is encapsulated in nanoparticles (NP), and administered as an NP-loaded solution through the intraperitoneal route (IP), assisted by passive targeting mechanisms as mentioned in section 2.3.

To ensure comparability between both approaches, the nanoparticle model retains the same geometric and material configuration established in the convection–diffusion model: a 1 mm^2 squared-cross section channel with a 6-mm length for fluid domain, and a 0.5-mm thickness of tissue wall; this volume is likewise considered as the analysis region for drug accumulation. Consequently, only the governing numerical interfaces and transport formulation are modified.

Nanoparticle-based model

The NP-based model was developed under these assumptions. Simulations were performed using COMSOL Multiphysics® [35] employing two physics interfaces: Free and Porous Media Flow and Particle Tracing for Fluid Flow, available through a project collaborator.

As in the convection-diffusion model, the fluid flow was modeled using the Free and Porous Media Flow module in COMSOL Multiphysics® [35], which was set up to solve the incompressible Navier-Stokes equations within a three-dimensional domain under stationary conditions. The momentum conservation is given by Equation 3.3, while mass conservation for incompressible flow is given by the continuity equation, Equation 3.4, both introduced in Chapter 3.

$$\rho(u_f \cdot \nabla)u_f = \nabla \cdot [-pI + \tau] + F \tag{3.3}$$

$$\nabla \cdot u_f = 0 \tag{3.4}$$

As for the administration of the drug-loaded nanoparticles, the “Particle Tracing for Fluid Flow” module was considered, as it has been deemed suitable for approximating the movement of NPs in the peritoneal cavity, given the scarcity of progress in this area. We propose the use of this module, as it has been employed for tracking in various application domains, including external flow. This module employs the results of the fluid flow field obtained in the module entitled “Free and Porous Media Flow”, and solves for the motion of a particle in a fluid in accordance with Newton's second law, as represented in Equation 4.1.

$$\frac{d(m_p v)}{dt} = F_t \tag{4.1}$$

where m_p is the particle mass, v is the particle velocity, and F_t is the net force which includes the drag, gravity, and other forces.

The initial nanoparticle properties were selected based on the representative NP systems suitable for paclitaxel encapsulation in Table 2.3, extracted from M. Souri, *et al.* [21]. From the available material formulations and loading strategies, a polymeric nanocarrier with a pre-loading approach was selected as a representative case, with a proposed diameter of 450 nm and a polymer density of $\rho_{NP}=1250\frac{kg}{m^3}$. For this set of parameters, a drug loading capacity of 42.6% was established, assuming solid-state behavior of the nanoparticles.

4.2 Numerical parameters of the model

4.2.1 Materials

The same three material domains previously described for the convection-diffusion model in Section 3.3.1 are assigned to the corresponding geometries of the nanoparticle model.

4.2.2 Boundary conditions

Free and Porous Media Flow

For the nanoparticle model, the fluid flow boundary conditions remain identical to those established for the convection–diffusion model, with modifications restricted to the particle transport interface. A constant inlet velocity of 30 μm/s was assigned at the channel inlet, while a reference pressure of P_o = 0 Pa was imposed at the channel outlet. No-slip condition on external boundaries of the microchannel for distal end of tissue domains and porous domains characteristics for healthy and cancerous tissue domains were considered as part of the model.

The initial conditions were stablished as u = 0 μm/s and P_0 = 0 Pa. All fluid flow boundary conditions are illustrated in Figure 4.1.

Particle Tracing for Fluid Flow

Boundary conditions were defined to represent localized drug release and a physiological clearance mechanism. Drug administration was modeled as the release of a nanoparticle (NP)-loaded solution via intraperitoneal injection, along with the interstitial fluid flow. A 100 mg drug mass, identical to that in the convection-diffusion model, was selected to ensure comparability between the two models.

Considering an identical dosage for paclitaxel as in the convection-diffusion model, a m_{drug} = 100 mg, considering the nanoparticle as a sphere the volume is calculated in Equation 4.2.

$$V = \frac{4}{3}\,\pi r^3 = 4.7713 \times 10^{-14}\ cm^3 \tag{4.2}$$

By using the proposed polymer density, the total mass of a single nanoparticle was calculated as $m_{NP}=5.96412\times10^{-14}$ g. Considering a drug loading capacity of 42.6%, the corresponding drug mass per nanoparticle was determined as $m_{drug/NP}=2.54071\times10^{-14}$ g.

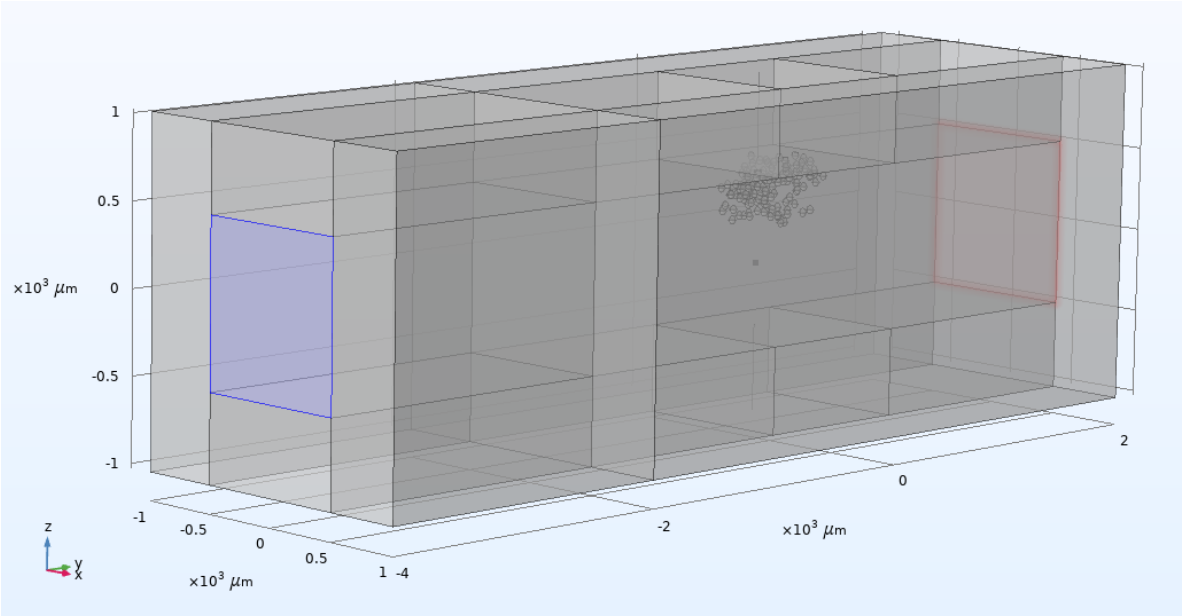

Figure 4.1. Fluid flow boundary conditions. Fluid flow velocity input u_{in}=30 µm/s (blue) and pressure outlet P_o = 0 Pa (red). Initial conditions are applied on all system domains.

For an intraperitoneal paclitaxel dose of 100 mg, the total nanoparticle mass required for delivery was estimated as $m_{NP,total}$ = 0.234742 g. Based on this total mass. the number of polymeric nanoparticles needed, assuming a diameter of 450 nm and 42.6% drug loading, was calculated as $N_{NPs,real}$ = 3.9359×10^{12} NPs. The parameters for drug and nanoparticles are condensed in Table 4.1.

In order to make the simulation computationally feasible, particle weighting was applied to reduce this quantity to a smaller number of numerical particles, as described in Equation 4.3. A particle release velocity parameter was calculated. A summary of the obtained values is presented in Table 4.2.

$$N_{num} = \frac{N_{real}}{PW} \tag{4.3}$$

where PW indicates the particle weighting equivalence used.

The boundary conditions established for this model consist of a single particle inlet located at the channel entrance. At this boundary, a total of N_{num} particles are released at an interval of n seconds. The initial release positions are uniformly distributed across the entire inlet area. Particles that come into contact with the tissue domains are assumed to adhere to these surfaces due to the enhanced permeability and retention (EPR) effect within the tumor microenvironment. Permanent adhesion on particles allows the analysis of an idealized system to evaluate the potential drug delivery to cancerous tissue.

For this instance of the study, it would be challenging to account for a recirculation of particles without a considerable margin of error, so the particles reaching the channel outlet are removed from the system. Additionally, no particle-particle interactions were considered in the present model, as the nanoparticles were assumed to be electrically neutral and thus Coulomb forces were therefore neglected. All boundary conditions are illustrated in Figure 4.2.

Table 4.1. Mass data for drug and nanoparticles.

Parameter	Symbol	Value
Mass per NP	m_{NP}	5.96412×10^{-14} g
Drug mass per NP	$m_{drug/NP}$	2.54071×10^{-14} g
Total NP mass for 0.1 g of drug	$m_{NP,total}$	0.234742 g
Number of polymeric NPs needed for dosage	N_{NPs}	3.9359×10^{12} NPs

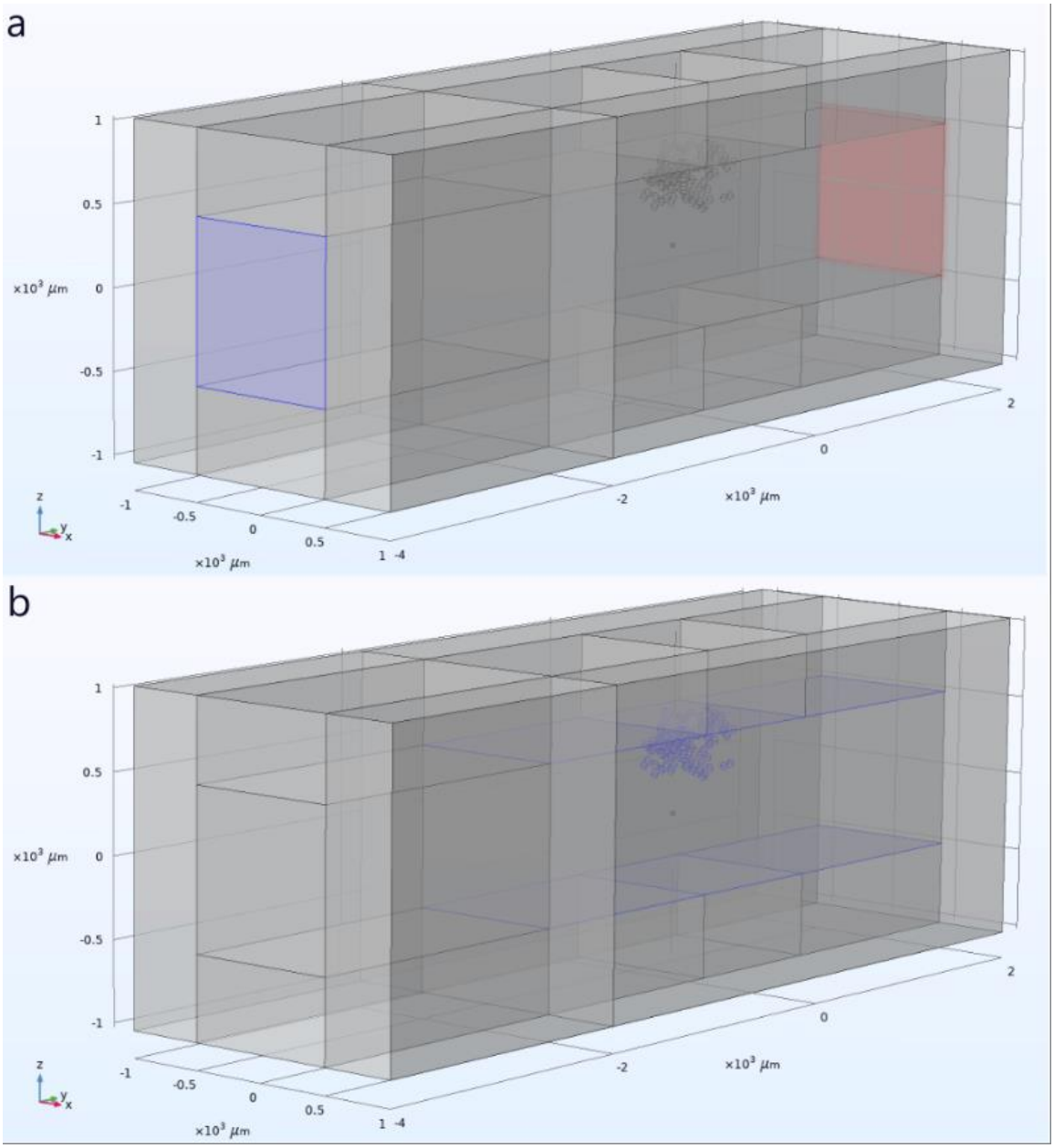

Figure 4.2. Species transport boundary conditions. [a] Particle inlet release (blue) and particle outlet clearance (red). [b] Particle adhesion on tissue surfaces (blue).

4.3 Computational model parameters

Two initial mesh independence studies were conducted. The first study was set up to assess the hydrodynamic aspect of the model, incorporating a stationary step. The second study was designed to calculate the results for the Particle Tracing module, incorporating a time-dependent step.

The parameters used for the mesh in the nanoparticle model match those of the convection–diffusion model, as the governing numerical interfaces of the Free and Porous Flow module are shared. Mesh configuration is shared in Table 4.2.

Table 4.2. Element size parameters for the mesh.

Element Domain	Fluid	Tissue
Mesh size	Fine	Finer
Calibration	Fluid dynamics	General physics
Maximum element size	60 µm	80 µm
Minimum element size	12.5 µm	12.5 µm
Maximum growth rate	1.13	1.35
Curvature factor	0.5	0.3
Narrow region resolution	0.8	0.85

The hydrodynamic stationary step study maintains a tolerance value of 0.0001, as in the convection-diffusion model, while the particle tracing study was configured to allow the tolerance to be controlled directly by the physics, which selects an average value of 10^{-5}.

4.4 Measurement approach

A particle counter feature was implemented to quantify particles located in a selected set of domains. Three counters were configured to account for distinct surface groups. The first counter was assigned to the cancerous tissue surfaces, including cell surfaces and the absorbing tissue boundaries located at z = 500 µm; the second counter for the healthy tissue surfaces at z = 500 µm; and the third for the healthy tissue surface at z = -500 µm.

For the particle weighting calibration phase, a fourth counter was introduced at the channel outlet. In this case, a particle adhesion configuration was applied to the boundary to retain particles that would have been removed from the system otherwise.

To determine the number of numeric particles (N_{num}) released at an interval of n seconds at the inlet boundary of the model, a particle weighting approach was proposed as an alternative to reduce the computational requirements of the model. Based on the total number of nanoparticles required to deliver a 100-mg dose, $N_{NPs} = 3.9359\times10^{12}$ NPs, the corresponding number of numerical particles was calculated for different weighting factors as shown in Table 4.3. Several particle weighting factors were evaluated for both fractal dimensions, calculating the total numerical particles amounted to each factor and the corresponding release rate for a 3 h infusion period. Accordingly, Table 4.3 reports the particle weighting factor, the equivalent number of real nanoparticles per numerical particle, the total number of numerical particles, the release rate of numerical particles, and the corresponding particle release schedule, including the number of numerical particles released per time interval.

Table 4.3. Particle weighting factors and release parameters for nanoparticle delivery.

Particle weighting factor, N_{NPs}/N_{num} [-]		Total numerical particles, N_{num}, [-]	Release rate, N_{NPs}/s, [-]	Particle release schedule [s]	N_{num} per release
10^9	1,000,000,000	3,935.90	0.3644	(0,3,10797)	1
5×10^8	500,000,000	7,871.80	0.7288	(0,1,10799)	1
3.5×10^8	350,000,000	11,245.43	1.0412	(0,1,10799)	1
1.02972×10^8	100,000,000	39,359.01	3.6443	(0,1,10799)	4
10^8	100,000,000	39,359.01	3.6443	(0,1,10799)	4
8.6007×10^7	86,007,000	45,762.57	4.2372	(0,3,10797)	9
5×10^7	50,000,000	78,718.03	7.2887	(0,1,10799)	7
4.55×10^7	45,500,000	86,408.37	8.0007	(0,1,10799)	8
10^7	10,000,000	393,590.15	36.4435	(0,1,10799)	37

Figure 4.3 shows the particle tracing results of the microchannel with a cluster of fractal dimension 2.3, here the numerical particles from the inlet boundary, adhere to the surfaces of the cancer cells and those that fail to adhere to them end up at the outlet. With results similar to those shown in the figure, different particle weighting factors were tested for both fractal dimension models.

The results for the models with fractal dimensions 2.3 and 2.7 are reported on Table 4.4 and 4.5, respectively. These results demonstrate that the particle weighting factor directly influences the total amount of drug deliver by the numerical model. With the total number of polymeric nanoparticles in surfaces at 24 h and the quantity of drug per nanoparticle, $m_{drug/NP} = 2.54071\times10^{-14}$ g, a value of total drug mass can be calculated. As the weighting value factor is varied, the number of numerical particles and the corresponding total number of polymeric NPs value change accordingly, affecting the drug mass delivered by the model.

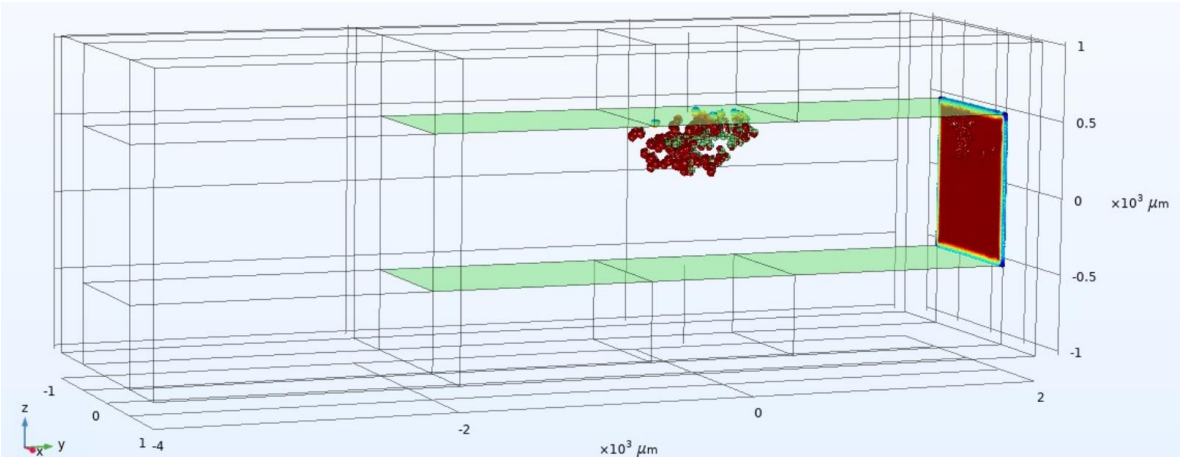

Figure 4.3. Particle tracing on tissue surfaces and outlet in microchannel with presence of a cluster of fractal dimension 2.3.

Table 4.4. Nanoparticle delivery and drug distribution at 24 h for varying particle weighting factors and release parameters for the model with fractal dimension 2.3.

Particle weighting factor, N_{NPs}/N_{num}, [-]		Particle release schedule [s]	Number of particles in surfaces at 24 h, N_{num}, [-]			Polymeric NPs, N_{NPs}, [-]	Drug mass [mg]	Moles of drug [mol]
			Outlet	Nodule	Total			
10^9	1,000,000,000	(0,1,10799)	3,113	445	3,558	3.5580E+12	90.3986	0.0001059
1.02972×10^8	100,000,000	(0,1,10799)	38,186	5,014	43,200	4.4484E+12	113.0209	0.0001324
10^8	100,000,000	(0,1,10799)	37,801	4,938	42,739	4.2739E+12	108.5876	0.0001272
8.6007×10^7	86,007,000	(0,2,10798)	43,010	5,590	48,600	4.1799E+12	106.2003	0.0001244
8.5×10^7	85,000,000	(0,3,10797)	41,341	5,459	46,800	3.9780E+12	101.0696	0.0001184
5×10^7	50,000,000	(0,2,10798)	71,456	9,544	81,000	4.0500E+12	102.8989	0.0001205
5×10^7	50,000,000	(0,3,10797)	69,843	9,357	79,200	3.9600E+12	100.6123	0.0001178
4.5554×10^7	45,554,000	(0,1,10799)	76,160	10,240	86,400	3.9355E+12	99.9991	0.0001171
3.5×10^7	35,000,000	(0,2,10798)	100,049	13,351	113,400	3.9690E+12	100.8409	0.0001181

Table 4.5. Nanoparticle delivery and drug distribution at 24 h for varying particle weighting factors and release parameters for the model with fractal dimension 2.7.

Particle weighting factor, N_{NPs}/N_{num}, [-]		Particle release schedule [s]	Number of particles in surfaces at 24 h, N_{num}, [-]			Polymeric NPs, N_{NPs}, [-]	Drug mass [mg]	Moles of drug [mol]
			Outlet	Nodule	Total			
10^9	1,000,000,000	(0,1,10799)	2,908	270	3,178	3.1780E+12	80.7439	0.0000946
5×10^8	500,000,000	(0,4,10796)	6,538	616	7,154	3.5770E+12	90.8813	0.0001064
3.5×10^8	350,000,000	(0,1,10799)	8,740	827	9,567	3.3485E+12	85.0745	0.0000996
1.02972×10^8	102,972,000	(0,1,10799)	34,871	3,352	38,223	3.9359E+12	99.9999	0.0001171
10^8	100,000,000	(0,1,10799)	34,871	3,352	38,223	3.8223E+12	97.1137	0.0001137
8.6007×10^7	86,007,000	(0,2,10798)	39,171	3,754	42,925	3.6919E+12	93.7994	0.0001098
8.5×10^7	85,000,000	(0,1,10799)	43,513	4,197	47,710	4.0554E+12	103.0348	0.0001207
8.5×10^7	85,000,000	(0,2,10798)	39,171	3,754	42,925	3.6486E+12	92.7011	0.0001086
8.5×10^7	85,000,000	(0,3,10797)	37,723	3,622	41,345	3.5143E+12	89.2889	0.0001046
5×10^7	50,000,000	(0,1,10799)	60,813	5,904	66,717	3.3359E+12	84.7544	0.0000993
5×10^7	50,000,000	(0,4,10796)	62,953	6,162	69,115	3.4558E+12	87.8007	0.0001028
5×10^7	50,000,000	(0,7,10793)	63,209	6,184	69,393	3.4697E+12	88.1539	0.0001032
10^7	10,000,000	(0,2,10798)	321,074	31,814	352,888	3.5289E+12	89.6587	0.0001050

Among the evaluated cases two selection strategies can be identified. The first one consists of adopting a single particle weighting factor that minimizes the error in both fractal dimension models. In this case, a weighting factor of 8.6007×10^7 calculates predicted drug masses of 93.7994 mg and

106.2003 mg for the 2.3 and 2.7 fractal dimension models, respectively; amounting to a drug mass difference of 6.2003 mg from the target dose of 100 mg.

The second strategy consists of selecting an independent particle weighting factor for each fractal dimension. For this approach, a weighting factor of 4.5554×10^{7} is selected for the fractal dimension 2.3 model which yields a predicted drug mass of 99.9991 mg. Similarly, for the fractal dimension 2.7 model, a weighting factor of 1.02972×10^{8} is selected, resulting in a predicted drug mass of 99.9999 mg.

Figures 4.4 to 4.7 show the particle tracing module results for both fractal dimensions, at 3 h and 24 h,

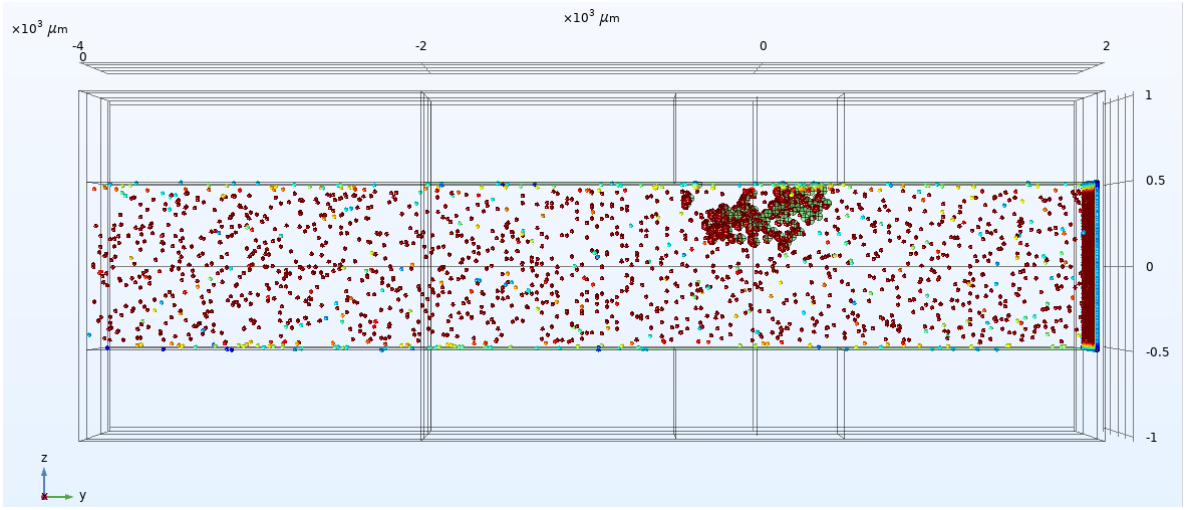

Figure 4.4. Particle distribution and accumulation in microchannel model with fractal dimension 2.3 for the nanoparticle-based delivery model at t = 3 h and PW=4.5554×10^{7}.

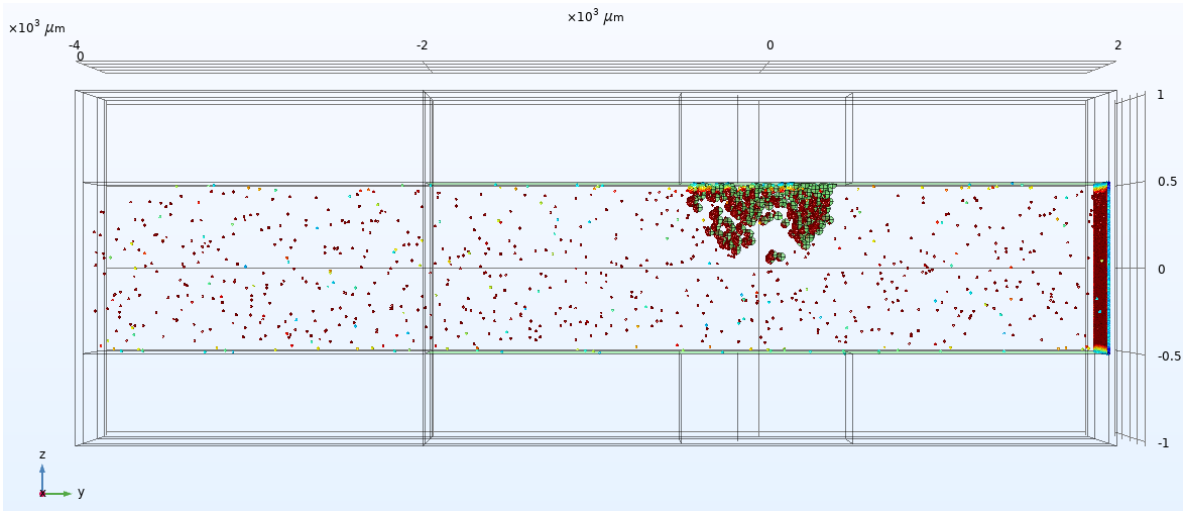

Figure 4.5. Particle distribution and accumulation in microchannel model with fractal dimension 2.7 for the nanoparticle-based delivery model at t = 3 h and PW = 1.02972×10^{8}.

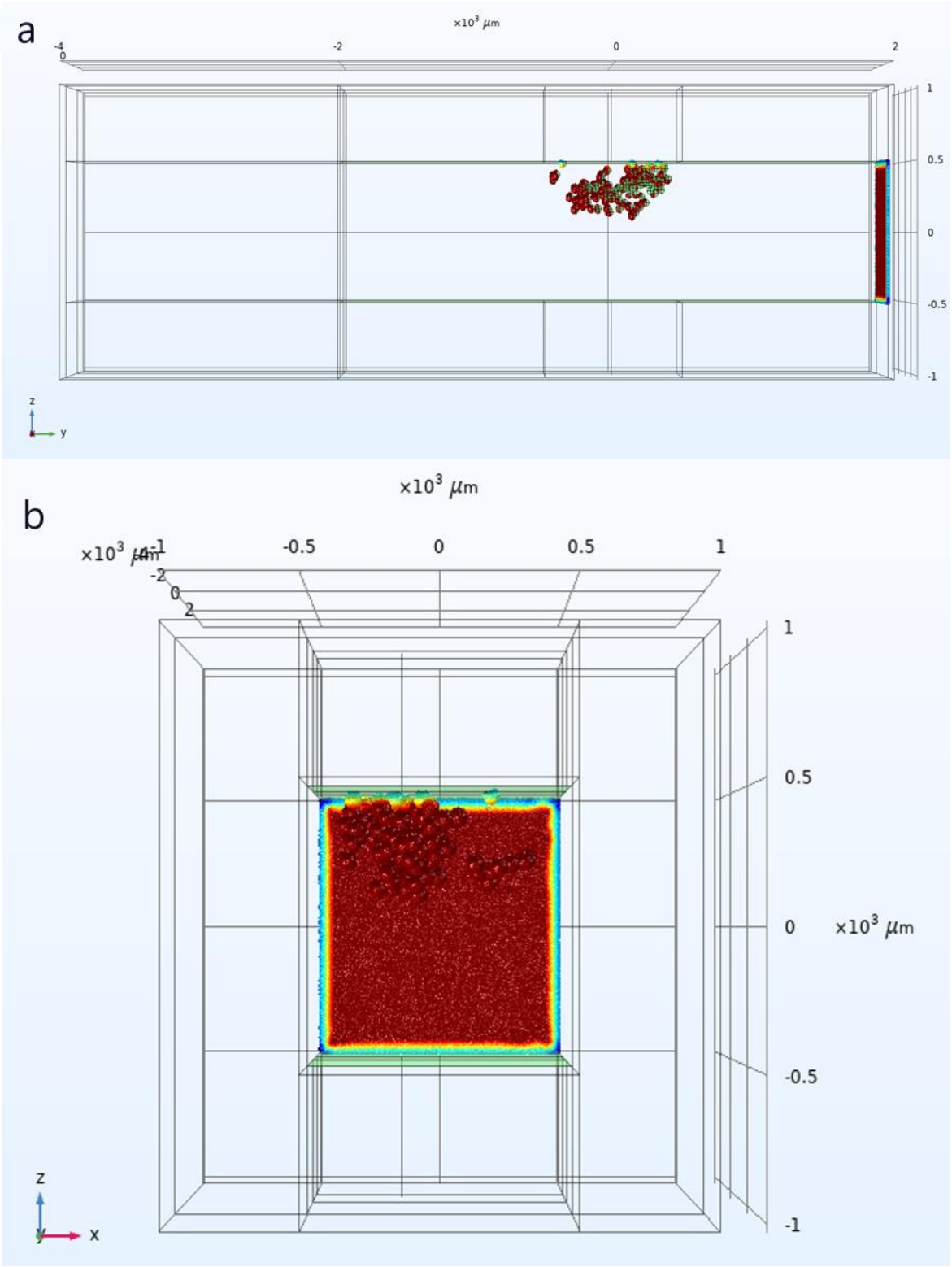

Figure 4.6. Particle distribution and accumulation in microchannel model with fractal dimension 2.3 for the nanoparticle-based delivery model at t = 24 h and PW=4.5554×10^{7}. Views in the *y*-*z* plane (a), and the *x*-*y* plane (b) are shown.

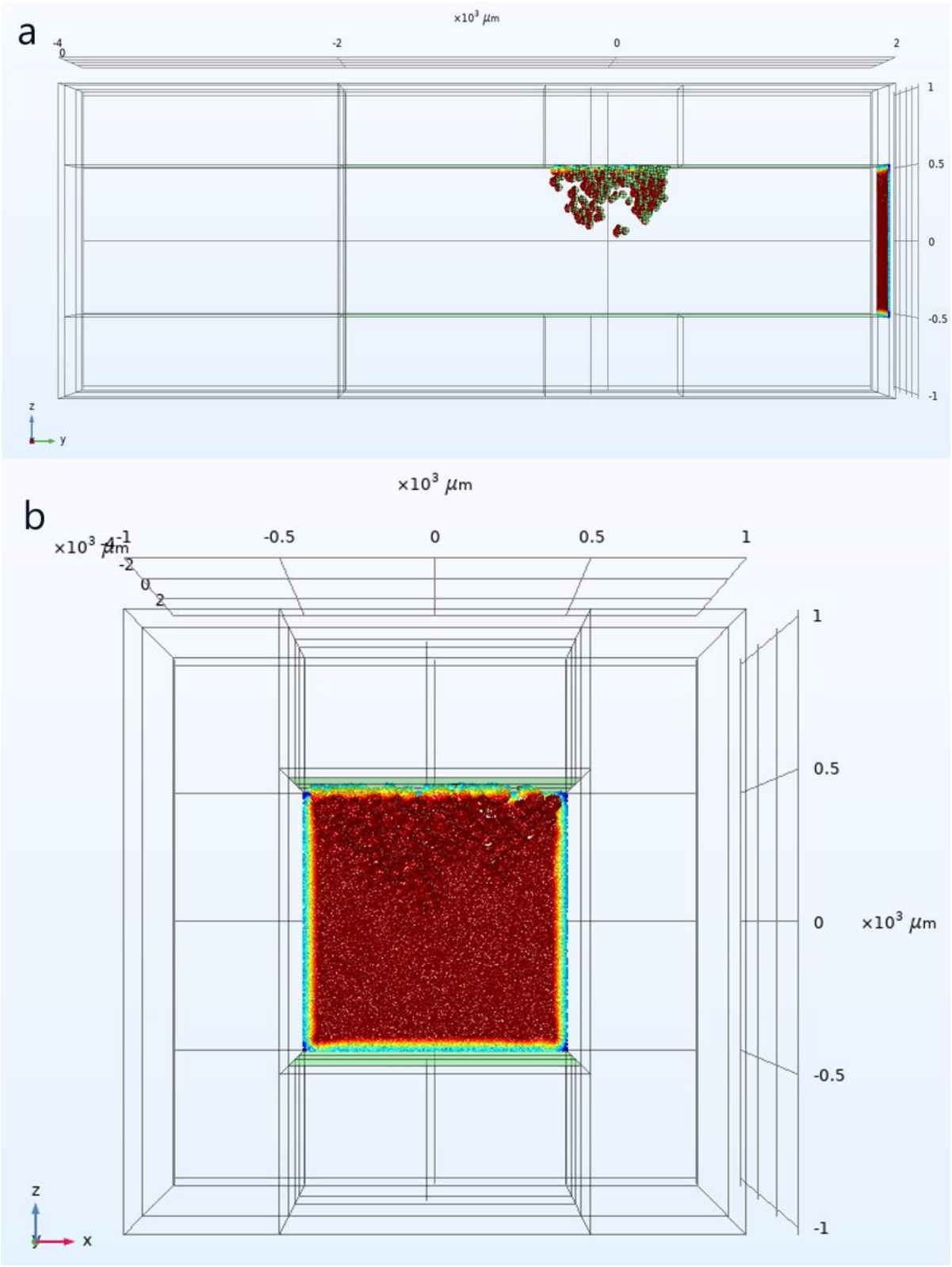

Figure 4.7. Particle distribution and accumulation in microchannel model with fractal dimension 2.7 for the nanoparticle-based delivery model at t = 24 h and PW=1.02972×10^{8}. Views in the *y-z* plane (a), and the *x-y* plane (b) are shown.

By now the baseline of both the drug-free and the nanoparticle-based transport behavior have been established, the following chapter extends the model to incorporate parameter variation for both models. This progression allows for an evaluation of how and which parameters influence drug accumulation and transport mechanisms in intraperitoneal drug delivery.

5. Identification of critical parameters and prediction of drug mass transfer dynamics.

Following the establishment of the model methodology for drug transport behavior in both convection-diffusion and nanoparticle-based models, a parametric analysis reviewing the influence of key parameters on drug delivery performance can now be evaluated. The behavior of each model is evaluated through concentration profiles as a function of time, allowing the identification of relevant mechanical parameters in the intraperitoneal drug accumulation process.

5.1 Convection-diffusion model

For the convection-diffusion model, a 100 mg dose of paclitaxel as a free-drug delivery is considered, as described in Chapter 3. A comparison between the fractal dimension 2.3 and fractal dimension 2.7 models is shown in Figure 5.1 based on the concentration profiles calculated for cancerous and healthy tissue domains with an inlet velocity of 30 μm/s. Although the overall cancerous tissue drug accumulation (C_{ct}) behavior remains consistent in both cases, the fractal dimension 2.3 model achieves a higher concentration value. This difference is attributed mainly due to the geometrical differences present between both fractal dimension models. The fractal dimension 2.3 model exhibits a lower structural density which contributes to the development of local velocity and pressure gradients that enhance species transport towards cancerous tissue domains.

A similar trend is observed with healthy tissue drug accumulation (C_{ht}), as fractal dimension 2.3 model presents a higher concentration value than fractal dimension 2.7. However, the concentration profile exhibits a different behavior compared with that of cancerous tissue domains. After finishing the 3-hour infusion period, the concentration presents a near asymptotic behavior and remains stable for the remaining 21 h of the simulation. This finding is consistent with the physiological lymphatic draining capacity of healthy tissues, which promotes foreign species clearance and prevents excessive accumulation. Figure 5.2 presents variation for inlet velocities, with most of the variability in concentration occurring between velocities of 10–50 μm/s, for both fractal dimensions. In contrast, the concentration profiles corresponding to velocities between 60-100 μm/s present a near identical temporal species accumulation, indicating a diminishing influence of velocity on species accumulation at higher flow rates.

A comparison of the drug mass accumulation within tissue domains for both fractal dimensions is provided in Figure 5.3. The accumulated drug masses average in the same order of magnitude for the fractal dimension 2.3 and fractal dimension 2.7 models. However, opposite trends are observed between the two types of tissues: For the cancerous tissue domain drug accumulation presents a decreasing trend with scaling inlet velocity, while drug accumulation in the healthy tissue domain exhibits an increasing trend.

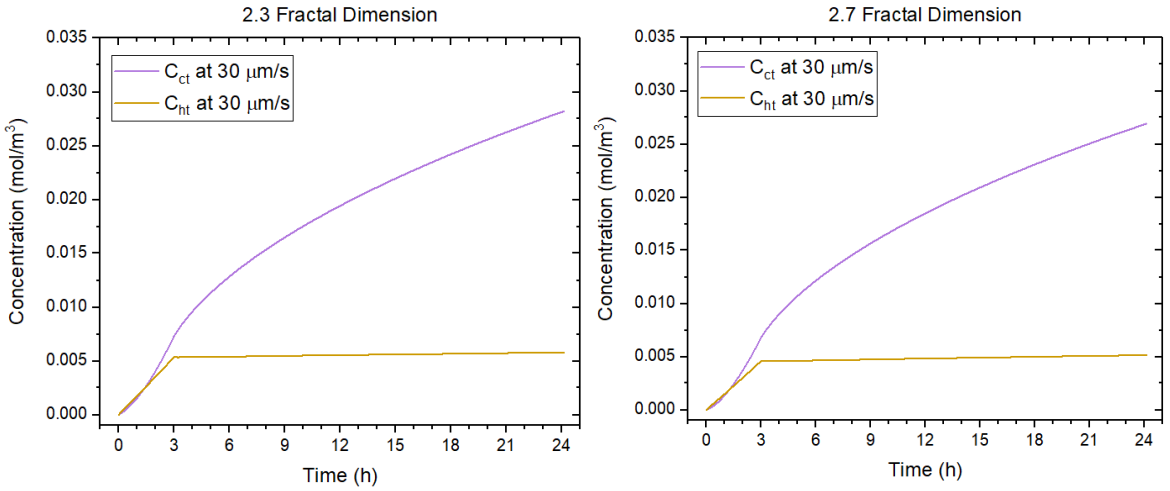

Figure 5.1. Molar drug accumulation by volume over time in tissue domains with inlet velocity of 30 μm/s for microchannel model with fractal dimension 2.3 and 2.7 for the convection-diffusion drug delivery model.

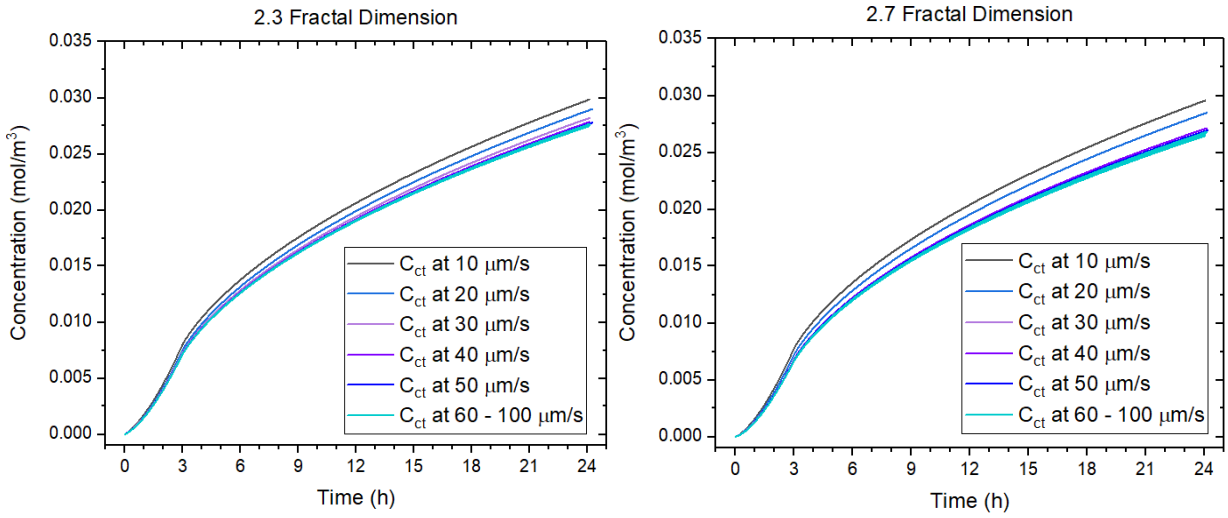

Figure 5.2. Molar drug accumulation by volume over time in cancerous tissue domains with inlet velocity variation between 10-100 μm/s for microchannel model with fractal dimension 2.3 and 2.7 for the convection-diffusion delivery model.

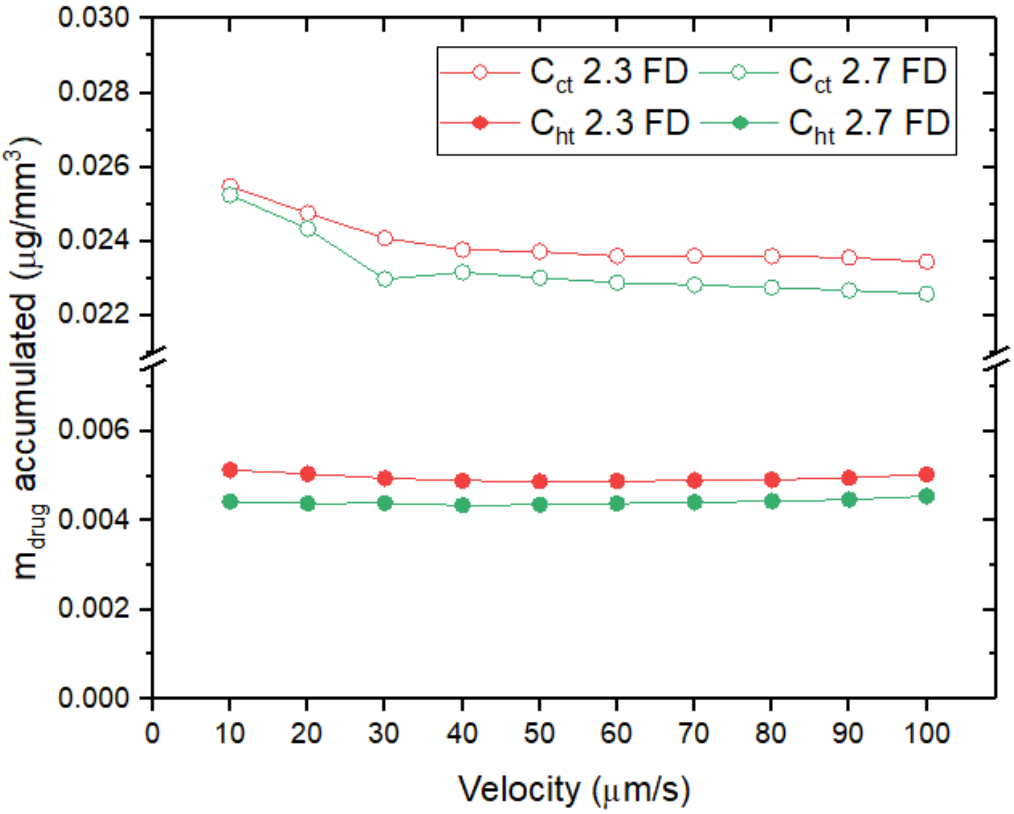

Figure 5.3. Drug mass accumulation in tissue domains with inlet velocity variation for microchannel model with fractal dimension 2.3 and 2.7 for the convection-diffusion-based delivery model at t = 24 h.

The results presented in Figure 5.4 show the comparison between accumulated concentration in cancerous tissue at different depths shown in Figure 3.7 for the model with 2.3 and 2.7 fractal dimension, represented as a solid line and scattered points, respectably. These results corroborate that the overall drug absorption behavior is independent of the development stage of the cancerous nodule, represented by the fractal dimension. Furthermore, the preceding argument that an increased concentration value is obtained in the model with 2.3 fractal dimension compared to that in the model with 2.7 fractal dimension is verified. With a direct comparison between 2.3 and 2.7 fractal dimension results the hypothesis is reinforced by the four depths analyzed for in cancerous tissue, the results obtained show a higher accumulation for 2.3 fractal dimension than for those of 2.7 fractal dimension.

Figure 5.5 illustrates the variation of molar concentration as a function of inlet velocity for the models with fractal dimension 2.3 and 2.7. For both fractal dimensions, a decrease of concentration with increasing velocity can be identified. The decline in concentration is more pronounced in the 2.7 fractal dimension model, while the 2.3 fractal dimension model exhibits a more moderate response to variation, this behavior may be linked to a reduced dependence on velocity-related changes in species transport.

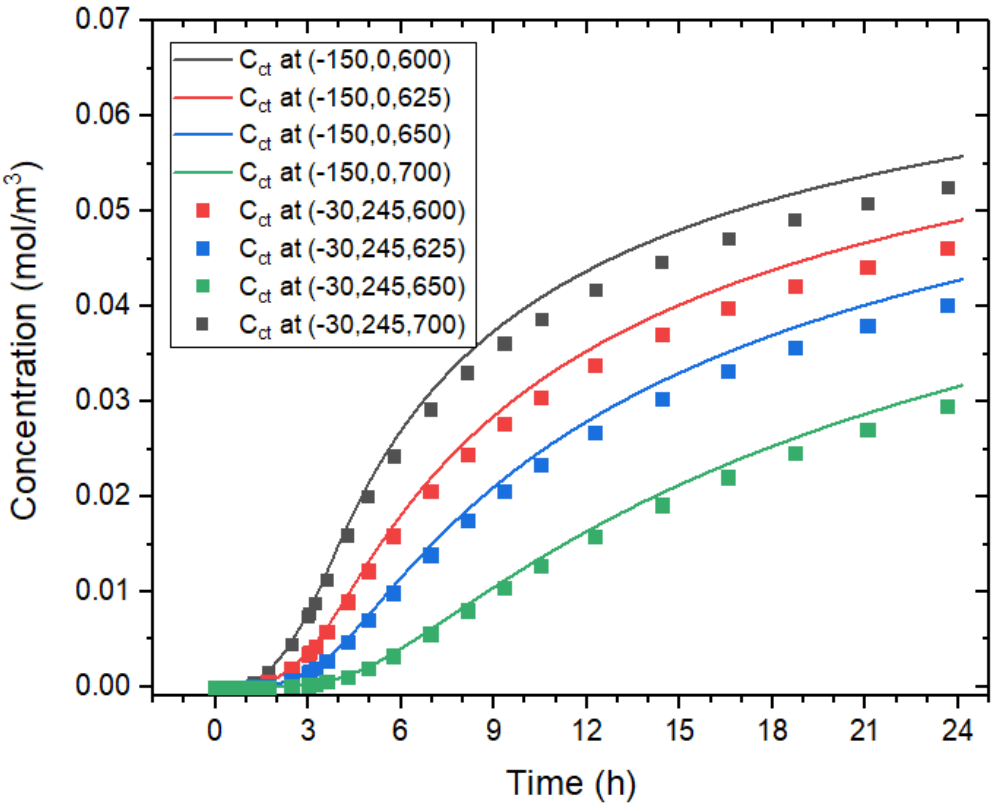

Figure 5.4. Concentration value by tissue depth with inlet velocity of 30 µm/s for microchannel model with fractal dimension 2.3 (solid line) and fractal dimension 2.7, (scatter) for the convection-diffusion delivery model.

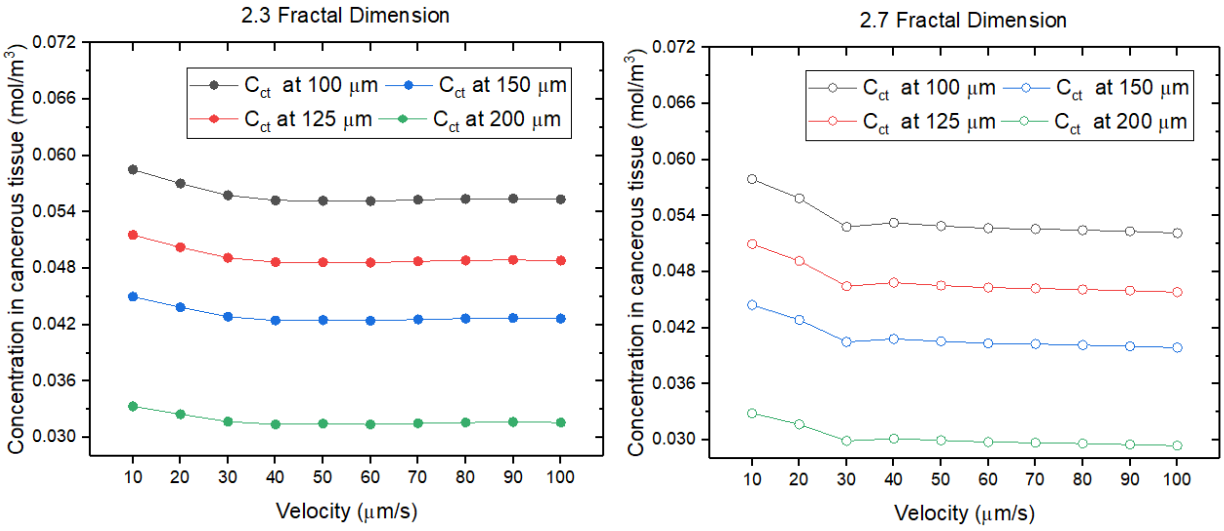

Figure 5.5. Concentration value comparison at 4 different tissue depths with variating inlet velocity between 10 - 100 µm/s for microchannel model with fractal dimension 2.3 (left) and fractal dimension 2.7 (right) for the convection-diffusion delivery model.

5.2 Nanoparticle-based model

As particles are released into the abdominal cavity, the Stokes number is evaluated to characterize the dynamics of particle motion in a certain flow, given by Equation 5.1.

$$St = \frac{\tau_p}{T_E} \tag{5.1}$$

where τ_p represents the particle relaxation time and T_E is the time scale of the fluid phase. For small spherical particles in the Stokes drag regime, $\tau_p = \frac{\rho_p d_p^2}{18\mu}$ where ρ_p is the particle density, d_p is the particle diameter and μ is the dynamic viscosity of the fluid. T_E can be evaluated as u/L where u is the fluid velocity and L is the characteristic length of the system [39,40]. Evaluating for a particle diameter range of 60 – 450 nm, and an inlet velocity range of 10 – 100 µm/s, the Stokes number (St) varies between 2.50×10^{-12} and 2.50×10^{-11} for 60 nm nanoparticles and between 1.41×10^{-10} and 1.41×10^{-9} for 450 nm nanoparticles. For both sizes the calculated Stokes number satisfies the condition that St << 1 by several orders of magnitude, which indicates that the particle inertia is negligible and that particle trajectories are determined by the fluid local streamlines [39,40].

Figure 5.6 and 5.7 present the results of the nanoparticle-based model in the form of two-dimensional plots, illustrating the variation of the number of numerical particles adhered to cancerous tissue surfaces over time, considering 450 nm nanoparticle size. The data in Figure 5.6 show that most of the particle adhesion occurs during the 3-hour infusion period of the nanoparticle-loaded solution, with surfaces retaining particles until the end of the 24-hour simulation. Additionally, particle adhesion profiles exhibit nearly identical temporal evolution trends for all evaluated velocities, indicating that velocity primarily affects the rate of particle accumulation rather than overall adhesion behavior, as shown in Figure 5.7.

Moreover, Figure 5.6 shows that overall temporal accumulation behavior in particle adhesion profiles for both fractal dimensions remains similar despite differences in particle weighting factors and the geometric distribution. Quantitatively, the fractal dimension 2.3 model exhibits a higher accumulation of nanoparticles in comparison to the fractal dimension 2.7 model, resulting in a higher potential dose delivery to the cancerous nodule.

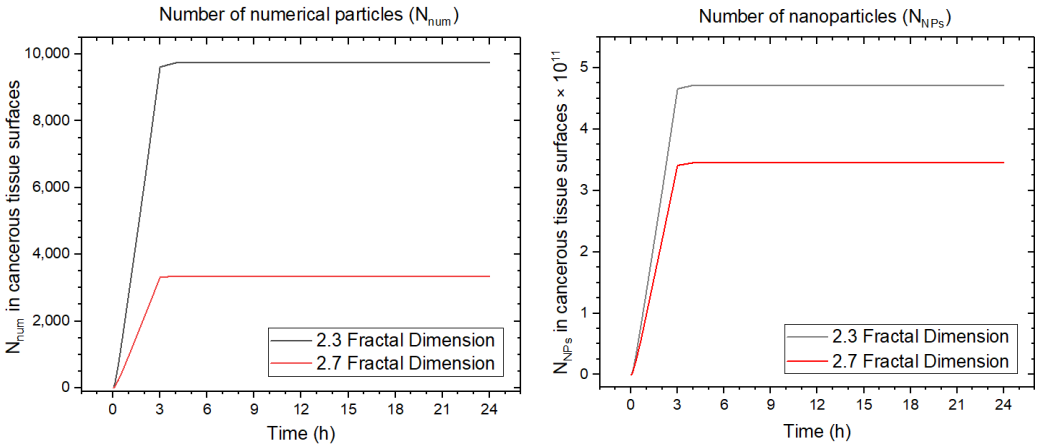

Figure 5.6. Numerical particle and nanoparticle accumulation over time in cancerous surfaces with inlet velocity of 30 µm/s for microchannel model with fractal dimension 2.3 for PW=4.5554×10^{7} and 2.7 for PW=1.02972×10^{8} with 450 nm nanoparticle size for the nanoparticle-based delivery model.

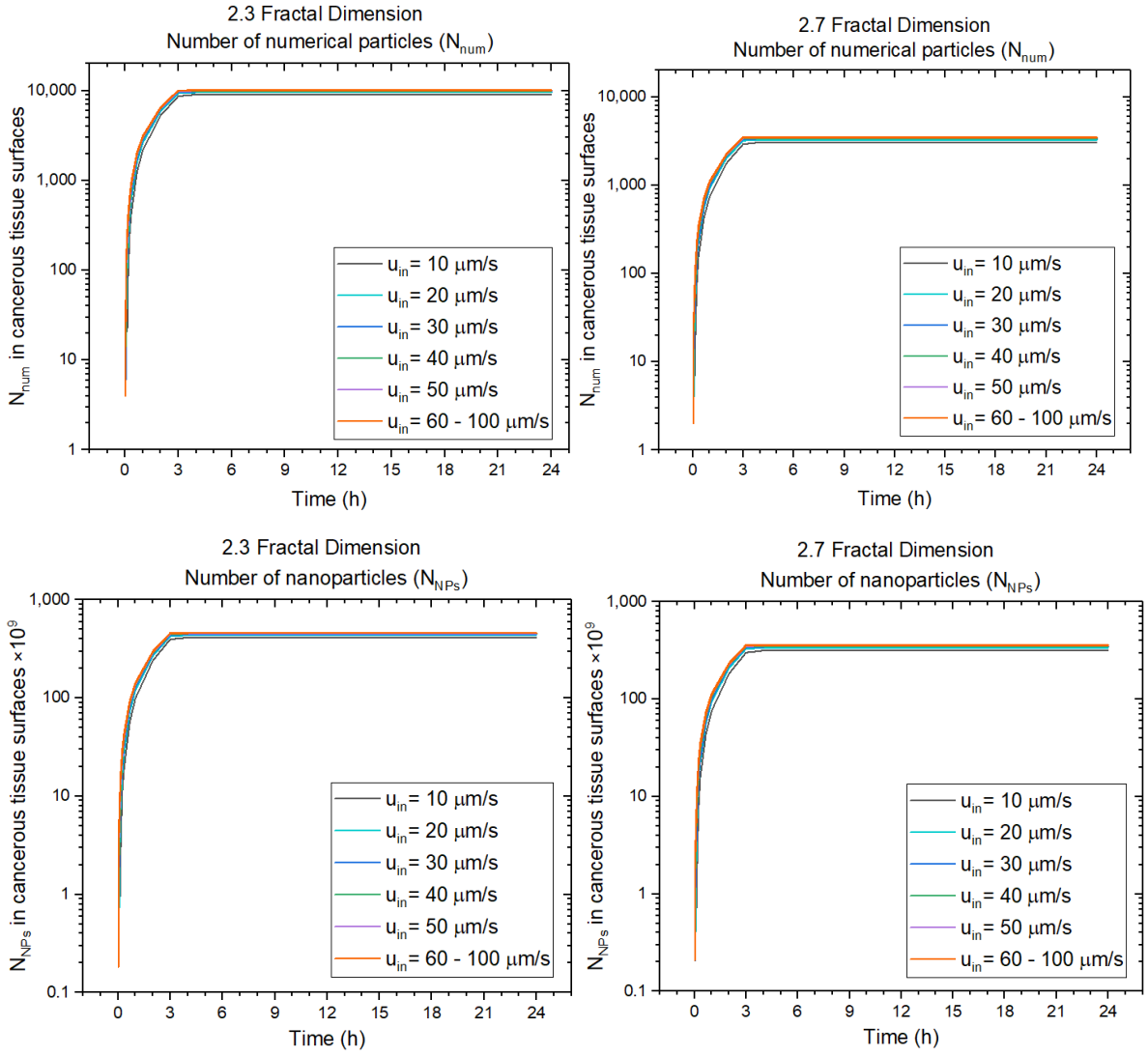

Figure 5.7. Numerical particle and nanoparticle accumulation over time in cancerous surfaces with variating inlet velocity between 10 – 100 μm/s for microchannel model with fractal dimension 2.3 for PW=4.5554×10^7 and 2.7 for PW=1.02972×10^8 with 450 nm nanoparticle size for the nanoparticle-based delivery model.

Figure 5.8 and 5.9 display numerical particle accumulation for different values of inlet velocity after a 24-hour period of time in both 2.3 and 2.7 fractal dimension models with 450 nm nanoparticle size. The data for both cases indicate a gradual increase in the number of particles adhered to cancerous tissue surfaces with the increase of inlet velocity, suggesting enhanced particle transport toward the tumor region.

For the 450 nm nanoparticle size the 2.3 fractal dimension model employs a particle weighting factor (PW) of 4.5554×10^7 nanoparticles per numerical particle in the model, this factor enables the model to reach a total model concentration of 99.9991 mg out of the 100 mg objective dose of paclitaxel. The number of numerical particles in cancerous tissue surfaces ranges from 9,086 to 10,165 due to varying inlet velocities.

Meanwhile, the 2.7 fractal dimension model employs a particle weighting factor (PW) of 1.02972×10^{8} nanoparticles per numerical particle. As each numerical particle amounts for a larger number of nanoparticles, the number of particles adhered to cancerous surfaces decreases significantly from the previous fractal dimension, to a range of 3,068 to 3,520.

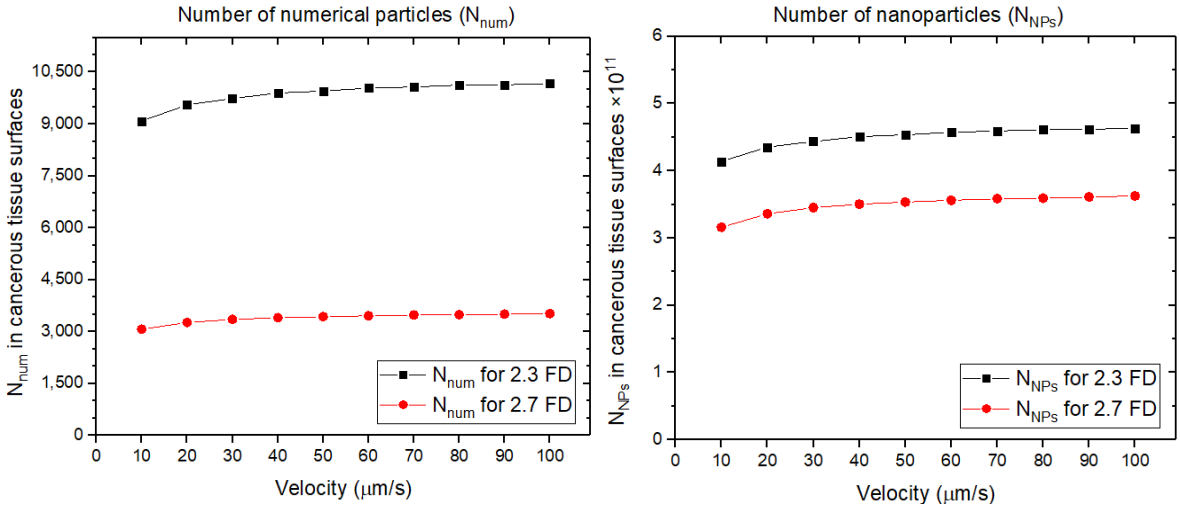

Figure 5.8. Numerical particle and nanoparticle accumulation in cancerous surfaces with inlet velocity variation for microchannel model with fractal dimension 2.3 for PW=4.5554×10^{7} and 2.7 for PW=1.02972×10^{8} with 450 nm nanoparticle size for the nanoparticle-based delivery model at t = 24 h.

Figure 5.9 presents the results of the nanoparticle-based model considering a reduction in nanoparticle size to 60 nm. The data in Figure 5.9 show that most of the particle adhesion occurs during the 3-hour infusion period of the nanoparticle-loaded solution in both fractal dimensions, replicating the behavior previously observed with the 450 nm nanoparticles.

Cancerous tissue surfaces retain particles until the end of the 24-hour simulation, which corroborates that particle adhesion profiles previously observed present nearly identical temporal evolution trends for all evaluated velocities. This indicates that velocity primarily affects the rate of particle accumulation rather than overall adhesion behavior, as shown in Figure 5.7.

Figure 5.10 exhibits numerical particle accumulation for different values of inlet velocity after a 24-hour period of time in both 2.3 and 2.7 fractal dimension models with 60 nm nanoparticle size. A similar trend is observed to that of the 450 nm nanoparticle size, a gradual increase in the number of particles adhered to cancerous tissue surfaces with the increase of inlet velocity is identified, suggesting enhanced particle transport toward the tumor region.

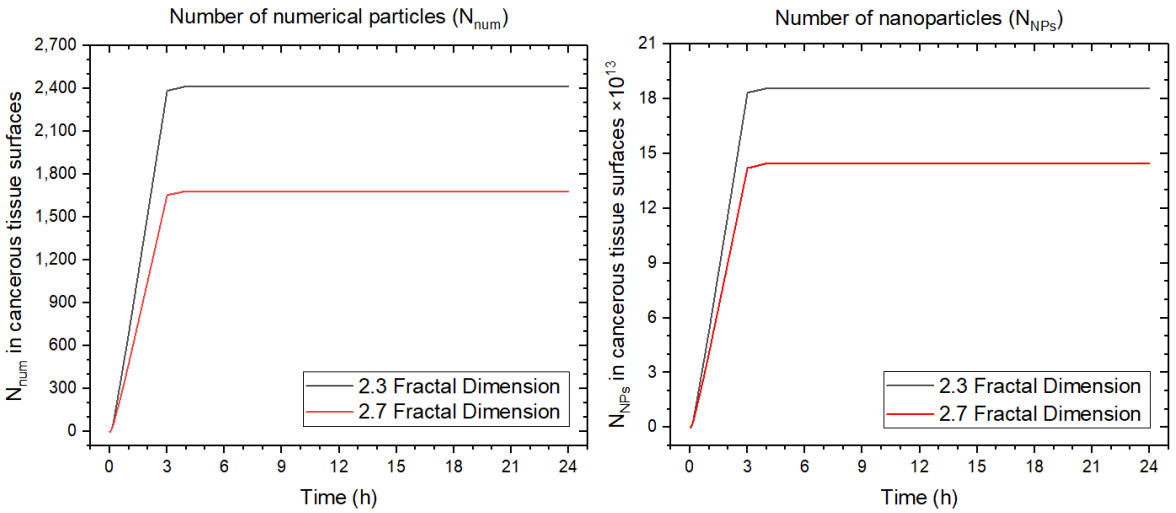

Figure 5.9. Numerical particle and nanoparticle accumulation over time in cancerous surfaces with inlet velocity of 30 µm/s for microchannel model with fractal dimension 2.3 for PW= 7.6873×10^{10} and 2.7 for PW=8.58917×10^{10} with 60 nm nanoparticle size for the nanoparticle-based delivery model.

Numerical particle accumulation over time with 60 nm nanoparticle size does not differ much from the behavior shown in Figure 5.7 with 450 nm nanoparticle size; therefore, it has been omitted from this analysis, as it provides no new information.

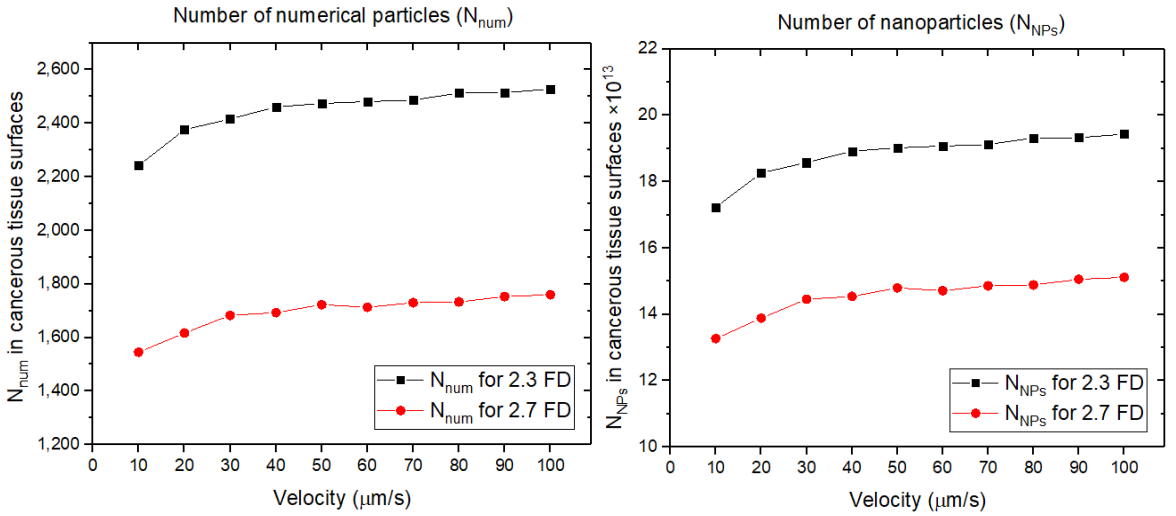

Figure 5.10. Numerical particle and nanoparticle accumulation in cancerous surfaces with inlet velocity variation for microchannel model with fractal dimension 2.3 for PW= 7.6873×10^{10} and 2.7 for PW=8.58917×10^{10} with 60 nm nanoparticle size for the nanoparticle-based delivery model at t = 24 h.

The number of particles can amount to a drug dosage in mg using Equation 4.3 and drug mass value per NP ($m_{drug/NP}$) from Table 4.1. For the 60 nm nanoparticles, the number of numerical particles adhered to cancerous tissue surfaces shown in Figure 5.10, ranges from 2,242 and 2,528 in the 2.3 fractal dimension model. In contrast, in the 2.7 fractal dimension model ranges between 1,545 and 1,760, exhibiting a lower particle count due to the difference in particle weighting factors between the two fractal dimensions.

Analyzing the numerical particle values for 450 nm NPs exhibited in Figure 5.8 amount to an increment ranging from 10.5161 mg to 11.7649 mg of paclitaxel for fractal dimension 2.3. Meanwhile, based on the numerical particle values in cancerous tissue surfaces for fractal dimension 2.7, the delivered paclitaxel dose is estimated to range from 8.0266 mg to 9.2091 mg.

For the numerical particle values for 60 nm NPs exhibited in Figure 5.10 amount to an increment ranging from 10.3796 mg to 11.7037 mg of paclitaxel for fractal dimension 2.3. Meanwhile, based on the numerical particle values in cancerous tissue surfaces for fractal dimension 2.7, the delivered paclitaxel dose is estimated to range from 7.9919 mg to 9.1041 mg.

The difference in drug mass accumulation between the two fractal dimension models in this analysis is observed in Figure 5.11, two nanoparticle sizes are exhibited with both fractal dimensions. The drug variation is attributed to differences in the internal structure of the cancerous nodule, the model with lower fractal dimension presents a lower structural density, generating larger void spaces that promote the formation of velocity and pressure gradients, which facilitate particle transport directly towards the cancerous tissue surfaces, resulting in increased particle adhesion and drug accumulation. Additionally, a subtle improvement in drug mass accumulation can be identified when comparing the two nanoparticle sizes, in favor of the larger nanoparticle size.

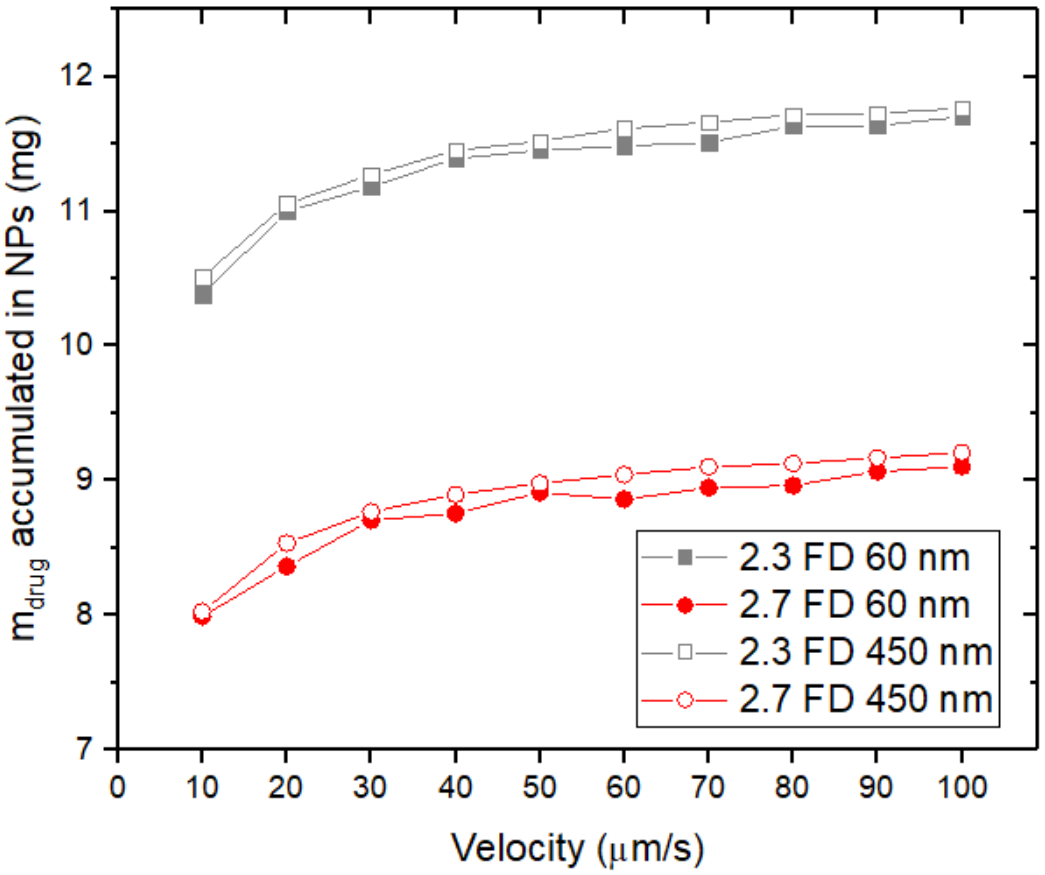

Figure 5.11. Drug mass accumulation in cancerous surfaces with inlet velocity variation for microchannel model with fractal dimension 2.3 and 2.7 with 450 nm nanoparticle size for the nanoparticle-based delivery model at t = 24 h.

A comparison between the convection-diffusion and nanoparticle-based models in Figure 5.3 and 5.11 reveals opposite responses to an increase in velocity. For the convection-diffusion model, cancerous tissue concentration decreases as inlet velocity increases, suggesting that a decrease in local drug residence time due to higher velocities affects diffusion capability into cancerous tissue and focuses instead in promoting drug transport downstream. This behavior is undesirable, as the drug may subsequently accumulate in other healthy tissues, contributing to discomfort and other side effects, or may be cleared by the lymphatic system before recirculating to the vicinity of the cancerous tissue. In contrast, the nanoparticle-based model exhibits an increase in accumulated drug mass with increasing velocity, indicating that enhanced velocity particle transport promotes favorable interactions between particle-tissue, improving subsequent adhesion. Some of the interactions may be related to enhanced particle penetration into tumor structure, directly increasing interactions between particle and surfaces, leading to adhesion events.

Additionally, for the development stage study both models consistently show greater drug accumulation in the geometry with fractal dimension 2.3 compared to the fractal dimension 2.7, supporting the previously stated hypothesis that the lower structural density of the fractal dimension 2.3 model generates gaps capable of promoting transport pathways and stronger local velocity gradients, facilitating drug transport towards cancerous tissue domains, this effect can be considered independent of the drug delivery method, whether it presents as free-drug transport or nanoparticle carriers.

In terms of velocity variation, even though the general behavior is an increase/decrease of drug accumulation. The gradient presented in the variation from 10 to 30 μm/s for inlet velocity is more pronounce and then gradually approaches an asymptotic trend. This can be observed in both drug delivery methods, but more strongly on the nanoparticle model, where both fractal dimensions and nanoparticle sizes present the same pattern.

Conclusions.

The results obtained through numerical simulation allow us to interpret the drug mass transfer behavior in biological tissue using both free drug delivery and nanoparticle-based drug delivery methods. A model representing a cancerous nodule was successfully constructed, with different stages of development represented by the fractal dimension of the structure.

Numerical models allow us to estimate a value for the drug absorption profile using parametric analysis, these models enable the reproduction of various hydromechanical conditions within the channel and help predict the behavior of the system under different conditions. An analysis of the accumulated drug concentration in the cancerous nodule, generated by the interstitial flow field was performed using a cluster model with a more complex geometry than those that can be constructed for *in vivo* experiments.

For free-drug delivery an average drug concentration was analyzed in healthy and cancerous tissue domains, the value presents a decreasing trend with increasing fluid velocity along with a reduction of the rate of decrease, suggesting that the influence of fluid velocity in temporal drug accumulation diminishes in higher flow rates. Meanwhile, analysis of the temporal variation in tissue concentration exhibits that during infusion period both types of tissue present a rapid increase in concentration but the behaviors diverge after the 3-hour period. Concentration in cancerous tissue domains continues to increase with a gradually decreasing accumulation rate due to continued transport after the end of drug administration, whereas concentration in healthy tissue domains present a near-asymptotic behavior with a virtually no increase, leading to an increasing concentration gradient between cancerous and healthy tissues over time, indicating enhanced drug accumulation within the cancerous nodule. This finding presents consistency with the physiological lymphatic draining capacity of healthy tissues, which promotes foreign species clearance. Although this effect is not evident within the 24-hour simulation period, it is expected to present over longer time scales.

For the nanoparticle-based drug delivery the concentration values is measured through the number of particles adhered to cancerous tissue surfaces, the drug load in particles is accounted as the potential drug mass to be released into the cancerous nodule. The temporal adhesion gradient for particles exhibit a rapid increase during the infusion period, after which the nodule is assumed to retain the particles throughout the remainder of the simulation. An increasing trend is observed between fluid velocity and particle adhesion, with higher velocities leading to a higher number of drug-loaded particles adhered to the nodule. Particle size was also considered as a possible variable to increase drug accumulation, the results yielded a small increase in drug mass favored towards larger particles.

The difference in observed behavior for increasing velocity on free-drug and nanoparticle models is inferred to be due to the contrast in the drug absorption mechanisms. In the case of free-drug delivery, a lower fluid velocity results in a prolonged drug exposure time in comparison to high fluid velocities, allowing drug transport mechanisms to interact with tissue domains for a longer period. In contrast, nanoparticle delivery derives little benefit from prolonged drug exposure time due to the lack of particle recirculation assumption in the model. Therefore, drug-loaded nanoparticles instead mostly benefit on an increase in fluid velocity to produce higher drug mass values.

Nevertheless, in both models, the most defining factor for drug mass accumulation is the stage of development of the cancerous nodule. In the tumor model with a fractal dimension of 2.3, a tumor at an intermediate stage of development with 129 cells is represented, while the tumor model with a fractal dimension of 2.7 represents a tumor at an advanced stage of development with 232 cells. The

model with fractal dimension of 2.3 presents a higher concentration value than the model with fractal dimension of 2.7. This difference is presumed to result from a lower cellular density associated with the stage of development of the cancerous nodule, which promotes the formation of local velocity and pressure gradients, enhancing convective drug mass transport towards cancerous tissue, increasing drug accumulation.

Future work

The study of the mechanical aspects of drug delivery to cancerous nodules within the peritoneal cavity, has resulted in several specific ideas that should be revisited in future studies in this area of research. Among them are:

- Analysis of multiple geometric configurations for each fractal dimension: It is recommended that the study be extended to include multiple geometric configurations representing each of the fractal dimensions evaluated. This approach would help determine whether the observed transport behavior trends are consistent, providing stronger support for the hypotheses proposed in this work.
- Broaden the geometric analysis. Evaluating additional fractal dimensions would provide a better overview of the relationship between geometric complexity and drug transport phenomena.
- Increase in parametric variability: The numerical models can be used to evaluate a wider range of tissue and fluid properties, such as tissue characteristics representative of different types of cancerous nodules, heterogeneous permeability distributions, and refined fluid properties for malignant ascites.
- Refine the nanoparticle-based model. Variations to represent a more accurate method of nanoparticle delivery can provide improved results for future analysis, such as considering additional interaction mechanisms, improved release kinetics, particle characteristic variation.
- Experimental validation of computational model. The numerical modeling results should be validated with experimental or clinical data to directly assess the accuracy of the proposed models and provide predictive capability under clinically relevant conditions. Early experiments could revolve around recreating the model geometry and incorporating several types of tissue to characterize drug absorption parameters and recreate the simulated mechanics.

References

1. S. Bilbao and M. Lloret, “Invasión y metástasis,” in *Principios generales del cáncer*, Madrid, Spain: Arán Ediciones, 2012, pp. 55-63.
2. J. A. Monasterio, “Modelado de la metástasis de un nódulo canceroso”, B.S. thesis, Fac. Ing., UASLP, San Luis Potosí, San Luis Potosí, México, 2023.
3. M. T. Martín de Civetta, and J. D. Civetta. “Carcinogénesis”, *Salud Pública Mex*, Vol. 53, pp. 405-414, 2011.
4. L. Elkington, P. Adhikari, and P. Pradhan, “Fractal dimension analysis to detect the progress of cancer using transmission optical microscopy,” *Biophysica*, vol. 2, pp. 59–69, 2022.
5. B. P. Rickard, *et al.*, “Malignant Ascites in Ovarian Cancer: Cellular, Acellular, and Biophysical Determinants of Molecular Characteristics and Therapy Response”, *Cancers*, 13, 4318, 2021.
6. N. Ahmed and K.L. Stenvers, “Getting to know ovarian cancer ascites: opportunities for targeted therapy-based translational research,” *Front Oncol.*, vol. 3, Art. no. 256, 2013.
7. Q. Huang, X. Hu, *et al.*, “Fluid shear stress and tumor metastasis,” *Am. J. Cancer Res.*, vol. 8, no. 5, pp. 763-777, 2018.
8. H.K. Pannu and M. Oliphant, “The subperitoneal space and peritoneal cavity: basic concepts,” *Abdom. Imaging*, vol. 40, no. 7, pp. 2710-2722, 2015, doi: 10.1007/s00261-015-0429-5.
9. I. Rizvi, *et al.*, “Flow induces epithelial-mesenchymal transition, cellular heterogeneity and biomarker modulation in 3D ovarian cancer nodules”, *Proc. Natl. Acad. Sci. U. S. A.*, 2013.
10. H. Gray, *Anatomy of the Human Body*, Philadelphia, PA, USA: Lea & Febriger, 1918. [Online]. Available: Bartleby.com, 2000.
11. E. H. Wissler, *Human Temperature Control. A Quantitative Approach*, Germany: Springer, 2018, doi: 10.1007/978-3-662-57397-6.
12. J.D. Shields, *et al.* “Autologous chemotaxis as a mechanism of tumor cell homing to lymphatics via interstitial flow and autocrine CCR7 signaling,” *Cancer Cell*, vol. 11, no. 6, pp. 526–538, 2007.
13. W.J. Polacheck, J.L. Charest, and R.D. Kamm, “Interstitial flow influences direction of tumor cell migration through competing mechanisms,” *Proc. Natl. Acad. Sci. U. S. A.*, vol. 108, no. 27, pp. 11115–11120, 2011.
14. O.L. Torres-Saucedo, B. Morales-Cruzado, and F.G. Pérez-Gutiérrez, “Experimental determination of shear stresses on an artificial transcoelomic metastasis model using optical tweezers: A comparison with numerical simulation,” *Lasers Surg. Med.*, vol. 54, no. 7, pp. 1027–1037, 2022, doi:10.1002/lsm.23554.
15. C.K.M. Ip, et al., “Stemness and chemoresistance in epithelial ovarian carcinoma cells under shear stress,” *Sci. Rep.*, vol. 6, art. no. 26788, 2016, doi: 10.1038/srep26788.
16. D.A. Robledo, “Caracterización de un modelo de corriente intersticial alrededor de un nódulo

canceroso en un flujo oscilatorio utilizando pinzas ópticas," M.S. thesis, CIEP, UASLP, San Luis Potosí, San Luis Potosí, México, 2021.

17. J. Ferlay, *et al.*, "Cancer statistics for the year 2020: An overview," *Int. J. Cancer*, 2021, doi: 10.1002/ijc.33588.

18. R. A. Weinberg, and C. L. Chaffer, "A Perspective on Cancer Cell Metastasis," *Science*, vol. 331, no. 6024, pp. 1559–1564, 2011, doi:10.1126/science.1203543.

19. D.S. Alberts, *et al*., Eds., *Intraperitoneal Therapy for Ovarian Cancer*, Berlin, Heidelberg, Germany: Springer-Verlag, 2010, doi: 10.1007/978-3-642-12130-2.

20. L. Preziosi, Ed., *Cancer Modelling and Simulation*, 1st ed. Boca Raton, FL, USA: CRC Press, 2003, doi: 10.1201/9780203494899.

21. M. Souri, *et al.*, "Towards principled design of cancer nanomedicine to accelerate clinical translation," *Mater. Today Bio*, vol. 13, art. no. 100208, 2022, doi: 10.1016/j.mtbio.2022.100208.

22. S.K. Bardal, J.E. Waechter, and D.S. Martin, *Applied Pharmacology*, St. Louis, MO, USA: Elsevier, 2011.

23. National Center for Biotechnology Information, "PubChem Compound Summary for CID 36314, Paclitaxel," 2025. [Online]. Available: https://pubchem.ncbi.nlm.nih.gov/compound/Paclitaxel.

24. U.S. Food and Drug Administration, *TAXOL® (paclitaxel) injection label*, 2011.

25. V. Danesi, *et al.*, "Body weight and body surface area of adult patients with selected cancers: An Italian multicenter study," *PloS one*, vol. 19, no. 12, art. no. e0314452, 2024, doi: 10.1371/journal.pone.0314452.

26. G. Bajaj, and Y. Yeo, "Drug delivery systems for intraperitoneal therapy," *Pharm. Res.*, vol. 27, no. 5, pp. 735–738, 2010, doi: 10.1007/s11095-009-0031-z.

27. C. Li, *et al.*, "Recent progress in drug delivery," *Acta Pharm. Sin. B*, vol. 9, no. 6, pp. 1145–1162, 2019, doi:10.1016/j.apsb.2019.08.003.

28. Y. Yao, *et al.*, "Nanoparticle-Based Drug Delivery in Cancer Therapy and Its Role in Overcoming Drug Resistance," *Front. Mol. Biosci.*, vol. 7, art. no. 193, 2020, doi: 0.3389/fmolb.2020.00193.

29. D. Venturoli, and B. Rippe, "Ficoll and dextran vs. globular proteins as probes for testing glomerular permselectivity: Effects of molecular size, shape, charge, and deformability," *Am. J. Physiol. Renal Physiol.*, vol. 288, no. 4, pp. F605–F613, 2005, doi: 10.1152/ajprenal.00171.2004.

30. P. Decuzzi, *et al.*, "Intravascular Delivery of Particulate Systems: Does Geometry Really Matter?," *Pharm. Res.*, vol. 26, no. 1, pp. 235-243, 2009. doi: 10.1007/s11095-008-9697-x.

31. J. Dorantes García, "Cálculo de dimensión fractal y entropía en tumores benignos y malignos," B.S. thesis, FCFM-BUAP, Puebla, México, 2021.

32. Y. Gazit, J. W. Baish, *et al.*, "Fractal characteristics of tumor vascular architecture during tumor growth and regression," *Microcirculation*, vol. 4, no. 4, pp. 395-402, 1997, doi: 10.3109/10739689709146803.

33. M. C. Shelberg, N. Lam, and H. Moellering, "Measuring the fractal dimensions of surfaces," *Tech. Rep.*, DMACC, St. Louis AFS, MO, USA, Oct. 1983.

34. R. Perdomo-Pérez, *et. al.* (2022) "Thermodynamics, Static properties and transport behavior of fluids with competing interactions," *Journal of Physics: Condensed Matter*, vol. 34, no. 144005, 2022.

35. COMSOL AB, *COMSOL Multiphysics® Reference Manual*, ver. 5.5. Stockholm, Sweden: COMSOL AB, 2019.

36. Q. Luo, D. Kuang, B. Zhang, and G. Song, "Cell stiffness determined by atomic force microscopy and its correlation with cell motility," *Biochim. Biophys. Acta - Gen. Subj.*, vol. 1860, no. 9, pp. 1953–1960, 2016.

37. L. T. Baxter and R. K. Jain, "Transport of fluid and macromolecules in tumors. I. Role of interstitial pressure and convection," *Microvasc. Res.*, vol. 37, no. 1, pp. 77–104, 1989, doi: 10.1016/0026-2862(89)90074-5.

38. Y. Granot and B. Rubinsky, "Mass transfer model for drug delivery in tissue cells with reversible electroporation," *Int. J. Heat Mass Transf.*, vol. 51, no. 23–24, pp. 5610-5616, 2008, doi: 10.1016/j.ijheatmasstransfer.2008.04.041.

39. A. Kubik and L. Kleiser, "DNS of particle-laden flow over a backward facing step at a moderate Reynolds number," in *Particle-Laden Flow*, B. J. Geurts, H. Clercx, and W. Uijttewaal, Eds. Dordrecht, The Netherlands: Springer, 2007, pp. 269–286, doi: 10.1007/978-1-4020-6218-6_14.

40. A. S. Berrouk, D. Laurence, J. J. Riley, D. E. Stock, "Stochastic modelling of fluid velocity seen by heavy particles for two-phase LES of non-homogeneous and anisotropic turbulent flows," in *Particle-Laden Flow*, B. J. Geurts, H. Clercx, and W. Uijttewaal, Eds. Dordrecht, The Netherlands: Springer, 2007, pp. 179-192.